

Algorithmically Generated Rodent Hepatic Vascular Trees in Arbitrary Detail

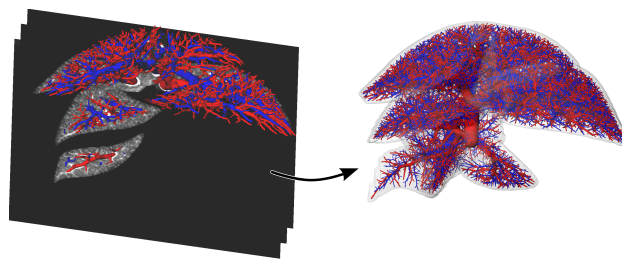
Lars Ole Schwen^{a,*}, Weiwei Wei^b, Felix Gremse^c, Josef Ehling^c, Lei Wang^a, Uta Dahmen^b, Tobias Preusser^{a,d}

^aFraunhofer MEVIS, Universitätsallee 29, 28359 Bremen, Germany

^bDepartment of General, Visceral and Vascular Surgery, University Hospital Jena, Drackendorfer Str. 1, 07747 Jena, Germany

^cExperimental Molecular Imaging, RWTH Aachen University, Pauwelsstrasse 30, 52074 Aachen, Germany

^dSchool of Engineering and Science, Jacobs University, Campus Ring 1, 28759 Bremen, Germany



Abstract

Physiologically realistic geometric models of the vasculature in the liver are indispensable for modelling hepatic blood flow, the main connection between the liver and the organism. Current in vivo imaging techniques do not provide sufficiently detailed vascular trees for many simulation applications, so it is necessary to use algorithmic refinement methods.

The method of Constrained Constructive Optimization (CCO) [1] is well suited for this purpose. Its results after calibration have been previously compared to experimentally acquired human vascular trees [2]. The goal of this article is to extend this calibration to the case of rodents (mice and rats), the most commonly used animal models in liver research. Based on in vivo and ex vivo micro-CT scans of rodent livers and their vasculature, we performed an analysis of various geometric features of the vascular trees. Starting from pruned versions of the original vascular trees, we applied the CCO procedure and compared these algorithmic results to the original vascular trees using a suitable similarity measure.

The calibration of the postprocessing improved the algorithmic results compared to those obtained using standard CCO. In terms of angular features, the average similarity increased from 0.27 to 0.61, improving the total similarity from 0.28 to 0.40. Finally, we applied the calibrated algorithm to refine measured vascular trees to the (higher) level of detail desired for specific applications. Having successfully adapted the CCO algorithm to the rodent model organism, the resulting individual-specific refined hepatic vascular trees can now be used for advanced modeling involving, e.g., detailed blood flow simulations.

Keywords: constrained constructive optimization, hepatic portal vein, hepatic vein

2010 MSC: 90C90, 92C35

*Corresponding author

Email addresses: ole.schwen@mevis.fraunhofer.de (Lars Ole Schwen), wei.weiwei@med.uni-jena.de (Weiwei Wei), fgremse@ukaachen.de (Felix Gremse), jehling@ukaachen.de (Josef Ehling), lei.wang@mevis.fraunhofer.de (Lei Wang), uta.dahmen@med.uni-jena.de (Uta Dahmen), tobias.preusser@mevis.fraunhofer.de (Tobias Preusser)

1. Introduction

The liver is a central organ for the mammalian metabolism as well as for clearance of xenobiotic substances from the blood plasma. The liver is connected to the organism via four vascular systems: blood is supplied by the portal vein (PV) and the hepatic artery (HA), the liver is drained by the hepatic vein (HV), and the bile ducts (BD). The PV, providing about 75 % of the hepatic blood flow, distributes venous blood rich in nutrients as it comes from the digestive system. The HA, providing the remaining hepatic blood supply and largely running in parallel with the PV, supplies the liver with arterial blood rich in oxygen. The HV drains the venous blood from the liver into the inferior vena cava. The BD drain the bile produced inside the liver [3]. The actual hepatic metabolism and elimination/clearance of compounds take place in the liver cells (hepatocytes), which are spatially organized in lobuli. Here a sinusoidal network permits an exchange of compounds between blood flowing through the network and hepatocytes adjacent to the sinusoids. The vascular trees of the liver thus provide the link between the organism and the functional units of the liver. Inter-individual variations of hepatic elimination are observed already for healthy livers, but in particular also in case of diseases [4].

1.1. Geometric Liver Models

Modeling and simulation of biophysical processes have become powerful tools for analyzing and understanding the behavior of dynamical biological systems as well as predicting their future states. Its impact lies, on the one hand, in basic science such as understanding how living organisms work, and on the other hand in applications such as improving surgical interventions and pharmaceutical developments.

In order to accurately simulate hepatic physiological processes, and thus avoid the need for performing actual experiments, single- or multi-scale models can be used. Pharmacokinetics models [5, 6] considering the liver as a well-stirred compartment can provide phenomenologically correct descriptions of total liver clearance or metabolism. Such models can, however, not take into account zonation [7] inside lobuli or heterogeneity on a larger length scale due to pathological conditions, such as steatosis [8, 9], fibrosis [10], cirrhosis [11], or hepatitis [12]). Two-scale models considering multiple sinusoids (see [13, 14] and the references therein for an overview) permit sinusoidal zonation and can, in principle, also incorporate different sinusoids for different regions of the liver. The same can be achieved using a two-scale model [15] using lobuli as the fine scale [16, 17] rather than sinusoids. In both cases, only using realistic vascular trees and organ geometry allows a mechanistic and individual-specific model. This is particularly important if a spatially heterogeneous pathological state is to be considered [18] or the influence of specific surgical techniques is to be assessed in rodents as model organisms. Examples of such surgical techniques include, but are not limited to, vessel-oriented liver resection [19] and their comparison to resections with mass ligation techniques [20].

Current contrast-enhanced radiological in vivo imaging provides sufficient resolution so that the main vascular trees can be reconstructed [21]. In vivo computed tomography (CT) provides sufficiently detailed vascular trees for planning liver resection surgery in humans [22, 23]. The level of detail may, however, be insufficient for modeling, depending on the spatial pattern of heterogeneity to be considered. In mouse livers, steady-state in vivo μ CT protocols in combination with large molecular weight (long circulating) blood pool contrast agents can be used. These allow non-invasive imaging of hepatic blood vessels at 35 μ m resolution [24]. Ex vivo imaging permits higher doses of radiation and thus better image quality. In either case, geometric parameters of the reconstructed vascular trees are subject to measurement and analysis errors [25] as well as limitations of the image size that can be processed.

In order to bridge the gap between the currently technically achievable vascular resolution and the one needed for accurate modeling (e.g., in [18]), algorithms for generating vascular trees can be applied, e.g., the method of constrained constructive optimization (CCO) [26]. In [2], a procedure was presented to evaluate and calibrate a CCO implementation to algorithmically generate geometrically realistic vascular trees for human livers. The goal of the present article is to transfer this algorithmic procedure to rodent hepatic vascular systems. For this purpose, we imaged vascular trees of rodents. We used twelve in vivo scans of mouse livers from a previous study focusing on tumor imaging [27], and nine corrosion casts of rat livers. These species are frequently used as animal models for liver investigations.

In this article, we describe two steps involving the algorithmic CCO procedure:

1. Calibration. First, we applied the algorithmic refinement procedure starting with substantially pruned versions of the experimentally acquired vascular trees. Comparing the results with experimentally acquired data, we could assess the quality of the algorithmic results and calibrate the algorithm to produce geometrically more realistic results.
2. Application. We then applied the algorithm to generate the desired level of detail in the vascular trees, this time starting from the full experimentally acquired vascular trees.

For the calibration step, we quantified similarity in terms of different geometric features using a statistics-based comparison described in [2]. We performed two types of analyses addressing the following questions.

1. How similar are experimentally acquired mouse PVs to each other?
⇒ What should the algorithm reproduce?
2. How similar are algorithmically generated mouse PVs to experimentally acquired PVs?
⇒ How well does the algorithm perform?

Besides the mouse PVs, we also considered the other types of vascular trees (mouse HVs, rat PVs, and rat HVs). Similarity is quantified on a scale from 0 to 1 (no significant differences) individually for different geometric features and averaged over these as described in [2]. In particular, we compare neither between PV and HV nor between species.

As for the application, we assume that the geometric properties determined in the experimentally acquired vascular trees also hold on finer geometric scales (self-similarity) so that our corresponding extrapolation is valid. Self-similarity is a plausible and partially verified assumption in this context, see, e.g., [28, 29, 30].

The HA is not considered in this study. Its radii are generally smaller than those of the PV, making it more difficult to experimentally acquire HA vascular trees in appropriate quality. For many modeling applications, however, the HA can be assumed to geometrically lie parallel to the PV [3]. The BDs are not considered here either since they are not part of the blood flow system on which we focus in this study.

1.2. Review of Related Work

1.2.1. Imaging of Vascular Structures

In vivo imaging of hepatic vascular trees can be performed using magnetic resonance imaging (MRI) or micro computed tomography (μ CT) [31]. While MRI does not expose the animal to X-rays, imaging whole organs at high resolution may require a scanning time up to hours [32]. In contrast, μ CT devices allow scanning the entire organ within minutes [24], but have the drawback of using ionizing radiation. Furthermore, the lower purchasing and maintenance costs have led to a higher availability. Since blood and other soft tissues have very similar radiodensity, a blood pool contrast agent is required to image the vasculature [33].

Many μ CT devices are designed for mice and have a limited bore diameter, making the excision of rat livers a necessity for scanning in these devices. Ex vivo μ CT imaging often results in a higher resolution compared to in vivo imaging, because much higher radiation doses and scanning durations can be used, because no motion artifacts occur, and because the scanning parameters can be optimized for the reduced sample sizes [24]. To prepare for ex vivo scanning, the vascular system is filled with a radiopaque polymerizing contrast agent [34], typically prior to explantation to preserve the shape of the organ. Two frequently used contrast agents are the polymerising monomer methylmethacrylate resin (Batson's No. 17 Plastic Replica and Corrosion Kit, Polysciences Inc., Warrington, PA, USA) and a silicone rubber polymer (Microfil, Flow Tech Inc., Carver, MA, USA) [34]. The former is mainly used to create corrosion casts, for which tissue is removed using a highly aggressive corrosive solution. Such casts are very fragile, but result in a higher contrast (polymer vs. air rather than tissue). Microfil specimens, however, have a soft, gel-like consistence, and are compatible with subsequent histological sectioning [35]. Optical imaging of histological serial sections may lead to much higher spatial resolution than ex vivo μ CT. For obtaining

3D datasets, however, registration of the 2D slices is required, causing tremendous experimental effort [36]. The resulting 3D data sets are typically four orders of magnitude larger than μ CT datasets, causing large computational effort for processing. Furthermore, remaining distortion artifacts can cause severe problems for subsequent image analysis. Hence we used μ CT imaging for the work presented here.

1.2.2. Image Processing

In order to obtain a geometric representation of the vascular trees, several image processing steps are necessary. For segmenting the liver and its vascular structures from the image data, numerous methods have been proposed in the literature, we refer to [37] for an overview. For our purposes, we chose an integrated, semi-automatic workflow including liver segmentation, vascular segmentation, and graph conversion [38], extended by an improved automatic vascular segmentation.

Various vascular models describing the appearance and geometric properties of vasculature have been proposed to fit in different image features [39]. Methods explicitly separating vascular models and image features normally require more computational effort, to optimize model parameters and calculate image features where models are fitted in [40, 41]. Therefore, vascular enhancement filters implicitly incorporating vascular shape models during feature calculation, such as Hessian-based enhancement filters, are favored [42, 43], in particular to enhance tube-like structures in 3D images. However, the Hessian-based filters with multi-scale parameters again decrease the calculation efficiency. Thus, we adopt a fast and efficient implementation of the Hessian-based filter and integrate it into a simple extraction scheme [44].

1.2.3. Morphometry

In order to quantify the similarity between different vascular trees, one should consider both geometric features and the topology, i.e., the connectivity structure, of the trees viewed as consisting nodes (bifurcation and end points) and edges.

The geometry of vascular edges can be described by lengths and radii (see, e.g., [45]), while bifurcations involve angles [46, 47, 48]. From these, a decrease of radii [46] and cross-section areas [49] at bifurcations, asymmetries [46, 50], and similar ratios for the lengths can be computed. Moreover, a bifurcation exponent γ satisfying the relation $r_p^\gamma = r_1^\gamma + r_2^\gamma$ can be computed, where r_p is the parent radius and $r_{\{1,2\}}$ are the daughter radii, see, e.g., [51]. This quantity has received some attention in the literature, including (but not limited to) $\gamma = 3$ being an optimal trade-off between the metabolic cost for maintaining the blood vessel wall and power dissipation for moving the blood if laminar Poiseuille flow can be assumed [52, 53]; $\gamma = 2.7$ being reported in [54]; and $\gamma = 2.55$ minimizing the reflection of pulse waves at bifurcations [55]. Based on additional assumptions, numerous derived have also been investigated, including pressures inside the vascular tree [56], supplied volumes and perfusion heterogeneity [57], and transit times [58], to name a few examples.

The simplest topological classification for edges in a tree is the generation number [59]. A frequently used classification is the Strahler order (e.g., in [60]) originally used to classify rivers [61], being a ‘major improvement [...] because it takes into account the asymmetric branching pattern’ [62]. Such a classification is necessary to restrict the geometric comparison to edges of similar importance in the vascular trees.

1.2.4. Algorithmic Refinement

One popular method to algorithmically generate vascular trees is based on constrained constructive optimization (CCO) [26], which is also the algorithmic concept we chose to use here. Alternatives to CCO include, but are not limited to, global constructive optimization [63, 64], deterministic geometric [65], and fractal [48, 66] construction procedures. Let us point out that the idea behind CCO is a phenomenological description of vascular trees of adults. It is not meant to (mechanistically) model angiogenesis, for which we refer the reader to [67, 68] and the review in [69]. Angiogenesis simulation can also be combined with subsequent geometric optimization of the vascular tree [70]. In contrast to most algorithms generating single vascular trees, methods to jointly generate supplying and draining vascular trees have been presented at a sub-organ length scale [71] and for tumors [72]. Grid-based methods, such as [65, 66, 72], have the drawback of producing a ‘somewhat stylized appearance’ [73, Fig. 1].

2. Material and Methods

We experimentally acquired 3D image data for hepatic vascular systems in rodents. For mice, 12 PVs and 12 HVs were obtained from 12 in vivo scans. For rats, 9 specimens were prepared, 3 showing both PV and HV, 3 showing only PV and 3 showing only HV, thus resulting in 6 PV and 6 HV datasets. The animal experiments were reviewed and approved by the local authorities according to German animal protection laws.

2.1. *In Vivo Imaging of Mouse Livers*

The scans used here were acquired in a previous study [27]. Twelve nude mice received an iodine-based blood-pool contrast agent (100 μ l, 130 mg of iodine per ml) [74], injected through the tail vein. Subsequently, we imaged them in a gantry-based dual energy flat-panel X-ray small animal μ CT device (TomoScope 30s Duo, CT-Imaging, Erlangen, Germany). The mice were inhalation-anesthetized with 1.5 % isoflurane in oxygen-enriched air via a face mask during in vivo measurements. The scanning duration for liver imaging was 6 minutes, resulting in 2880 projections with 1032×1012 pixels for each tube. We operated the two tubes of μ CT at 40 kV and 1.0 mA and at 65 kV and 0.5 mA [75], respectively. For reconstruction at isotropic voxel size 35 μ m, we used a Feldkamp-type reconstruction algorithm [76] including ring artifact correction (Impact-CB, CT-Imaging, Erlangen, Germany). The image data (16 bit integer) in our regions of interest had intensities in the ranges [0, 5649] to [0, 20370].

2.2. *Ex Vivo Imaging of Rat Liver Specimens*

For the hepatic vascular systems in rats, we prepared specimens which were subsequently scanned.

Prior to the surgical procedure to create the ex vivo rat liver specimens, we prepared Microfil polymer as a mixture of 2 ml MV-120 and 3 ml MV-Diluent solution (Flow Tech Inc., Carver, MA, USA). All surgical interventions were performed under inhalation anesthesia with 3 % isoflurane and an oxygen flow of 0.5 L/min (isoflurane vaporizer, Sigma Delta, UK) in an S1 operation room under sterile conditions. Animals were subjected to laparotomy via a transverse abdominal incision. We isolated the vessels (portal vein, hepatic artery, and inferior vena cava) under an operating microscope (Zeiss, Jena, Germany, magnification 10–25 \times), and heparinized the animals by i.v. injection of Heparin (Rotexmedica GmbH, Germany) 500 IU/kg BW 5 minutes before cannulation of the PV. Animals were sacrificed by opening the diaphragm and the intrathoracic vena cava. Then we ligated the infrahepatic abdominal cava and perfused the liver with 20 ml physiological saline solution at 66 ml/h using a perfusion pump (B. Braun Melsungen AG, Germany, with a 20 ml syringe). We performed a slow manually controlled injection of polymer with a maximal volume of up to 2 ml after adding 0.3 ml MV-curing agent (Flow Tech Inc., Carver, MA, USA) to the solution. In order to prevent any laceration of the liver surface, we explanted the whole liver with the catheter in place. Finally, we fixed the Microfil-injected liver sample in 4.5 % formalin solution. For one specimen, the superior caudate lobe (forming only a small fraction of the total volume) was resected for histological imaging outside this study.

For μ CT imaging, we mounted the ex vivo rat liver specimens near the central axis of a gantry-based dual energy flat-panel X-ray small animal μ CT device (TomoScope 30s Duo, CT-Imaging, Erlangen, Germany). We acquired 720 projections (1032×1012 pixels) during one full gantry rotation over 90 s, now operating both tubes at 65 kV and 0.5 mA. We reconstructed volumetric images as above with isotropic voxel size 35 μ m using the same Feldkamp-type algorithm including ring artifact correction as above (Impact-CB, CT-Imaging, Erlangen, Germany). The (16-bit integer) image data in the regions of interest had intensities in the ranges [0, 1814] to [0, 6512].

2.3. *Image Processing*

As the first step, we segmented the liver from the 3D image data using a semi-automatic procedure, using live-wire techniques and shape-based interpolation as described in [21]. This serves two purposes, it provides an organ mask for later use and evaluation, and it is used as the region of interest for the segmentation of vascular trees described next. A tree representation is obtained only at the end of this workflow, so the terms “structure” and “graph” (for pixel representations and after skeletonization, respectively) are used throughout this section.

2.3.1. Segmentation of Vascular Structures

We employed a semi-automatic segmentation framework requiring minimal user interactions for quick and robust segmentation of hepatic vein and portal vein [44]. First, in the preprocessing stage, we segmented the liver and analyzed the histogram of intensities to preclude regions with extremely low intensities. Then, a Hessian-based vesselness filter was adopted to enhance the vascular structures. For this purpose, we chose the multi-scale, Hessian-based vesselness filter introduced by Frangi et al. [77] to enhance vessels in the μ CT image data within the liver mask. Let σ denote the size of the Gaussian kernel used for calculating the Hessian matrices (second derivatives) $H(x, \sigma)$ of the image at every voxel position x and assume that the eigenvalues $\lambda_i = \lambda_i(x, \sigma)$, $i = 1, 2, 3$, of the $H(x, \sigma)$ are sorted according to $|\lambda_1| \leq |\lambda_2| \leq |\lambda_3|$. For simplicity of the notation, we consider all quantities to be dimensionless and omit the dependency on position, image intensity and filter width. Then Frangi's vesselness filter is defined as

$$f_\sigma(x) = \begin{cases} 0 & \text{if } \lambda_2 > 0 \text{ or } \lambda_3 > 0 \\ \left[1 - \exp\left(\frac{-R_A^2}{2\alpha^2}\right)\right] \cdot \exp\left(\frac{-R_B^2}{2\beta^2}\right) \cdot \left[1 - \exp\left(\frac{-S^2}{2c^2}\right)\right] & \text{otherwise} \end{cases} \quad (1)$$

where

$$R_A = \frac{|\lambda_2|}{|\lambda_3|}, \quad R_B = \frac{|\lambda_1|}{\sqrt{|\lambda_2\lambda_3|}}, \quad S = \sqrt{\lambda_1^2 + \lambda_2^2 + \lambda_3^2}. \quad (2)$$

Note that the terms R_A , R_B , and S in (2) depend on x and σ . The ratio R_A is designed to differentiate vessels from sheet-like structures, whereas R_B is used to distinguish vessels from blob-like structures. The term S suppresses noise structures. We set the parameters used in this filter to $\alpha = 0.5$, $\beta = 0.5$, and $c = 10$. The parameter c , unlike α and β , needs to be chosen to match the range of image intensities. Considering the radius range of the vascular structures, we heuristically chose three optimized scales for σ , 140 μm , 280 μm , and 560 μm which were able to capture vessels with thin, medium, and thick radii, respectively. The final vesselness response was obtained by extracting the maximum across all scales.

Based on the vesselness response, we initially segmented the vascular structures utilizing an automatic region-growing algorithm [78]. The seeds for the region-growing were automatically found by analyzing the histogram of vesselness outputs. We took all voxels with a vesselness value between the 90th and 99th percentiles as seed points. As the lower and upper thresholds for the region growing, we chose the 75th and 99.9th percentiles, respectively. If the vascular structures possessed high contrast against their surrounding structures, the initial segmentation typically yielded satisfactory results.

2.3.2. Bifurcative Tree Representation of Vascular Structures

In case the vascular structures exhibited low contrast, many irrelevant structures were enhanced as well by the vesselness filter and captured in the region-growing step. For refinement, we first transformed the segmented vessel structures into a graph representation [21]. This representation involves nodes and edges, the latter equipped with center lines (defined by skeleton points) and radii.

Unconnected components of the segmented vessels were transformed into separate graphs. These graphs were processed using two filters. We used a first filter to introduce a lower limit to the volume of each individual vascular graph. The graphs with volume less than 0.05 mm^3 were filtered out. Hence, unconnected components could be removed by this filter. Additionally, we determined the edge length of all branches in a graph tree and assigned a minimum threshold to filter out and truncate small branches shorter than 300 μm . These parameters were heuristically determined as being able to rule out isolated trees and prune spurious branches in the vascular trees.

We subsequently converted the vascular graphs to strictly bifurcative trees with cylindrical edges as described in [2]. In summary, an average radius was used and any intermediate skeleton points were discarded. Loops needed to be removed and mono-/multifurcations needed to be converted. Loops were characterized by more than one incoming edge at a node, in this case all except the one with largest radius were discarded. Nodes representing monofurcations were removed, setting the edge radius to the average of the two edges involved. Multifurcations were converted to multiple bifurcations with edges of length 0 and inheriting the parent radius.

2.4. Geometric Analysis

In order to quantify the similarity of different vascular trees we followed the approach we presented earlier in [2]. For the edges and bifurcations in the vascular trees, different geometric features were computed; as a topological hierarchy, Strahler-type orders [61] were assigned to the edges; histograms for the geometric features were computed on a per-order basis; and tools from statistics were used for a pair-wise comparison of the histograms between different vascular trees.

As geometric features, edge radii and lengths as absolute values, relative to the parent edge, and their asymmetry between sibling edges were considered. Moreover, the bifurcation exponent introduced above was computed. Each bifurcation was characterized by the three angles shown in Figure 1. Strahler orders [79] were computed for each edge, their differences to the maximum Strahler order in each tree were denoted by Strahler* order (as in [2] for a better comparison of trees with different resolution available) and used for the later analysis.

From these features, histograms (more precisely, the empirical cumulative distribution functions, CDFs) for each geometric feature, each Strahler* order, and each vascular tree were computed. These CDFs were then compared using a statistical two-sample Kolmogorov–Smirnov (KS) test [80], a non-parametric test for differences in the underlying distributions. Two CDFs were pragmatically classified as similar if the KS test did not show a significant ($p < \alpha = 0.05$) difference, even though this is, strictly speaking, a misuse of the statistical test. This standard, albeit arbitrary, choice of the significance level [81] is the same as in [2]. It was chosen to be neither too strict (larger α would lead to more frequent classification as different, thus a smaller similarity) nor to produce misleadingly high similarity values (for smaller α).

For one set of vascular trees (i.e., the intra-specimen comparison for mice or rats, PV or HV), the similarity was then defined to be the number of pair-wise comparisons classified as similar divided by the total number distinct of pairs. Note that these similarity values are still defined per geometric feature and per Strahler* order. So, in a first averaging step, a weighted average was computed over the Strahler* orders (weighted with the number of edges of the respective order) so that similarity values are obtained with respect to individual geometric features. In a second step, also averages over the geometric features were computed to obtain further simplified similarity measures. For the detailed formulas of these computations, we refer to [2]. In addition, we computed values ζ_{rad} , ζ_{len} , ζ_{ang} , and ζ_{total} of the radius, length, angular, and total similarity, respectively, as the arithmetic average over the four cases HV and PV for mice and rats.

For comparing algorithmically generated to experimentally acquired vascular trees, the same similarity measures and averaging steps are used, except that pairs to be compared are now from two disjoint sets of vascular trees. This is necessary to obtain meaningful values, but leads to a slightly different averaging, so that the similarity values for the cases of one or two sets of vascular trees should not be compared quantitatively [2]. In analogy to the values ζ above, we compute the arithmetic averages $\bar{\zeta}_{\text{rad}}$, $\bar{\zeta}_{\text{len}}$, $\bar{\zeta}_{\text{ang}}$, and $\bar{\zeta}_{\text{total}}$ when comparing two sets of vascular trees. These numbers allow providing a single scalar measure of the improvement by postprocessing.

2.5. Radius Accuracy Assessment

Besides the similarity analysis, we also assessed how well the radii of the experimentally acquired vascular trees match the CCO model assumptions of homogeneous perfusion and outflow resistance. The algorithm is described below in Section 2.6. For this purpose, we separately consider each of the

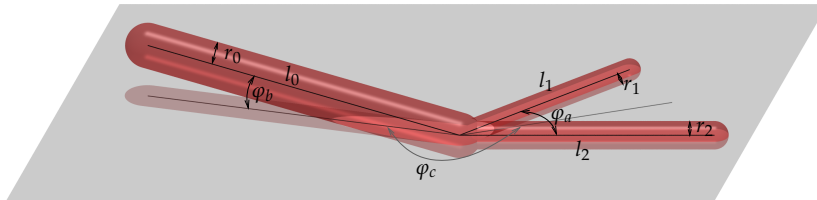


Figure 1: Geometric characterization of bifurcations. A vascular bifurcation is characterized by nine geometric parameters: three radii and three lengths, one each for the parent edge and the two daughter edges, and three angles. (Figure from [2])

experimentally acquired vascular trees T and determine a vascular tree T_m for a 1-to-1 comparison. The tree T_m has the same nodes and topology as T , its radii are modified to match the CCO model assumptions as follows.

- The outflow from each leaf node is proportional to the volume of its Voronoï cell (of the liver volume with respect to the leaf nodes), see also the analysis in [82].
- The outflow resistance is the same for each leaf node.
- The flow resistance R of each edge e (of length $l(e)$ and radius $r(e)$) is given by Poiseuille's law as [83]

$$R = \frac{8 \cdot l(e) \cdot \eta(r(e))}{\pi \cdot r(e)^4} \quad (3)$$

where the effective viscosity η depends on the radius (at least for small radii $< 150 \mu\text{m}$ due to the Fåhræus-Lindqvist effect [84] and according to the formula

$$\eta(r) = \frac{\eta_\infty}{(1 + \delta/r)^2} \quad (4)$$

with $\eta_\infty = 4 \cdot 10^{-3} \text{ Pa s}$, $\delta = 4.29 \mu\text{m}$ in the range $r \in [4, 150] \mu\text{m}$ [85]. We extended $\eta(r)$ constantly for $r < 4 \mu\text{m}$ and, in order to make η continuous at $150 \mu\text{m}$, used a linear transition from η according to Eq. 4 to η_∞ in the range $140 \mu\text{m} \leq r \leq 160 \mu\text{m}$.

For each edge e , let $r(e)$ be the radius of e in the vascular tree T and $r_m(e)$ the radius in T_m . In order to exclude edges at the resolution limit, we only considered the non-terminal edges of T to compute

$$\bar{d}(T) = \underset{\text{non-terminal edge } e \text{ of } T}{\text{mean}} (r(e) - r_m(e)) \quad (5a)$$

$$\hat{d}(T) = \underset{\text{non-terminal edge } e \text{ of } T}{\text{stdev}} (r(e) - r_m(e)) \quad (5b)$$

where $\bar{d}(T)$ can be interpreted as the systematic deviation between computed radii for the experimentally acquired data and those matching the model assumptions, whereas $\hat{d}(T)$ is a measure for how much the individual deviations are scattered. These values can either be viewed as absolute quantities (in μm) and compared to the voxel size, i.e., the inherent scale of imaging and image processing; or relative (in %) to the average radius considered for the average and standard deviation, more precisely the average radius of the non-terminal edges of the experimentally acquired vascular trees. Note that this relative deviation is not a relative error per edge. We were finally interested in the mean \bar{d} and standard deviation \hat{d} of $\bar{d}(T)$ and $\hat{d}(T)$, respectively, evaluated (a) over all rat Microfil specimens and (b) over all mouse in vivo scans, in both cases separately for PVs and HVs.

While the image processing did not work differently for PV and HV vascular trees, the experimental conditions both for creating Microfil specimens and for contrast-enhanced perfusion were slightly different due to the different physiology. In order to assess whether this has an influence on the accuracy of determining radii, we again considered the \bar{d} and \hat{d} values and used a statistical test to examine them for significant differences. As we had no reason to assume these values to follow a normal distribution (but also no reason to doubt it), we used a non-parametric statistical Cramér-von-Mises test [86] implemented in R [87] with $p < \alpha = 0.05$ as a standard significance level [81].

2.6. Constrained Constructive Optimization

As an algorithmic procedure for generating vascular trees of arbitrary level of detail, we used CCO [26] for the case of non-convex organs [1] subject to a calibration as described in [2]. In summary, CCO [26] is based on the physiologically plausible assumption of minimal intravascular volume to achieve a given perfusion. As no better data was available, we assumed homogeneous supply and drainage. The algorithm

first determines a set of pseudo-randomly [88] distributed leaf nodes. During the selection of leaf nodes, pair-wise minimal distance between leaf nodes is enforced in order to obtain a more or less homogeneous distribution. Moreover, a minimal distance to the organ boundary can be prescribed. Starting with an initial tree (e.g., the one obtained from the μ CT scan or a pruned version of it), these leaf nodes are connected one by one, each time introducing an optimal new bifurcation. Since there are edges of radius smaller than $150\text{ }\mu\text{m}$ to consider for rodent livers already at moderate resolution, the decreasing effective viscosity of the blood due to the Fåhræus-Lindqvist effect [85] needs to be taken into account.

Livers are clearly of non-convex shape. In the human case [2], this was taken into account via a penalty term [89] in the cost function of the optimization, penalizing bifurcation points lying outside the organ. This approach turned out to be insufficient for rodent livers and we added corresponding penalties for n equidistant points along each of the incident edges to the bifurcation. Heuristically, we determined $n = 16$ as a trade-off between accuracy and computational cost. The cost function is then the sum of all volumes of the cylinders representing the edges of the vascular tree plus the sum of the squared distances of those equidistant points weighted by 2.625 mm to mimic the cost function used in [2] and to match units.

During the optimization, radii at all bifurcations are balanced such that the flow resistance is equal for both subtrees and such that the bifurcation exponents satisfy $\gamma = 3$ as in [2]. Resistances are computed for the individual edges by Poiseuille’s law [83] and for the network by Kirchhoff’s law [90]. This results in equal exit pressures for all the leaf nodes. After adding the desired number of leaf nodes, all leaf nodes already present in the initial tree are removed and radii are again balanced as before. For a video illustrating this construction behavior, we refer to [91].

2.7. Calibration and Application

The two steps of our overall workflow as in [2], calibration and application, are illustrated in Figure 5 in the results section for two of the specimens. The experimentally acquired vascular tree datasets are pruned before CCO and subsequently a postprocessing step is applied to obtain different realizations of vascular trees (one of which is visualized) used for assessing the quality of the results and for calibrating the postprocessing. Finally, CCO including postprocessing is applied to the experimentally acquired trees to obtain pairs of vascular trees of higher detail.

In order to make use of as much input data as possible, we start with the full (not pruned) experimentally acquired vascular trees in the later application step. However, in the calibration step, we compare algorithmic results to the experimental data and thus need to apply a pruning step to obtain appropriate input. The pruning for each vascular tree is performed such that only the coarsest anatomic structure is preserved, since this is not meant to be generated by CCO. For this purpose, we proceed very similar to [2], starting from the root and recursively selecting daughter edges at bifurcations in the tree, as long as the radius is larger than 0.15 times the maximal edge radius or the bifurcation lies outside the liver mask. The latter condition accounts for the vascular trees originating from outside the organ.

Different random seeds for selecting the leaf nodes thus lead to different realizations of the CCO-generated trees. Moreover, using the same set of leaf nodes in a different order typically also changes the topology and geometry of the resulting tree. We algorithmically generated 20 different CCO trees for each of the experimentally acquired trees considered to have a sufficiently large basis of data for the analysis.

Since standard CCO did not give satisfactory results for the geometric angle features, we use the same postprocessing as described in [2]. The similarity in terms of φ_a is improved by shifting bifurcation points along the angle bisector by a distance to be calibrated below. Furthermore, the similarity in terms of φ_b is increased by moving out of the plane spanned by the three adjacent points by a pseudo-random [88] amount according to the distribution determined in the experimental vascular trees (combined for all Strahler* orders).

3. Results

3.1. Geometric Analysis

The results of the geometric similarity analysis for the four groups of experimentally determined vascular trees is shown in Figure 2. The absolute radius values show a low similarity, but we also expect

Table 1: Radius accuracy assessment. In order to assess how the radii determined in the experimentally acquired vascular trees match the model assumptions, edge radii of the experimentally acquired vascular trees were compared, on a one-to-one basis, to those of the topologically same trees with radii matching the model assumptions. The table lists means \pm standard deviation of the systematic deviation (\bar{d} , see Eq. 5a), and its scattering (\hat{d} , see Eq. 5b). For comparison, absolute values (in μm) are listed as well as values (in %) relative to the respective average radii from the experimentally acquired vascular trees.

specimen set		systematic deviation \bar{d}		scattering \hat{d}
mouse	PV	$-0.6 \pm 38.7 \mu\text{m}$	$(-1.5 \pm 23.3 \%)$	$72.2 \pm 17.2 \mu\text{m}$ ($41.5 \pm 7.2 \%$)
	HV	$31.7 \pm 56.4 \mu\text{m}$	$(13.2 \pm 22.7 \%)$	$145.9 \pm 39.6 \mu\text{m}$ ($54.2 \pm 10.3 \%$)
rat	PV	$74.2 \pm 60.1 \mu\text{m}$	$(31.8 \pm 24.9 \%)$	$64.7 \pm 13.2 \mu\text{m}$ ($29.1 \pm 6.6 \%$)
	HV	$-73.4 \pm 121.3 \mu\text{m}$	$(-21.9 \pm 33.8 \%)$	$250.4 \pm 75.8 \mu\text{m}$ ($62.7 \pm 16.6 \%$)

least robust results from the analysis. This feature is discussed in more detail in Section 3.2. The other (derived) radius-related features show a higher similarity, so that the average similarity for the radius features is moderate ($\zeta_{\text{rad}} = 0.496$). Similarity in terms of length and angle features is generally moderate to high ($\zeta_{\text{len}} = 0.763$ and $\zeta_{\text{ang}} = 0.734$). This results in $\zeta_{\text{total}} = 0.700$. The more detailed analysis per Strahler* order generally exhibits a decreasing similarity from the root to the periphery of the vascular trees, see the detailed similarity analysis in the supporting information S2.

3.2. Radius Accuracy Assessment

The systematic deviation between radii determined from the experimentally acquired datasets and those fitting the model assumptions (mean \bar{d} , see Eq. 5a) was in the range of one voxel ($-0.6 \mu\text{m}$ and $31.7 \mu\text{m}$ for mouse the PVs and HVs, respectively, with voxel size $35 \mu\text{m}$; $74.2 \mu\text{m}$ and $-73.4 \mu\text{m}$ for the rat PVs and HVs, respectively, with voxel size $70 \mu\text{m}$), see Table 1. This is below 30 % of the respective average radii; interestingly with opposite sign for PV and HV for the rat cases. The average scattering of the deviations (mean \hat{d} , see Eq. 5b) was in the range of up to four voxels or up to more than 60 % of the average radius. A detailed 1-to-1 comparison of radii used to compute \bar{d} and \hat{d} is shown in the supporting information S1.

Comparing the results for PV and HV vascular trees separately for the two species, we obtained no significant difference for the systematic deviation (\bar{d}) in mice ($p = 0.123$). Significant differences were observed for the scattering (\hat{d}) in mice ($p = 6.29 \cdot 10^{-5}$) as well as for both measures in rats (\bar{d} : $p = 0.028$, \hat{d} : $p = 0.002$).

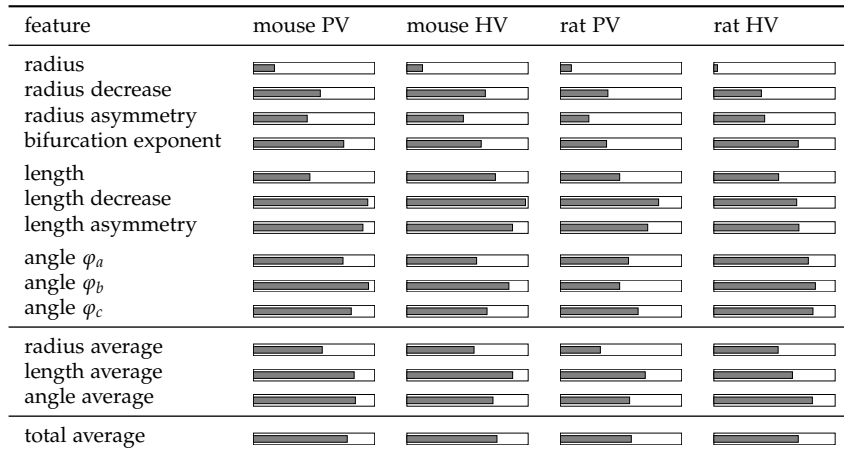


Figure 2: Inter-individual similarity. For mouse and rat, PV and HV vascular trees, the similarity of vascular trees within the respective groups in terms of different geometric features is shown in plots (longer gray bars stand for higher similarity).

3.3. Calibration of Constrained Constructive Optimization

The similarity values between vascular trees generated by the standard CCO procedure and the respective experimentally acquired vascular trees are plotted in Figure 3, separately for mouse and rat, PV and HV vascular trees. Note that the absolute similarity values cannot be compared directly to those shown in Figure 2, as discussed above.

Radius features were not similar in the measure considered here (average $\xi_{\text{rad}} = 0.048$ over the species and vascular system types), but lie in comparable ranges (see the supporting information S3). The bifurcation exponents are fixed to $\gamma = 3$ per algorithmic construction as opposed to the measurements. Radius asymmetry is much smaller in the algorithmically generated vascular trees. Length features show a moderate similarity ($\xi_{\text{len}} = 0.401$), the absolute lengths again lie in comparable ranges. Angle features also show a moderate similarity ($\xi_{\text{ang}} = 0.274$). This results in $\xi_{\text{total}} = 0.275$. For a detailed analysis, we refer to the supporting information S3. It includes plots of the respective cumulative distribution functions which were considered in the similarity analysis and in which the respective ranges of values can be seen.

As described above, a shift of bifurcation points along the angle bisector requires calibration of a “push-forward ratio” in order to increase the similarity in terms of φ_a . The shift, however, also affects length features and the other angle features. A value per group of vascular trees thus needs to be found so that the average overall similarity is maximized. This optimum can be determined from the plots in Figure 4. Combined with shifting bifurcations out of plane as described above, the postprocessing of the trees also has an effect on the objective function used in the CCO procedure, average relative changes \pm standard deviations are listed in Figure 3. The values slightly larger than 1 (the result of the CCO procedure) show that postprocessing only slightly reduces the optimality condition used for the CCO procedure. In fact, for some individual cases the postprocessing actually decreased the cost function used in the optimization. This is to be expected as CCO finds an optimal connection for the newly connected leaf node in each step, but is not a global optimization approach like [64].

The similarity values for different features are also plotted in Figure 3. For the angle features, the postprocessing lead to an increase in similarity to $\xi_{\text{ang}} = 0.609$, in particular for φ_b . The length features were affected by the postprocessing, with a slight increase in similarity in some cases and a slight decrease in the others, resulting in a slight decrease to $\xi_{\text{len}} = 0.387$. As the radii are not rebalanced during the postprocessing, the similarity in terms of radius features remained unaffected by the calibration, resulting in an increased $\xi_{\text{total}} = 0.400$.

3.4. Realistic Rodent Vascular Trees

We finally applied our calibrated procedure to algorithmically generate high-resolution vascular trees.

For the mouse liver with a computed volume of 1.142 ml (obtained from the organ segmentation in the μ CT data), we computed a number of 6281 lobuli. This was obtained by the same estimate as in [18]: We assume a lobular cross-section area of $A = 0.21 \text{ mm}^2$, a lobular radius of $r = 284.3 \mu\text{m}$ (assuming a regular hexagonal shape; both values from Table 1 in [92]), and the same elongation (height divided by diameter) of 1.52 as for human lobuli [3], Chapter 2.5. Based on this, a mouse lobulus has an estimated volume of $181.9 \cdot 10^{-9} \text{ l}$, approximately $1/6281$ of the total liver volume in this case. We thus chose the number of leaf nodes to be 6281 for both PV and HV.

The rat liver considered here had a computed volume of 12.34 ml (again obtained from the organ segmentation). Assuming the same lobule size as for mice, this corresponds to 67990 lobuli. As this number of leaf nodes was beyond the capabilities of our current implementation of the CCO procedure, we reduced it by a factor of 8 and chose a number of 8500 leaf nodes for PV and HV so that the domains drained by one terminal edge in the geometric model had twice the radius and length of a physiological lobule. Let us point out that the rat specimen chosen for these detailed results is the one with most detail (number of edges) in the PV vascular tree, despite the resection of the superior caudate lobe.

The resulting, algorithmically generated vascular trees for one mouse and one rat liver are visualized in Figure 5. The corresponding datasets plus some coarser intermediate trees are provided in the supporting information S4.

feature	mouse PV	mouse HV	rat PV	rat HV
radius				
radius decrease				
radius asymmetry				
bifurcation exponent				
length				
length decrease				
length asymmetry				
angle φ_a				
angle φ_b				
angle φ_c				
radius average				
length average				
angle average				
total average				
relative cost change	1.024 \pm 0.012	1.012 \pm 0.006	1.015 \pm 0.008	1.020 \pm 0.007

Figure 3: Similarity between experimentally acquired and algorithmically generated vascular trees. For mouse and rat, PV and HV vascular trees, the similarity of algorithmically generated and experimentally acquired vascular trees within the respective groups in terms of different geometric features is shown. In each plot, the upper, light gray, bar stands for the standard CCO results whereas the lower, dark gray, bar stands for the postprocessed results. This shows that the postprocessing improves the overall similarity between algorithmic results and measurements, but not for each individual geometric feature. The last row shows the change of the cost function (objective function used in the optimization procedure, essentially the intravascular volume) relative to the value before postprocessing. On average, the cost slightly increases by the postprocessing.

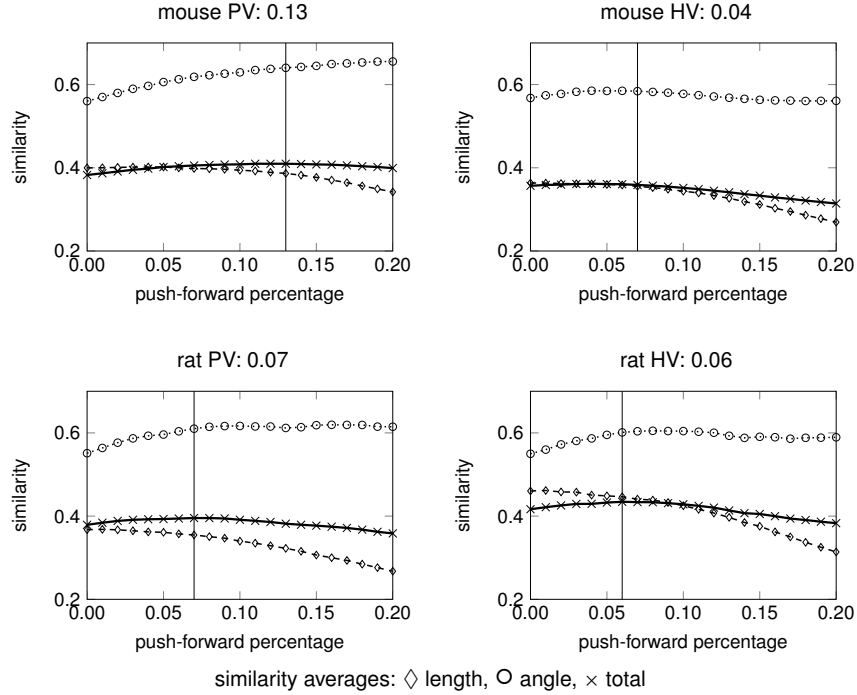


Figure 4: Calibration for shifting bifurcation points. As one part of the postprocessing step subsequent to the CCO procedure, bifurcation nodes are moved along the angle bisector of the daughter edges. These plots show the influence of different such “push-forward ratios” on the average length and angle as well as overall similarities between (fully postprocessed) algorithmically generated and experimentally acquired vascular trees. The optimum (maximal overall similarity) is a trade-off between improving similarity in the angle features while worsening the similarity in the length features. For the different groups of specimens, different optimal “push-forward ratios” are obtained.

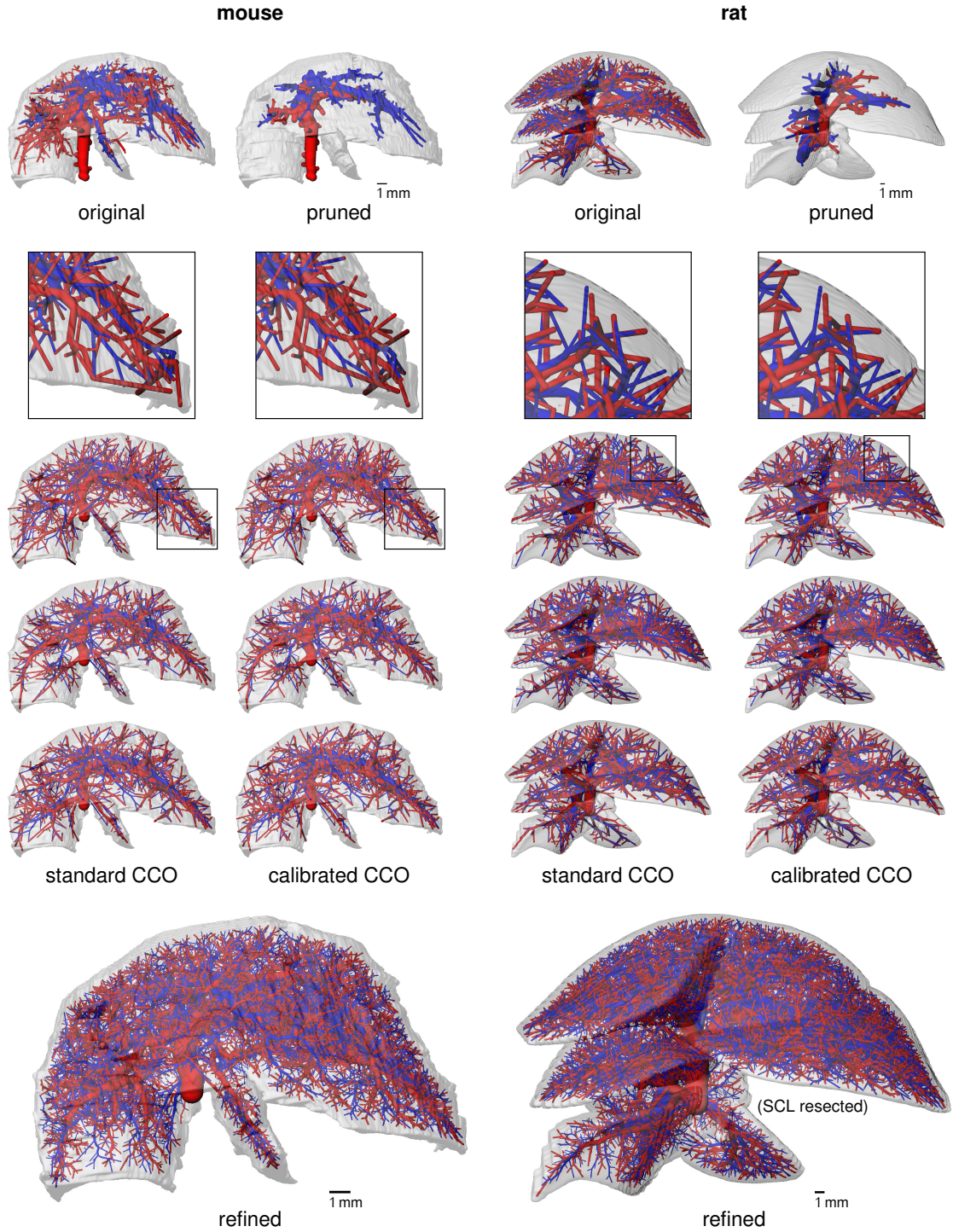


Figure 5: Calibration and application. Experimentally acquired vascular trees (“original”) for a mouse (left) and a rat (right) were pruned to have a starting point (“pruned”) for an assessment of the CCO procedure. Three out of 20 algorithmically generated CCO realizations are visualized, before and after postprocessing (“standard CCO” and “calibrated CCO”, respectively). The postprocessing only altered individual bifurcations, but not the overall appearance of the vascular trees. The boxes show zoomed views to illustrate the effect of the postprocessing. Finally, the CCO procedure including postprocessing was applied to the experimentally acquired vascular trees to obtain the desired level of detail, in our case 6281 and 8500 leaf nodes in the mouse and rat case, respectively (“refined”). Portal veins are shown in red, hepatic veins in blue, the organ shapes in gray.

4. Discussion

4.1. Geometric Analysis

Using experimentally acquired rodent vascular trees, we characterized the inter-individual similarity (Figure 2). For the different geometric features, a small to high similarity was observed. A more detailed analysis (see the supporting information S2) shows that the similarity generally decreased from the root towards the periphery (increasing Strahler* order). This is probably due to resolution limitations of the imaging and image processing.

In particular the radius features exhibited a low similarity among the experimentally acquired vascular trees. The main challenge is that the radii were in the range of few voxels in the image data, preventing robust measurements. Moreover, determined radii in the experimentally acquired vascular trees did not closely match our model assumptions (Table 1). This is additionally due to the fact that flow resistances play a rather central role in the geometric construction, but are highly sensitive to the radii due to the fourth power in Equation 3. Note, however, that the comparison in Table 1 is by no means a validation of the radius measurements as no ground truth was available.

The results in Table 1 do not give any indication whether the model assumptions about radii for homogeneous perfusion were inadequate, whether the image data did not accurately represent the real vascular radii, or to what extent the image processing incorrectly determined radii. Besides the limited resolution mentioned above, imaged radii are those of the radiopaque contrast agent flowing through the mouse livers or of the Microfil specimens after injection and polymerization in the rat livers. Both might slightly differ from the radii of the physiological vascular structures. The radius accuracy of the image processing could be addressed by a (software) phantom study as in [25] on the size scale of the μ CT scans and performing the image processing techniques used here.

The reason for the differences between PVs and HVs in the systematic deviation \bar{d} and the scattering \hat{d} (listed in Table 1) are unclear at present. The imaging and subsequent data processing procedures are, in principle, independent of the type of vascular system. Thus, the differences could indicate that the two types of vascular system differ in terms of their accessibility by the experimental procedures used here (perfusion by contrast agent, Microfil injection), or that our CCO assumptions require a slightly different adaption for PVs and HVs.

4.2. Calibrated Constructive Algorithm

Comparing the results of our algorithmic procedure to the experimentally acquired vascular trees showed a moderate similarity (Figure 3). The similarity was particularly low for the radius features, which is not surprising as this data is not robustly available for the experimentally acquired vascular trees. In particular, the bifurcation exponents were fixed to $\gamma = 3$ in the algorithm, and are not distributed as in the experimentally acquired vascular trees. Our calibration procedure could improve the results to some extent (Figure 4), in particular in terms of the angle features. For the geometric features with low similarity, we could at least verify that the values lie in comparable ranges, see the supporting information S3.

For the trees generated for calibration, let us point out that these do not necessarily match the coarse anatomic structures of the input data, see the differences between the three CCO realizations in Figure 5. Any anatomic details lost in the pruning process are not available to the algorithm, and the algorithm is not meant to recover such details. In the actual application, however, we start with the full experimentally acquired information and in particular do not lose the coarse anatomic information if it is available in the first place.

4.3. Comparison to the Human Case

Comparing the similarity values for rodents from this study to the previous results for human data reported in [2], we can observe that the similarity among experimentally acquired trees was slightly lower for rodents than in the human case (Figure 2 and the overview table in supporting information S2 vs. Table 3 in [2]). Comparing the algorithmic results to the experimentally acquired trees, the similarity in the rodent cases was notably lower than in the human case (Figure 3 and the overview table in

supporting information S3 vs. Table 6 in [2]). Both can be speculated to be due to less reliable data for the generally smaller specimens/organs and due to larger variations in the smaller number of rodent specimens. Furthermore, the postprocessing parameters determined in the calibration also varied for the different species as well as for PV and HV.

4.4. Limitations

As for the analysis performed here, twelve PVs and HVs for mice and six PVs and HVs for rats were used. This is a relatively small number of specimens, in particular compared to [2] where more than 160 datasets were available. This limitation is due to the large experimental and image processing effort, both of which are already at the limit of efficiency for batch processing. In particular, it would have been preferable for the calibration procedure to split the datasets in training data and data used for validation. Due to the small number of specimens, however, we decided to restrict our analysis to comparing each of the $20n$ algorithmically generated vascular trees to each of the n experimentally acquired trees.

The method itself is also subject to a few limitations, mainly already stated in [2]. In our similarity analysis, we only considered geometric features of the vascular trees. It would clearly be desirable to also consider functional properties such as spatially resolved perfusion or metabolic capacity. However, such data is not easily accessible by measurements, in particular in vivo. Computing them for the algorithmic results would moreover require additional well-established and validated assumptions. The geometric representation of vascular trees used in the analysis is a simplified approximation of the physiological setting. Neglecting curvature as well as variable and non-circular cross-section of vascular edges permits a consistent definition of geometric features at the cost of ignoring available geometric details. However, it is unclear at present to what extent this kind of geometric details is preserved correctly from the physiological setting through the experimental, imaging, and image processing procedure.

The assumption of homogeneous perfusion for CCO is plausible, but not experimentally funded. However, if data were available indicating perfusion heterogeneity at the length scale considered here, the algorithmic procedure could easily be adapted to take that heterogeneity into account. Moreover, we extrapolated geometric properties from the level of detail available from the experimentally acquired vascular trees to finer resolution. This is based on the plausible but not fully verified assumption of self-similarity.

4.5. Perspective

The algorithmic CCO procedure can be improved further. In our current implementation, the PV and HV in the same organ are generated independently, so they are not prevented from intersecting. Jointly generating the two vascular trees, maybe also adding the HA, should probably involve a joint flow/pressure model also including an effective representation of the organ tissue between the vascular trees, following the ideas in [93] possibly in a multi-scale fashion [94], and additionally add a non-intersection constraint in the construction process. It might be possible to combine this extension with a more global optimization approach [64] in the construction.

Another potential artifact is given by potential connections between territories that are actually supplied/drained separately in the physiological setting. To prevent this, the CCO procedure could be extended to take into account a subdivision of the liver into supplied and drained territories according to the experimentally acquired vascular trees available for our datasets [95], or into territories according to other schemes [96] for the human case. This would prevent artificial vascular connections across territory boundaries, which is not explicitly prevented in the current implementation. A second major advantage of treating territories separately is that this approach permits easy and efficient parallelization. Even without parallelization, the performance of the method can largely benefit from such a classical divide and conquer approach due to the $n^2 \log(n)$ computational complexity of the CCO implementation. Performance is a major bottleneck in the current implementation, the refined vascular trees in Figure 5 took several days to generate on a standard desktop PC. Let us point out, however, that this is not an issue for many simulation applications, as the geometric input is generated only once prior to multiple model simulations.

Depending on the application, e.g., for drug discovery and development [97], one might be more interested in geometrically “typical” (rather than individual-specific) liver models. To obtain those, shape

averaging techniques such as [98] could be applied and one would need to investigate whether an average of multiple liver shapes actually yields a typical shape.

5. Conclusions

The CCO procedure provides a framework for algorithmically refining hepatic vascular trees to an arbitrary level of detail. We here transferred the CCO procedure from human [2] to rodent livers and determined appropriate calibration parameters. The results are suitable geometric input for individual-specific models of processes involving hepatic perfusion. These models are needed in particular when taking into account organ-scale heterogeneity, e.g., in pharmacokinetics simulations or when assessing specific surgical techniques.

Acknowledgments

The authors would like to thank Olaf Dirsch for fruitful discussions about the preparation of the rat specimens, Constanze Sanger for the administration of these specimens, and Michael Schwier and Dipen Parekh for coordinating and performing the vascular segmentation. This work was funded by the systems biology network ‘Virtual Liver’ (<http://www.virtual-liver.de>) by the German Ministry of Education and Research (BMBF grant numbers 0315743 [FG], 0315765 [UD, WW], 0315769 [LOS, TP]). JE and FG were additionally funded by RWTH Aachen University (START-152/12).

References

- [1] W. Schreiner, R. Karch, M. Neumann, F. Neumann, P. Szawłowski, S. Roedler, Optimized arterial trees supplying hollow organs, *Medical Engineering & Physics* 28 (5) (2006) 416–429. doi:10.1016/j.medengphy.2005.07.019.
- [2] L. O. Schwen, T. Preusser, Analysis and algorithmic generation of hepatic vascular systems, *International Journal of Hepatology* (Article ID 357687) (2012) 1–17. doi:10.1155/2012/357687.
- [3] E. Kuntz, H.-D. Kuntz, *Hepatology: Textbook and atlas*, 3rd Edition, Springer, Heidelberg, 2008.
- [4] A. J. Atkinson Jr, W. Kushner, Clinical pharmacokinetics, *Annual Review of Pharmacology and Toxicology* 19 (1) (1979) 105–127. doi:10.1146/annurev.pa.19.040179.00054.
- [5] S. Willmann, J. Lippert, M. Sevestre, J. Solodenko, F. Fois, W. Schmitt, PK-Sim: a physiologically based pharmacokinetic ‘whole-body’ model, *BIOSILICO* 1 (4) (2003) 121–124. doi:10.1016/S1478-5382(03)02342-4.
- [6] T. Eissing, L. Kuepfer, C. Becker, M. Block, K. Coboecken, T. Gaub, L. Goerlitz, J. Jaeger, R. Loosen, B. Ludewig, M. Meyer, C. Niederalte, M. Sevestre, H.-U. Siegmund, J. Solodenko, K. Thelen, U. Telle, W. Weiss, T. Wendl, S. Willmann, J. Lippert, A computational systems biology software platform for multiscale modeling and simulation: Integrating whole-body physiology, disease biology, and molecular reaction networks, *Frontiers in Physiology* 2 (4) (2011) 1–10. doi:10.3389/fphys.2011.00004.
- [7] R. Gebhardt, Metabolic zonation of the liver: regulation and implications for liver function, *Pharmacology & Therapeutics* 53 (3) (1992) 275–354. doi:10.1016/0163-7258(92)90055-5.
- [8] M. Karcaaltincaba, O. Akhan, Imaging of hepatic steatosis and fatty sparing, *European Journal of Radiology* 13 (2007) 33–43. doi:10.1016/j.ejrad.2006.11.005.
- [9] J. Sun, Induction of fatty liver in low rats using different diets, Ph.D. thesis, University of Duisburg-Essen (2011).
- [10] N. S. Goldstein, F. Hastah, M. V. Galan, S. C. Gordon, Fibrosis heterogeneity in nonalcoholic steatohepatitis and hepatitis C virus needle core biopsy specimens, *American Journal of Clinical Pathology* 123 (2005) 382–387. doi:10.1309/EY72F1EN9XCB1KXX.
- [11] B. Holund, H. Poulsen, P. Schlichting, Reproducibility of liver biopsy diagnosis in relation to the size of the specimen, *Scandinavian Journal of Gastroenterology* 15 (3) (1980) 329–335. doi:10.3109/00365528009181479.
- [12] D. C. Rockey, S. H. Caldwell, Z. D. Goodman, R. C. Nelson, A. D. Smith, Liver biopsy, *Hepatology* 49 (3) (2009) 1017–1044. doi:10.1002/hep.22742.
- [13] M. S. Roberts, M. Rowland, A dispersion model of hepatic elimination: 1. Formulation of the model and bolus considerations, *Journal of Pharmacokinetics and Biopharmaceutics* 14 (3) (1986) 227–260. doi:10.1007/BF01106706.
- [14] K. S. Pang, M. Weiss, P. Macheras, Advanced pharmacokinetic models based on organ clearance, circulatory, and fractal concepts, *The AAPS Journal* 9 (2) (2007) E268–E283. doi:10.1208/aapsj0902030.
- [15] H.-G. Holzhutter, D. Drasdo, T. Preusser, J. Lippert, A. M. Henney, The virtual liver: A multidisciplinary, multi-level challenge for systems biology, *Wiley Interdisciplinary Reviews: Systems Biology and Medicine* 4 (3) (2012) 221–235. doi:10.1002/wsbm.1158.
- [16] R. Saxena, N. D. Theise, J. M. Crawford, Microanatomy of the human liver—exploring the hidden interfaces, *Hepatology* 30 (6) (1999) 1339–1346. doi:10.1002/hep.510300607.
- [17] S. Hoehme, M. Brulport, A. Bauer, E. Bedawy, W. Schormann, M. Hermes, V. Puppe, R. Gebhardt, S. Zellmer, M. Schwarz, E. Bockamp, T. Timmel, J. G. Hengstler, D. Drasdo, Prediction and validation of cell alignment along microvessels as order principle to restore tissue architecture in liver regeneration, *Proceedings of the National Academy of Sciences of the United States of America* 107 (23) (2010) 10371–10376. doi:10.1073/pnas.0909374107.

- [18] L. O. Schwen, M. Krauss, C. Niederaht, F. Gremse, F. Kiessling, A. Schenk, T. Preusser, L. Kuepfer, Spatio-temporal simulation of first pass drug perfusion in the liver, *PLOS Computational Biology* 10 (3) (2014) e1003499. doi:10.1371/journal.pcbi.1003499.
- [19] N. Madrahimov, O. Dirsch, C. Broelsch, U. Dahmen, Marginal hepatectomy in the rat: from anatomy to surgery, *Annals of Surgery* 244 (1) (2006) 89. doi:10.1097/01.sla.0000218093.12408.0f.
- [20] U. Dahmen, N. Madrahimov, F. Madrahimova, Y. Ji, A. Schenk, O. Dirsch, Small-for-size syndrome in the rat: Does size or technique matter?, *Journal of Surgical Research* 149 (1) (2008) 15–26. doi:10.1016/j.jss.2007.09.010.
- [21] D. Selle, B. Preim, A. Schenk, H.-O. Peitgen, Analysis of vasculature for liver surgical planning, *IEEE Transactions on Medical Imaging* 21 (11) (2002) 1344–1357. doi:10.1109/TMI.2002.801166.
- [22] I. Endo, H. Shimada, K. Takeda, Y. Fujii, K. Yoshida, D. Morioka, S. Sadatoshi, S. Togo, H. Bourquain, H.-O. Peitgen, Successful duct-to-duct biliary reconstruction after right hemihepatectomy. Operative planning using virtual 3D reconstructed images, *Journal of Gastrointestinal Surgery* 11 (5) (2007) 666–670. doi:10.1007/s11605-007-0130-2.
- [23] A. Schenk, S. Zidowitz, H. Bourquain, M. Hindennach, C. Hansen, H. K. Hahn, H.-O. Peitgen, Clinical relevance of model based computer-assisted diagnosis and therapy, in: M. L. Giger, N. Karssemeijer (Eds.), *Medical Imaging 2008: Computer-Aided Diagnosis*, Vol. 6915 of *Proceedings of SPIE*, International Society for Optics and Photonics, 2008, pp. 1–19. doi:10.1117/12.780270.
- [24] J. Ehling, M. Bartneck, X. Wei, F. Gremse, V. Fech, D. Möckel, C. Baek, K. Hittatiya, D. Eulberg, T. Luedde, F. Kiessling, C. Trautwein, T. Lammers, F. Tacke, CCL2-dependent infiltrating macrophages promote angiogenesis in progressive liver fibrosis, *Gut Online First* (2014). doi:10.1136/gut.jnl-2013-306294.
- [25] J. Drexler, V. Knappe, H. K. Hahn, K. S. Lehmann, B. Frericks, H. Shin, H.-O. Peitgen, Accuracy analysis of vessel segmentation for a LITT dosimetry planning system, in: T. M. Buzug, T. C. Lueth (Eds.), *Perspective in Image-Guided Surgery*, World Scientific, 2004, pp. 204–213, *proceedings of the Scientific Workshop on Medical Robotics, Navigation and Visualization*. doi:10.1142/9789812702678_0029.
- [26] W. Schreiner, Concepts and features of arterial tree models generated by constrained constructive optimization, *Comments on Theoretical Biology* 6 (1) (2001) 103–136.
- [27] J. Ehling, B. Theek, F. Gremse, S. Baetke, D. Möckel, J. Maynard, S.-A. Ricketts, H. Grüll, M. Neeman, R. Knuechel, W. Lederle, F. Kiessling, T. Lammers, Micro-CT imaging of tumor angiogenesis: Quantitative measures describing micromorphology and vascularization, *The American Journal of Pathology* 184 (2) (2014) 431–441. doi:10.1016/j.ajpath.2013.10.014.
- [28] J. H. G. M. Van Beek, S. A. Roger, J. B. Bassingthwaite, Regional myocardial flow heterogeneity explained with fractal networks, *American Journal of Physiology—Heart and Circulatory Physiology* 26 (1989) H1670–H1680.
- [29] M. Zamir, Fractal dimensions and multifractality in vascular branching, *Journal of Theoretical Biology* 212 (2) (2001) 183–190. doi:10.1006/jtbi.2001.2367.
- [30] D. Mancardi, G. Varetto, E. Bucci, F. Maniero, C. Guiot, Fractal parameters and vascular networks: facts & artifacts, *Theoretical Biology and Medical Modelling* 5 (2008) 12. doi:10.1186/1742-4682-5-12.
- [31] J. Ehling, T. Lammers, F. Kiessling, Non-invasive imaging for studying anti-angiogenic therapy effects, *Thrombosis and Haemostasis* 109 (3) (2013) 375–390. doi:10.1160/TH12-10-0721.
- [32] C. A. Berrios-Otero, Y. Z. Wadghiri, B. J. Nieman, A. L. Joyner, D. H. Turnbull, Three-dimensional micro-MRI analysis of cerebral artery development in mouse embryos, *Magnetic Resonance in Medicine* 62 (6) (2009) 1431–1439. doi:10.1002/mrm.22113.
- [33] F. Kiessling, S. Greschus, M. P. Lichy, M. Bock, C. Fink, S. Vosseler, J. Moll, M. M. Mueller, N. E. Fusenig, H. Traupe, W. Semmler, Volumetric computed tomography (VCT): a new technology for noninvasive, high-resolution monitoring of tumor angiogenesis, *Nature Medicine* 10 (2004) 1133–1138. doi:10.1038/nm1101.
- [34] F. Kiessling, D. Razansky, F. Alves, Anatomical and microstructural imaging of angiogenesis, *European Journal of Nuclear Medicine and Molecular Imaging* 37 (1) (2010) 4–19. doi:10.1007/s00259-010-1450-0.
- [35] L. Zagorchev, P. Oses, Z. W. Zhuang, K. Moodie, M. J. Mulligan-Kehoe, M. Simons, T. Couffinhal, Micro computed tomography for vascular exploration, *Journal of Angiogenesis Research* 2 (7) (2010) 1–11. doi:10.1186/2040-2384-2-7.
- [36] M. Schwier, T. Böhler, H. K. Hahn, U. Dahmen, O. Dirsch, Registration of histological whole slide images guided by vessel structures, *Journal of Pathology Informatics* 4 (2013) 10. doi:10.4103/2153-3539.109868.
- [37] A. Schenk, Liver segmentation and its application to hepatic interventions, Ph.D. thesis, Universität Bremen (2012). URL <http://nbn-resolving.de/urn:nbn:de:gbv:46-00102953-17>
- [38] H. Bourquain, A. Schenk, F. Link, B. Preim, G. Prause, H.-O. Peitgen, HepaVision2—a software assistant for preoperative planning in living-related liver transplantation and oncologic liver surgery, in: *CARS 2002 Computer Assisted Radiology and Surgery*, 2002, pp. 341–346. doi:10.1007/978-3-642-56168-9_56.
- [39] D. Lesage, E. D. Angelini, I. Bloch, G. Funka-Lea, A review of 3D vessel lumen segmentation techniques: Models, features and extraction schemes, *Medical Image Analysis* 13 (6) (2009) 819–845. doi:10.1016/j.media.2009.07.011.
- [40] O. Friman, M. Hindennach, C. Kühnel, H.-O. Peitgen, Multiple hypothesis template tracking of small 3D vessel structures, *Medical Image Analysis* 14 (2) (2010) 160–171. doi:10.1016/j.media.2009.12.003.
- [41] J. A. Tyrrell, E. di Tomaso, D. Fuja, R. Tong, K. Kozak, R. K. Jain, B. Roysam, Robust 3-D modeling of vasculature imagery using superellipsoids, *IEEE Transactions on Medical Imaging* 26 (2) (2007) 223–237. doi:10.1109/TMI.2006.889722.
- [42] M. Descoteaux, D. L. Collins, K. Siddiqi, A geometric flow for segmenting vasculature in proton-density weighted MRI, *Medical Image Analysis* 12 (4) (2008) 497–513. doi:10.1016/j.media.2008.02.003.
- [43] Y. Sato, S. Nakajima, N. Shiraga, H. Atsumi, S. Yoshida, T. Koller, G. Gerig, R. Kikinis, Three-dimensional multi-scale line filter for segmentation and visualization of curvilinear structures in medical images, *Medical Image Analysis* 2 (2) (1998) 143–68. doi:10.1016/S1361-8415(98)80009-1.
- [44] L. Wang, C. Hansen, S. Zidowitz, H. K. Hahn, Segmentation and separation of venous vasculatures in liver CT images, in: S. Aylward, L. M. Hadjiiski (Eds.), *Medical Imaging 2014: Computer-Aided Diagnosis*, Vol. 9035 of *SPIE Proceedings*, 2014. doi:10.1117/12.2043406.

- [45] J. N. Maina, P. van Gils, Morphometric characterization of the airway and vascular systems of the lung of the domestic pig, *sus scrofa*: comparison of the airway, arterial and venous systems, *Comparative Biochemistry and Physiology Part A* 130 (4) (2001) 781–798. doi:10.1016/S1095-6433(01)00411-1.
- [46] M. Gössl, M. Rosol, N. M. Malyar, L. A. Fitzpatrick, P. E. Beighley, M. Zamir, E. L. Ritman, Functional anatomy and hemodynamic characteristics of vasa vasorum in the walls of porcine coronary arteries, *The Anatomical Record* 272A (2) (2003) 526–537. doi:10.1002/ar.a.10060.
- [47] S.-Y. Wan, E. L. Ritman, W. E. Higgins, Multi-generational analysis and visualization of the vascular tree in 3D micro-CT images, *Computers in Biology and Medicine* 32 (2) (2002) 55–71. doi:10.1016/S0010-4825(01)00034-8.
- [48] J. C. Parker, C. B. Cave, J. L. Ardell, C. R. Hamm, S. G. Williams, Vascular tree structure affects lung blood flow heterogeneity simulated in three dimensions, *Journal of Applied Physiology* 83 (1997) 1370–1382.
- [49] M. Zamir, On fractal properties of arterial trees, *Journal of Theoretical Biology* 197 (4) (1999) 517–526. doi:10.1006/jtbi.1998.0892.
- [50] M. Zamir, Nonsymmetrical bifurcations in arterial branching, *Journal of General Physiology* 72 (6) (1978) 837–845. doi:10.1085/jgp.72.6.837.
- [51] C. A. Dawson, G. S. Krenz, K. L. Karau, S. T. Haworth, C. C. Hanger, J. H. Linehan, Structure-function relationships in the pulmonary arterial tree, *Journal of Applied Physiology* 86 (2) (1999) 569–583.
- [52] C. D. Murray, The physiological principle of minimum work. I. The vascular system and the cost of blood volume, *Proceedings of the National Academy of Sciences of the United States of America* 12 (3) (1926) 207–214. URL <http://www.jstor.org/stable/85001>
- [53] K. Horsfield, M. J. Woldenberg, Diameters and cross-sectional areas of branches in the human pulmonary arterial tree, *The Anatomical Record* 223 (3) (1989) 245–251. doi:10.1002/ar.1092230302.
- [54] N. Suwa, T. Niwa, H. Fukasawa, Y. Sasaki, Estimation of intravascular blood pressure gradient by mathematical analysis of arterial casts, *Tohoku Journal of Experimental Medicine* 79 (1963) 168–198. doi:10.1620/tjem.79.168.
- [55] T. Arts, R. T. Kruger, W. van Gerven, J. A. Lambregts, R. S. Reneman, Propagation velocity and reflection of pressure waves in the canine coronary artery, *American Journal of Physiology—Heart and Circulatory Physiology* 237 (4) (1979) H469–H474.
- [56] G. S. Krenz, J. H. Linehan, C. A. Dawson, A fractal continuum model of the pulmonary arterial tree, *Journal of Applied Physiology* 72 (6) (1992) 2225–2237.
- [57] M. Marxen, R. M. Henkelmann, Branching tree model with fractal vascular resistance explains fractal perfusion heterogeneity, *American Journal of Physiology—Heart and Circulatory Physiology* 284 (2003) H1848–H1857. doi:10.1152/ajpheart.00510.2002.
- [58] N. Mittal, Y. Zhou, C. Linares, S. Ung, B. Kaimovitz, S. Molloy, G. S. Kassab, Analysis of blood flow in the entire coronary arterial tree, *American Journal of Physiology—Heart and Circulatory Physiology* 289 (1) (2005) H439–H446. doi:10.1152/ajpheart.00730.2004.
- [59] K. Horsfield, G. Cumming, Morphology of the bronchial tree in man, *Journal of Applied Physiology* 24 (3) (1968) 373–383.
- [60] W. Huang, R. T. Yen, M. McLaurine, G. Bledsoe, Morphometry of the human pulmonary vasculature, *Journal of Applied Physiology* 81 (5) (1996) 2123–2133.
- [61] A. N. Strahler, Quantitative analysis of watershed geomorphology, *Transactions of the American Geophysical Union* 38 (6) (1957) 913–920. doi:10.1029/TR038i006p00913.
- [62] Z. L. Jiang, G. S. Kassab, Y. C. Fung, Diameter-defined Strahler system and connectivity matrix of the pulmonary arterial tree, *Journal of Applied Physiology* 76 (5) (1994) 882–892.
- [63] H. Hahn, M. Georg, H.-O. Peitgen, *Fractals in Biology and Medicine, Mathematics and Biosciences in Interaction*, Springer, 2005, Ch. Fractal Aspects of Three-Dimensional Vascular Constructive Optimization, pp. 55–66. doi:10.1007/3-7643-7412-8_5.
- [64] M. Georg, T. Preusser, H. K. Hahn, Global constructive optimization of vascular systems, Tech. Rep. 2010-11, Washington University in St. Louis, Department of Computer Science & Engineering (2010). URL http://cse.wustl.edu/Research/Lists/Technical%20Reports/Attachments/910/idealvessel_1.pdf
- [65] R. Gödde, H. Kurz, Structural and biophysical simulation of angiogenesis and vascular remodeling, *Developmental Dynamics* 220 (4) (2001) 387–401. doi:10.1002/dvdy.1118.
- [66] H. K. Hahn, C. J. G. Evertsz, H.-O. Peitgen, J. H. D. Fasel, Fractal properties, segment anatomy, and interdependence of the human portal vein and the hepatic vein in 3D, *Fractals* 11 (1) (2003) 53–62. doi:10.1142/S0218348X03001422.
- [67] F. Nekka, S. Kyriacos, C. Kerrigan, L. Cartilier, A model of growing vascular structures, *Bulletin of Mathematical Biology* 58 (3) (1996) 409–424. doi:10.1007/BF02460590.
- [68] D. Iber, D. Menshykau, The control of branching morphogenesis, *Open Biology* 3 (9) (2013) 130088. doi:10.1098/rsob.130088.
- [69] M. Scianna, C. Bell, L. Preziosi, A review of mathematical models for the formation of vascular networks, *Journal of Theoretical Biology* 333 (2013) 174–209. doi:10.1016/j.jtbi.2013.04.037.
- [70] M. Kretowski, Y. Rolland, J. Bézy-Wendling, J.-L. Coatrieux, Physiologically based modeling of 3-D vascular networks and ct scan angiography, *IEEE Transactions on Medical Imaging* 22 (2) (2003) 248–257. doi:10.1109/TMI.2002.808357.
- [71] A. A. Linninger, I. G. Gould, T. Marinnan, C.-Y. Hsu, M. Chojecki, A. Alaraj, Cerebral microcirculation and oxygen tension in the human secondary cortex, *Annals of Biomedical Engineering* 41 (11) (2013) 2264–2284. doi:10.1007/s10439-013-0828-0.
- [72] M. Welter, H. Rieger, Interstitial fluid flow and drug delivery in vascularized tumors: A computational model, *PloS one* 8 (8) (2013) e70395. doi:10.1371/journal.pone.0070395.
- [73] M. E. Gottlieb, Modelling blood vessels: A deterministic method with fractal structure based on physiological rules, in: *Proceedings of the Annual International Conference of the IEEE Engineering in Medicine and Biology Society*, Vol. 12, 1990, pp. 1386–1387. doi:10.1109/IEMBS.1990.691802.
- [74] A. de Vries, E. Custers, J. Lub, S. van den Bosch, K. Nicolay, H. Grull, Block-copolymer-stabilized iodinated emulsions for use as CT contrast agents, *Biomaterials* 31 (25) (2010) 6537–6544. doi:10.1016/j.biomaterials.2010.04.056.

- [75] F. Gremse, C. Grouls, M. Palmowski, T. Lammers, A. de Vries, H. Gröll, M. Das, G. Mühlenbruch, S. Akhtar, A. Schober, F. Kiessling, Virtual elastic sphere processing enables reproducible quantification of vessel stenosis at CT and MR angiography, *Radiology* 260 (3) (2011) 709–717. doi:10.1148/radiol.11110069.
- [76] L. A. Feldkamp, L. C. Davis, J. W. Kress, Practical cone-beam algorithm, *Journal of the Optical Society of America A* 1 (6) (1984) 612–619. doi:10.1364/JOSA.1.000612.
- [77] A. F. Frangi, W. J. Niessen, K. L. Vincken, M. A. Viergever, Multiscale vessel enhancement filtering, in: *Medical Image Computing and Computer-Assisted Intervention — MICCAI '98*, Vol. 1496 of *Lecture Notes in Computer Science*, 1998, pp. 130–137. doi:10.1007/BFb0056195.
- [78] R. Adams, L. Bischof, Seeded region growing, *IEEE Transactions on Pattern Analysis and Machine Intelligence* 16 (6) (1994) 641–647. doi:10.1109/34.295913.
- [79] S. B. Barker, G. Cumming, K. Horsfield, Quantitative morphometry of the branching structure of trees, *Journal of Theoretical Biology* 40 (1) (1973) 33–43. doi:10.1016/0022-5193(73)90163-X.
- [80] E. J. Dudewicz, S. N. Mishra, *Modern Mathematical Statistics*, Wiley series in probability and mathematical statistics, Wiley, 1988.
- [81] S. Stigler, Fisher and the 5% level, *Chance* 21 (4) (2008) 12. doi:10.1007/s00144-008-0033-3.
- [82] R. Karch, F. Neumann, M. Neumann, P. Szawlowski, W. Schreiner, Voronoi polyhedra analysis of optimized arterial tree models, *Annals of Biomedical Engineering* 31 (5) (2003) 548–563. doi:10.1114/1.1566444.
- [83] S. C. Gupta, *Fluid Mechanics and Hydraulic Machines*, Pearson Education India, 2006.
- [84] R. Fåhræus, T. Lindqvist, The viscosity of the blood in narrow capillary tubes, *American Journal of Physiology* 96 (3) (1931) 562–568.
- [85] A. Kamiya, T. Takahashi, Quantitative assessments of morphological and functional properties of biological trees based on their fractal nature, *Journal of Applied Physiology* 102 (2007) 2315–2323. doi:10.1152/japplphysiol.00856.2006.
- [86] M. Schumacher, Two-sample tests of Cramér–von Mises- and Kolmogorov–Smirnov-type for randomly censored data, *International Statistical Review / Revue Internationale de Statistique* 52 (3) (1984) 263–281.
URL <http://www.jstor.org/stable/1403046>
- [87] R Development Core Team, R: A Language and Environment for Statistical Computing, R Foundation for Statistical Computing, Vienna, Austria (2011).
URL <http://www.R-project.org/>
- [88] M. Matsumoto, T. Nishimura, Mersenne twister: A 623-dimensionally equidistributed uniform pseudo-random number generator, *ACM Transactions on Modeling and Computer Simulation* 8 (1) (1998) 3–30. doi:10.1145/272991.272995.
- [89] D. P. Bertsekas, *Nonlinear Programming*, 2nd Edition, Athena Scientific, Belmont, MA, 1999.
- [90] E. Marušić-Paloka, Rigorous justification of the Kirchhoff law for junction of thin pipes filled with viscous fluid, *Asymptotic Analysis* 33 (1) (2003) 51–66.
- [91] L. O. Schwen, M. Krauss, C. Niederal, F. Gremse, F. Kiessling, A. Schenk, T. Preusser, L. Kuepfer, Spatio-temporal simulation of first pass drug perfusion in the liver, *PLOS Computational Biology* 10 (3) (2014) e1003499, supporting Information Video S3. doi:10.1371/journal.pcbi.1003499.s003.
- [92] S. Hoehme, M. Brulport, A. Bauer, E. Bedawy, W. Schormann, M. Hermes, V. Puppe, R. Gebhardt, S. Zellmer, M. Schwarz, E. Bockamp, T. Timmel, J. G. Hengstler, D. Drasdo, Prediction and validation of cell alignment along microvessels as order principle to restore tissue architecture in liver regeneration, supporting Information (2010). doi:10.1073/pnas.0909374107.
- [93] T. Ricken, U. Dahmen, O. Dirsch, A biphasic model for sinusoidal liver perfusion remodeling after outflow obstruction, *Biomechanics and Modeling in Mechanobiology* 9 (4) (2010) 435–450. doi:10.1007/s10237-009-0186-x.
- [94] P. T. Boggs, D. M. Gay, S. K. Griffiths, R. M. Lewis, K. R. Long, S. Nash, R. H. Nilson, Optimization algorithms for hierarchical problems with application to nanoporous materials, *SIAM Journal on Optimization* 22 (4) (2012) 1285–1308. doi:10.1137/110856411.
- [95] D. Selle, W. Spindler, B. Preim, H.-O. Peitgen, *Mathematics unlimited – 2001 and beyond*, Springer, 2001, Ch. Mathematical methods in medical imaging: analysis of vascular structures for liver surgery planning, pp. 1039–1059.
- [96] J. H. D. Fasel, A. Schenk, Concepts for liver segment classification: Neither old ones nor new ones, but a comprehensive one, *Journal of Clinical Imaging Science* 3 (4) (2013) 48. doi:10.4103/2156-7514.120803.
- [97] H. M. Jones, I. B. Gardner, K. J. Watson, Modelling and PBPK simulation in drug discovery, *AAPS Journal* 11 (1) (2009) 155–166. doi:10.1208/s12248-009-9088-1.
- [98] M. Rumpf, B. Wirth, A nonlinear elastic shape averaging approach, *SIAM Journal on Imaging Sciences* 2 (3) (2009) 800–833. doi:10.1137/080738337.

6. Supporting Information

In the supporting information, we provide more detailed analysis results and vascular datasets for the two cases shown in Figure 5.

S1 [pdf]. Detailed results of the 1-to-1 comparison of measured radii and those matching the model assumptions for each specimen

S2 [pdf]. Detailed results of the inter-individual similarity analysis among mouse PV, mouse HV, rat PV, rat HV

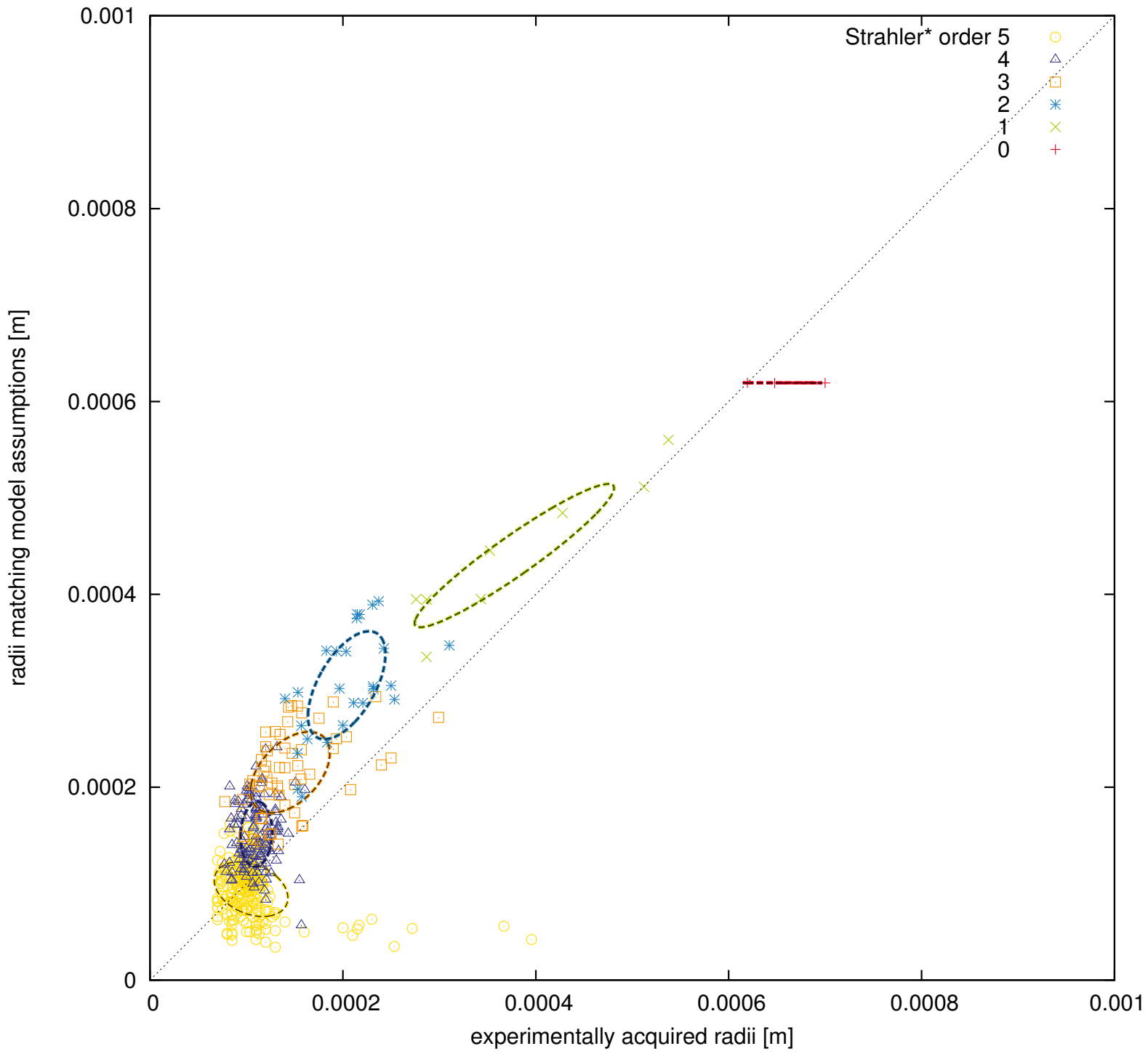
S3 [pdf]. Detailed results of the similarity analysis between experimentally acquired and algorithmically generated vascular trees, same four cases, before and after calibration

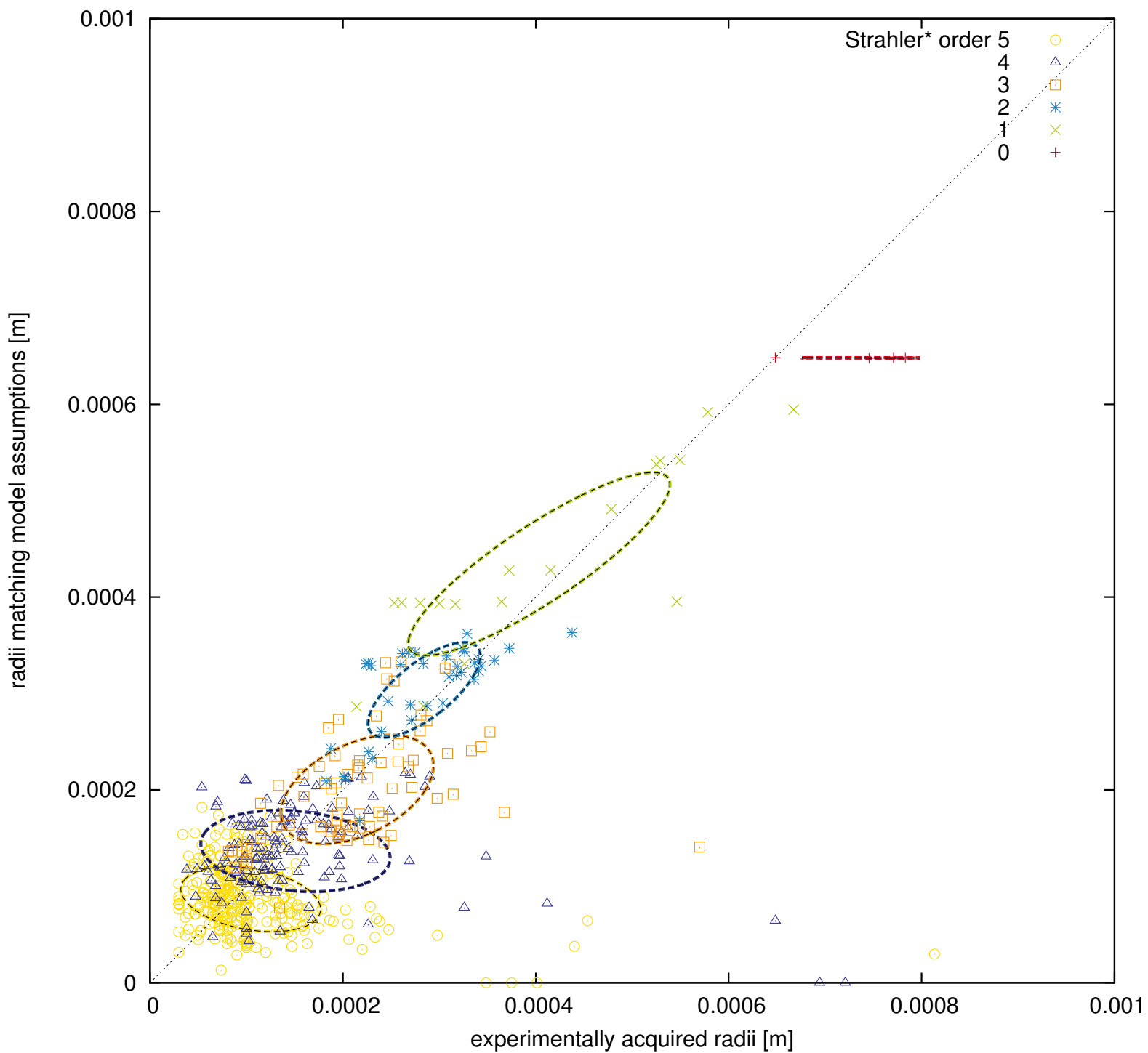
S4 [archive]. Datasets shown in Figure 5 plus intermediate generated trees (including a simple viewer tool from [18])

Radius Accuracy Assessment

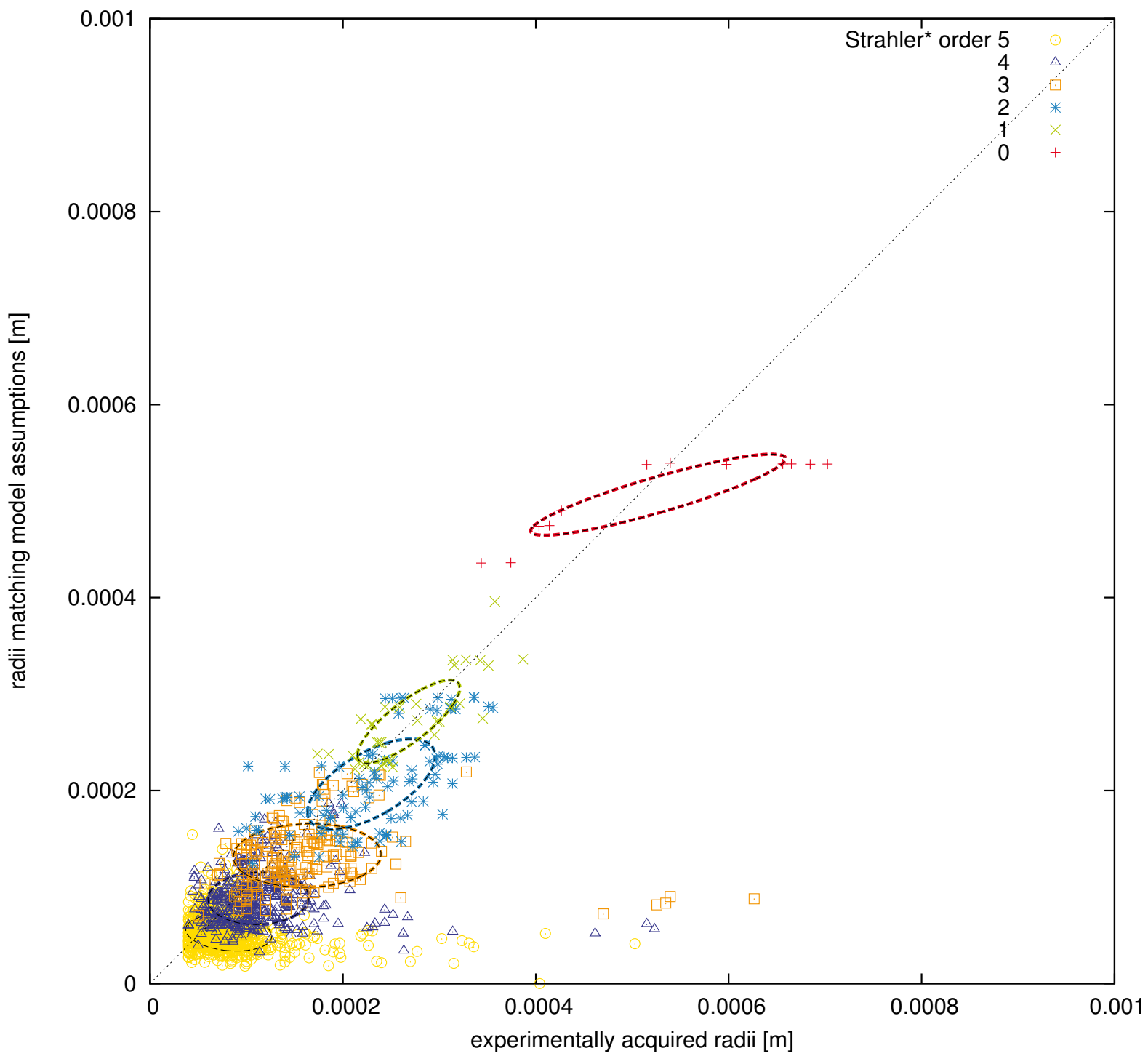
Lars Ole Schwen	Weiwei Wei	Felix Gremse	Josef Ehling
Lei Wang	Uta Dahmen	Tobias Preusser	

Mouse PV 1/12

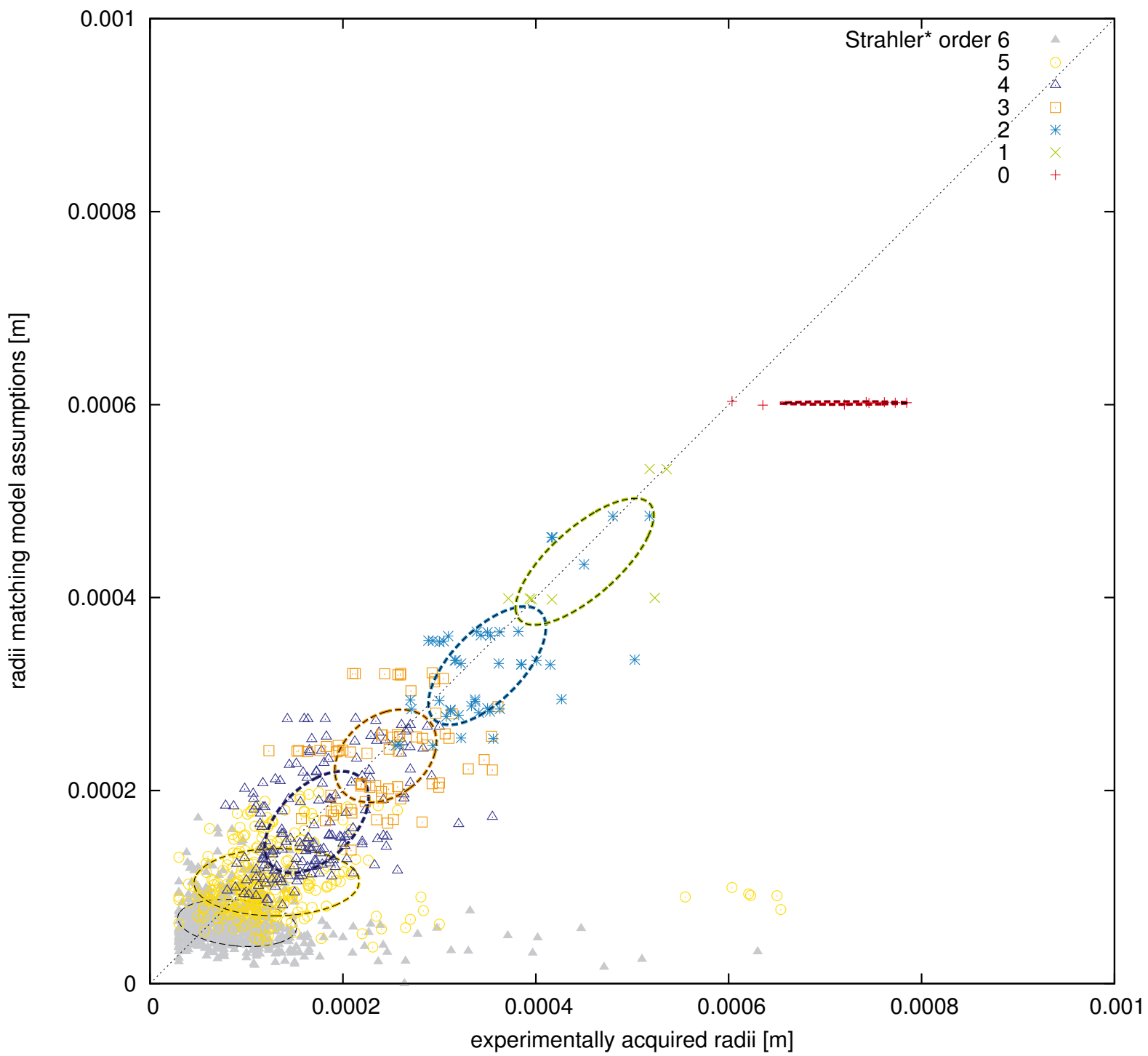




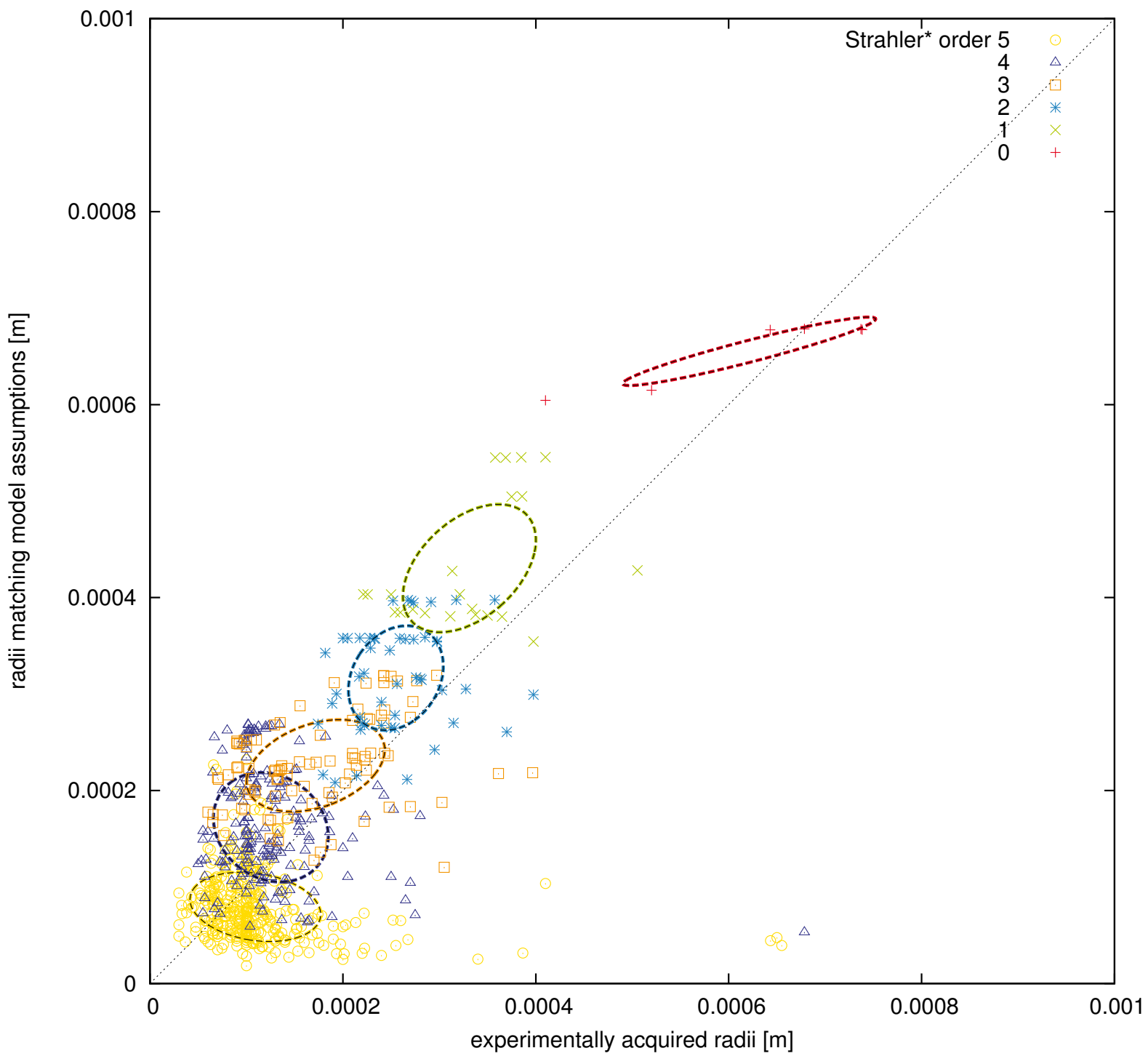
Mouse PV 3/12



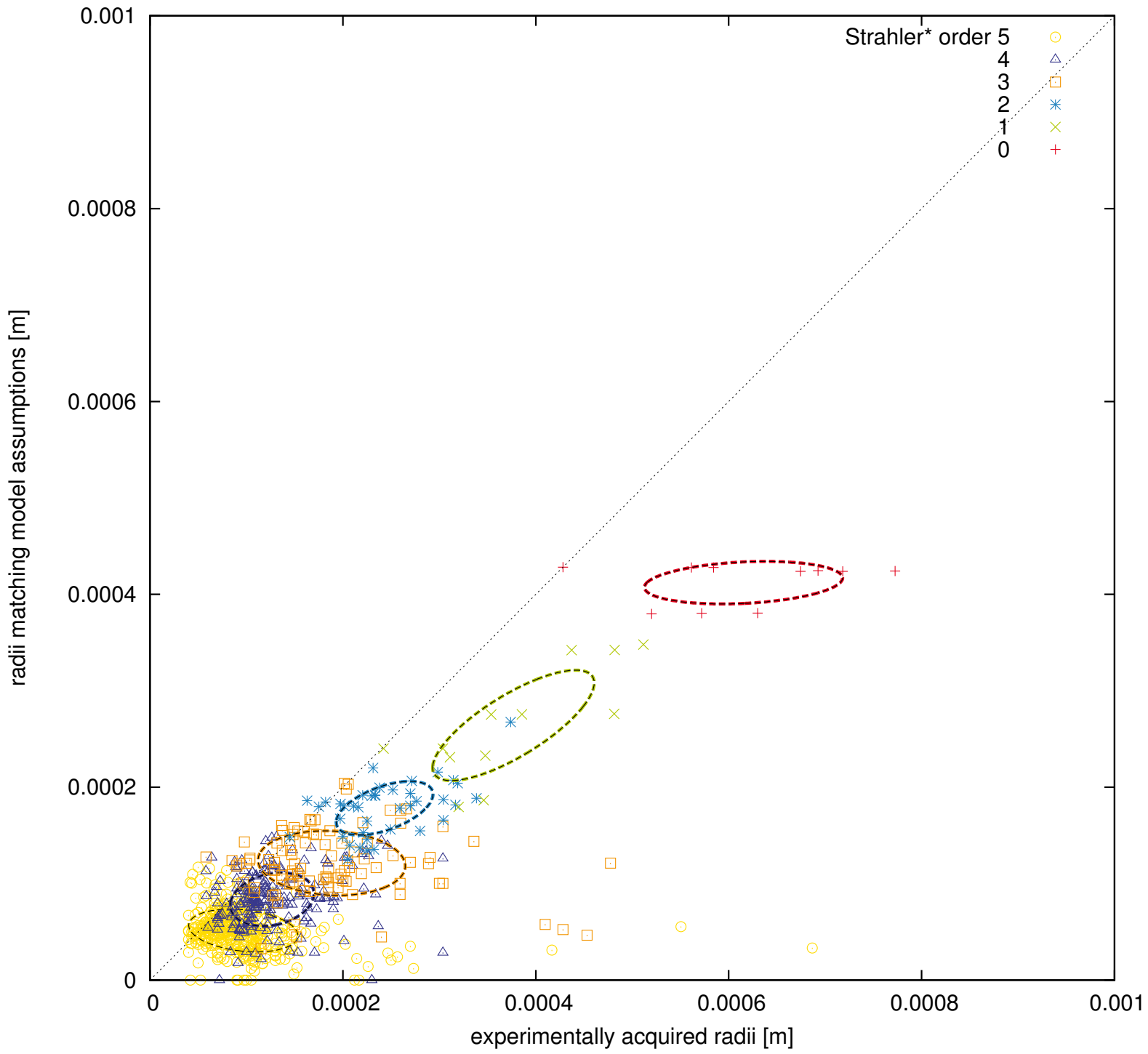
Mouse PV 4/12



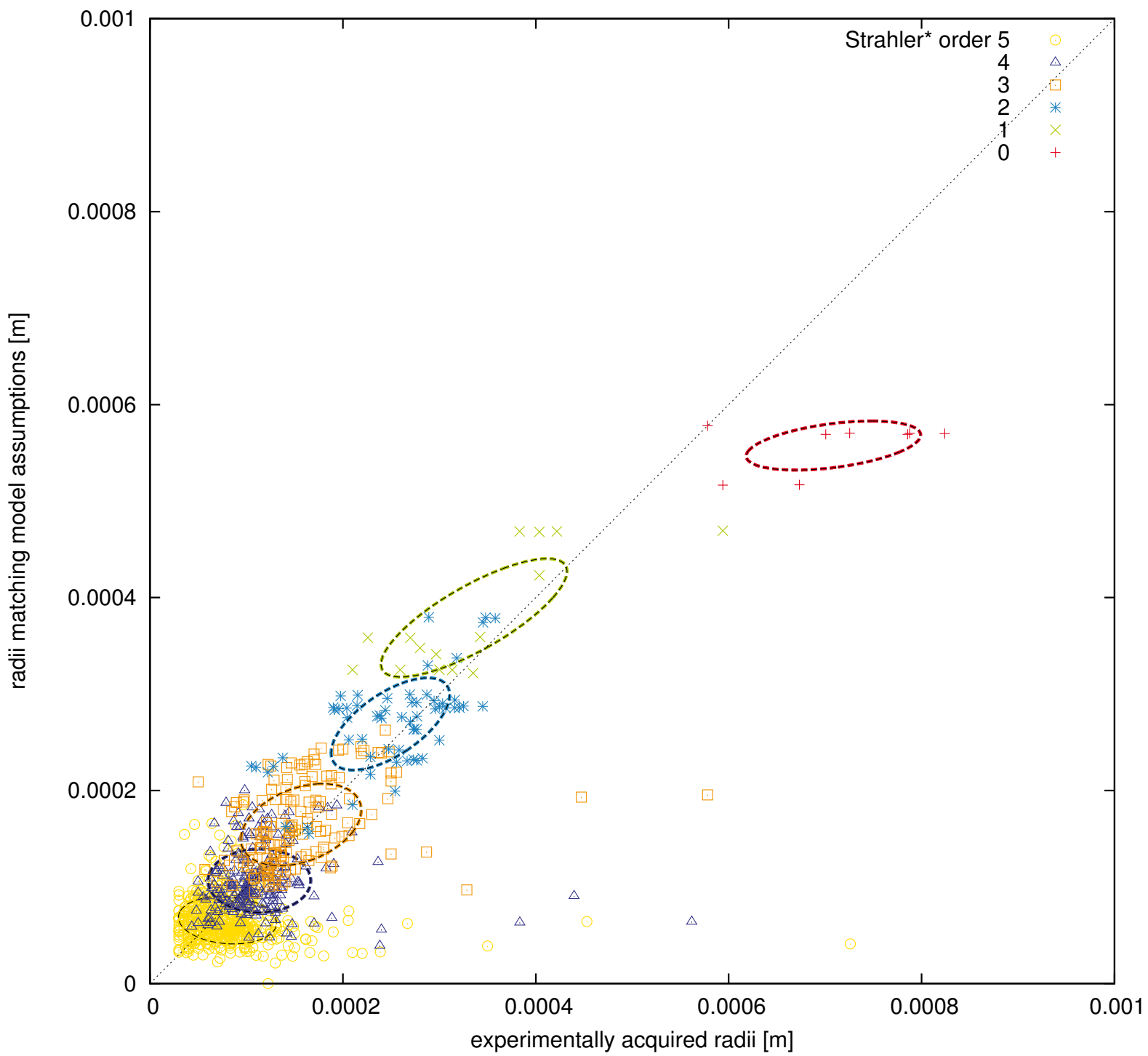
Mouse PV 5/12



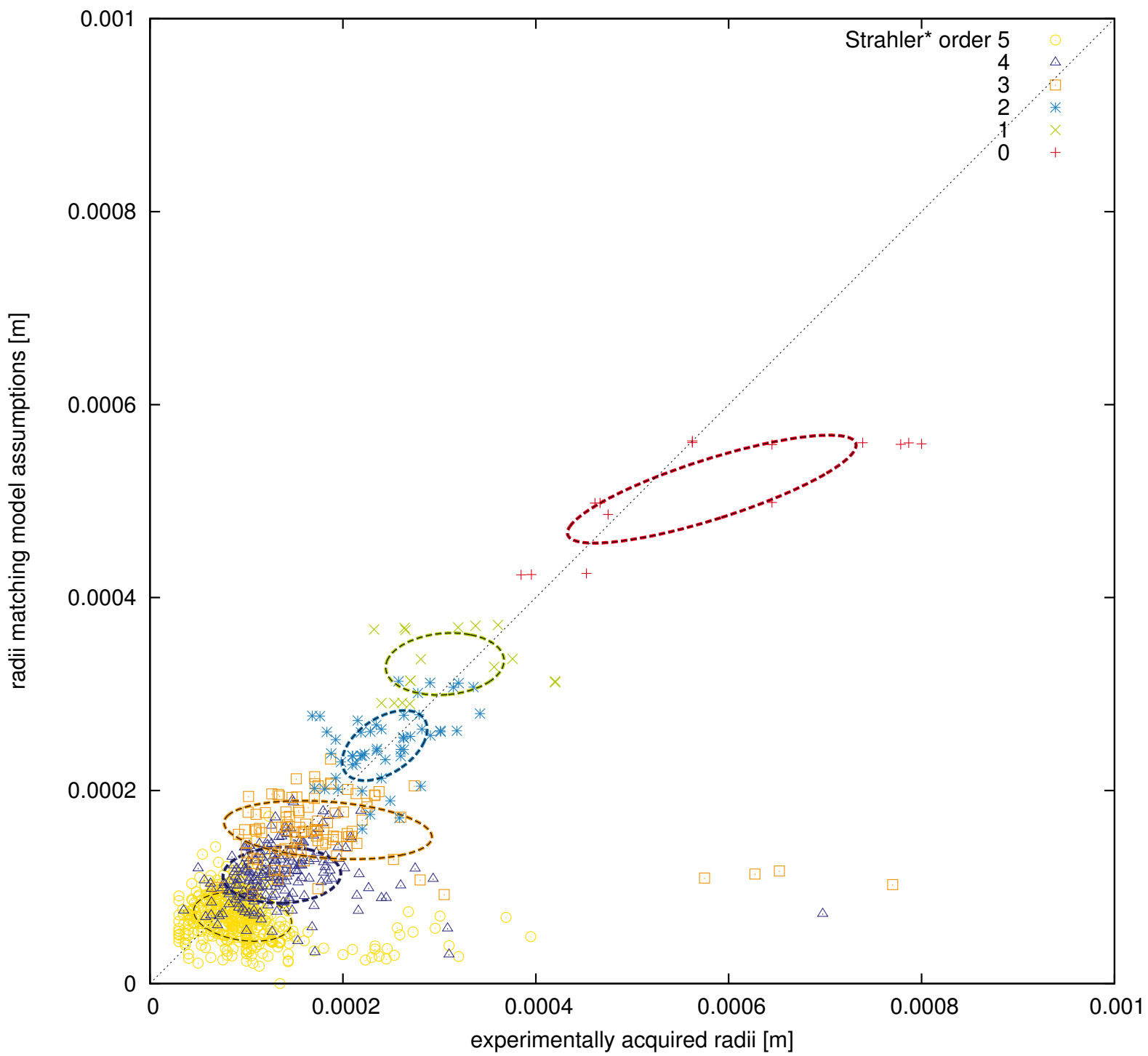
Mouse PV 6/12



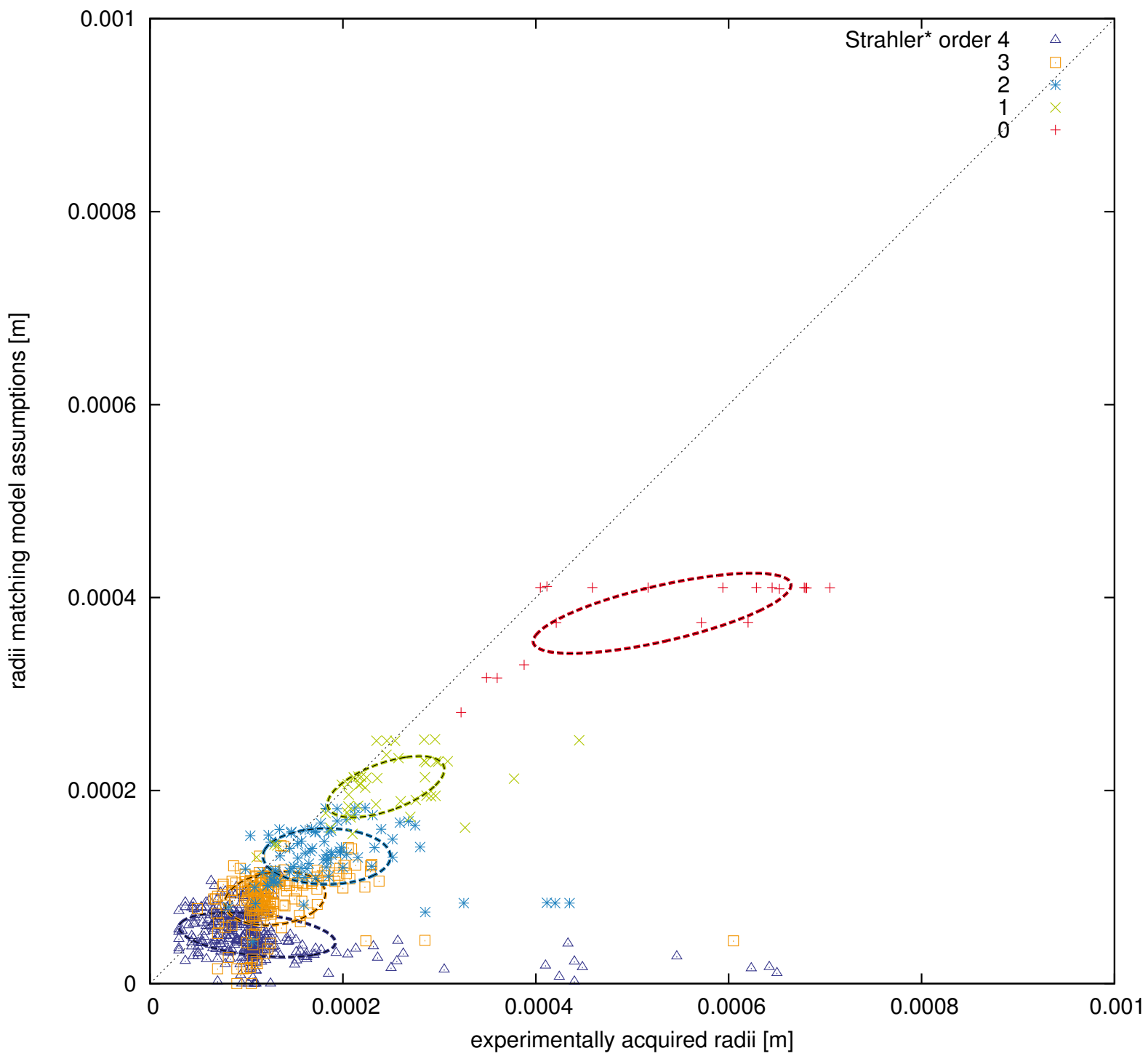
Mouse PV 7/12



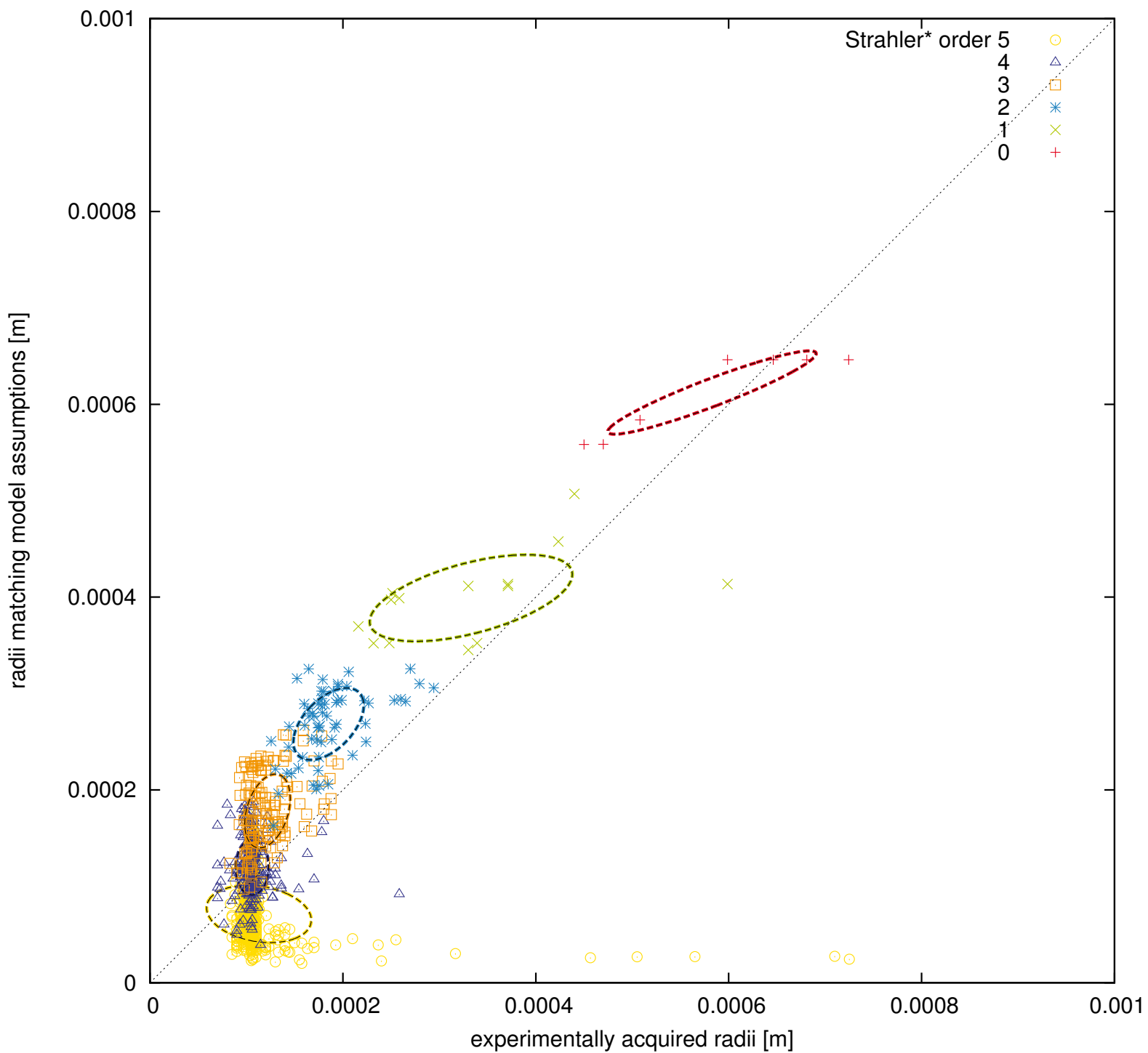
Mouse PV 8/12



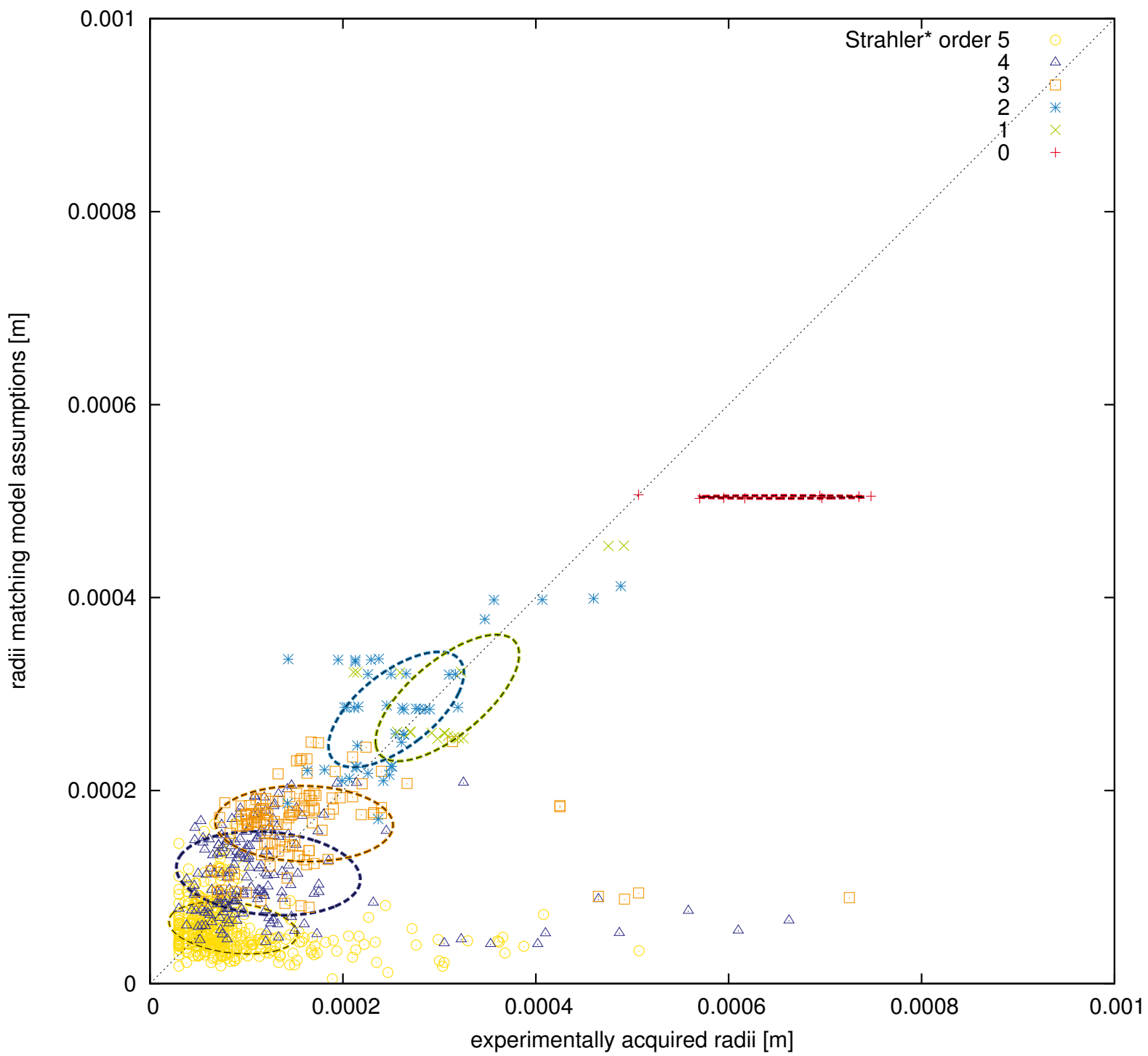
Mouse PV 9/12



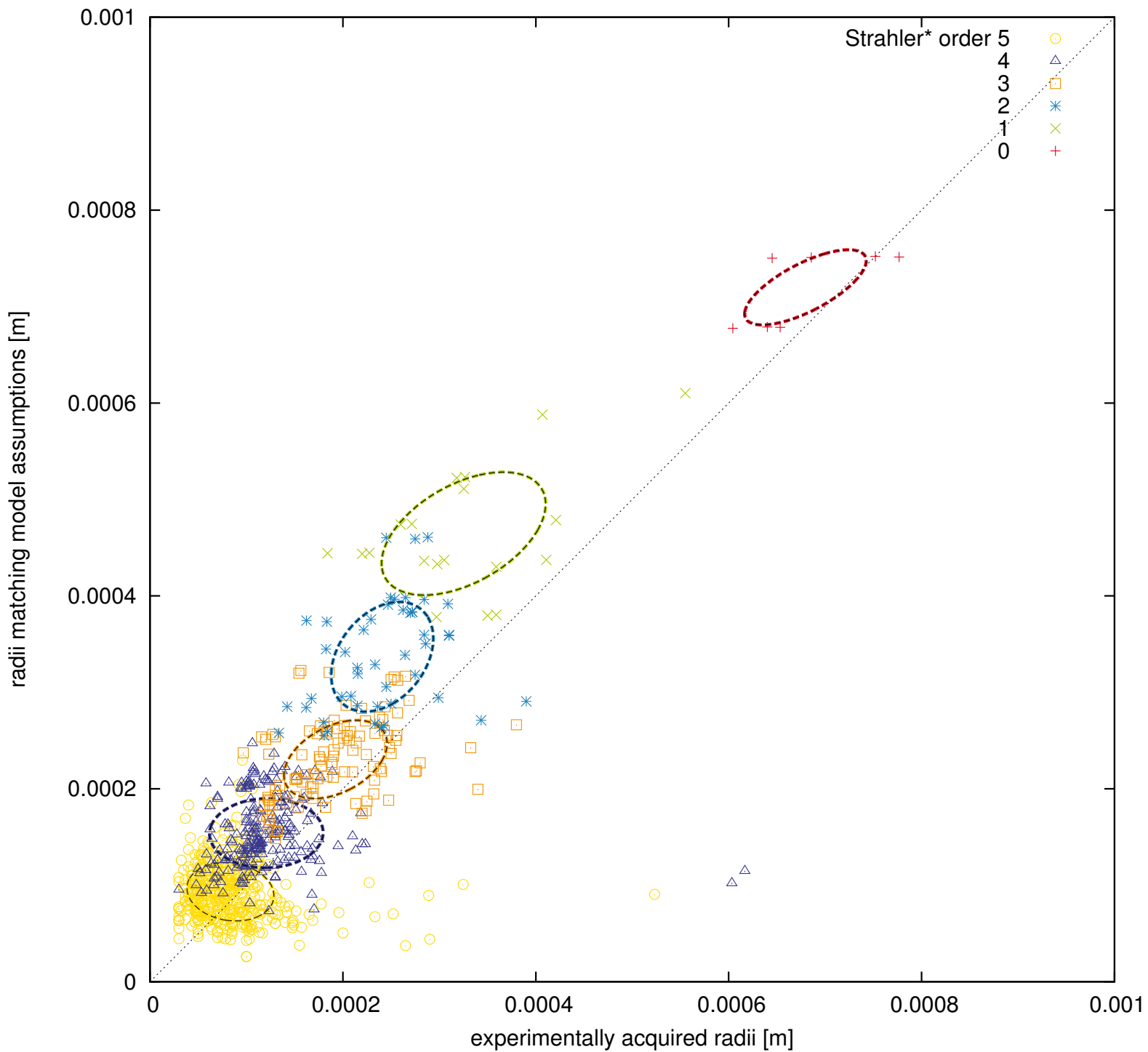
Mouse PV 10/12



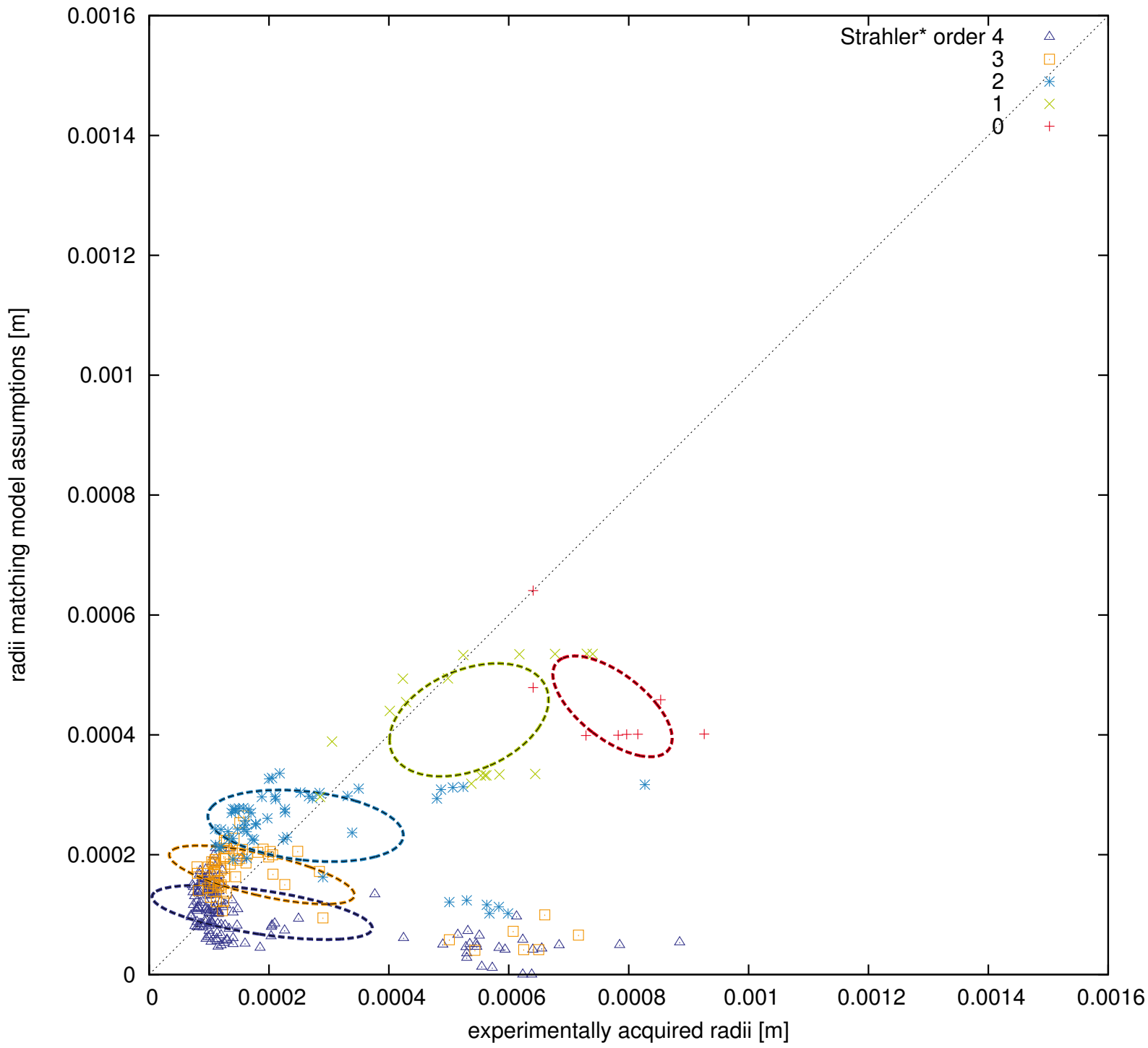
Mouse PV 11/12



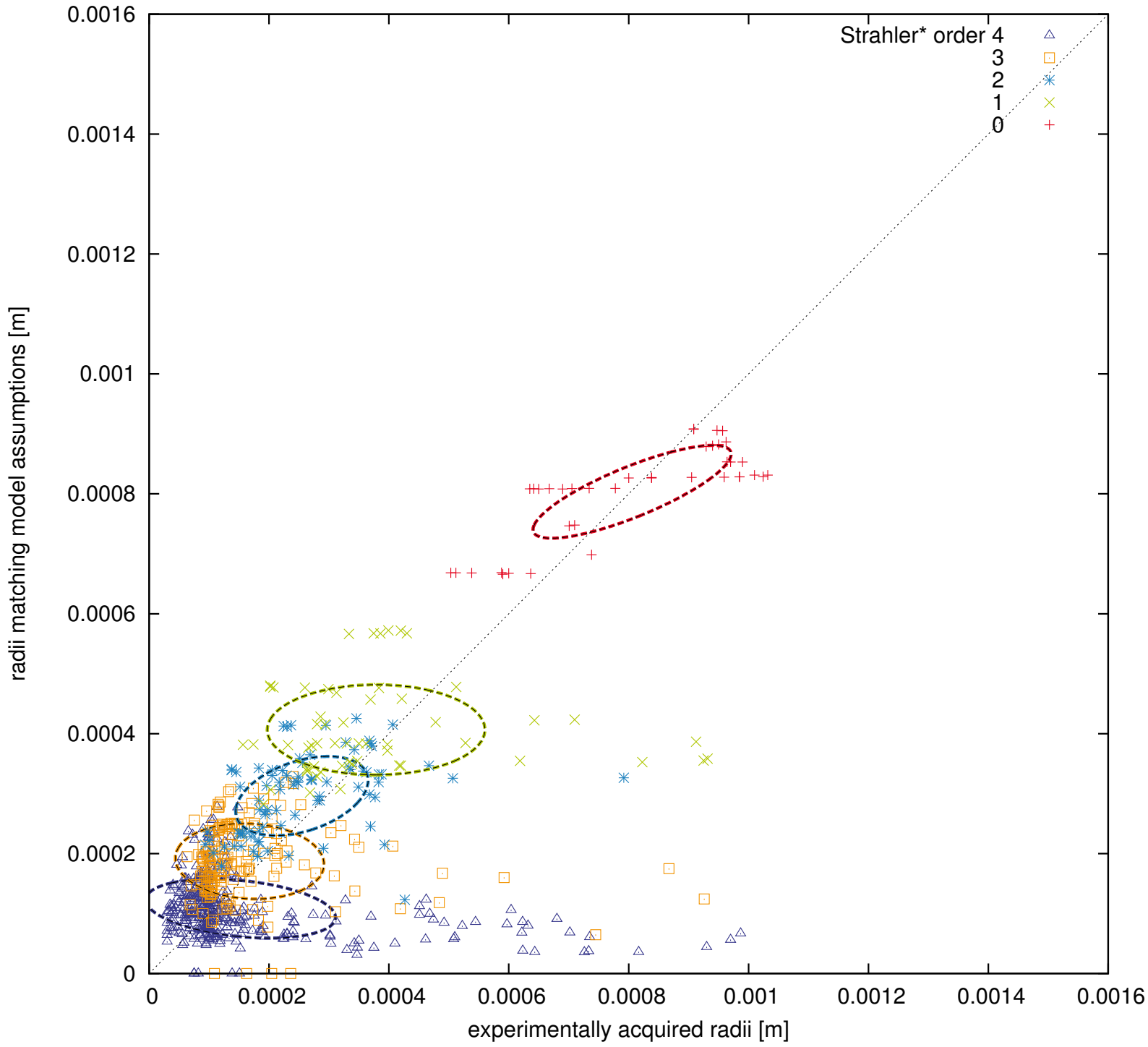
Mouse PV 12/12



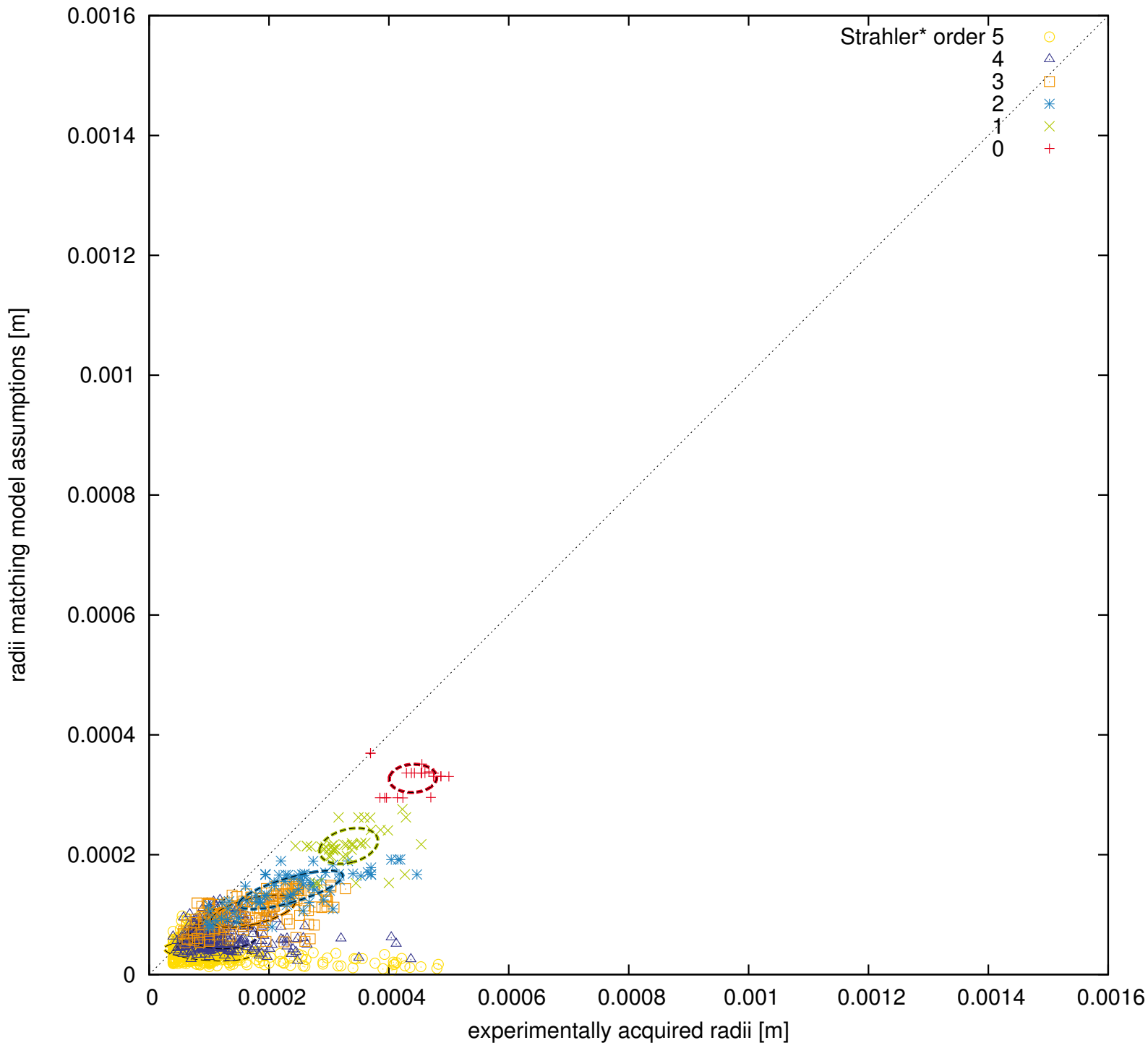
Mouse HV 1/12



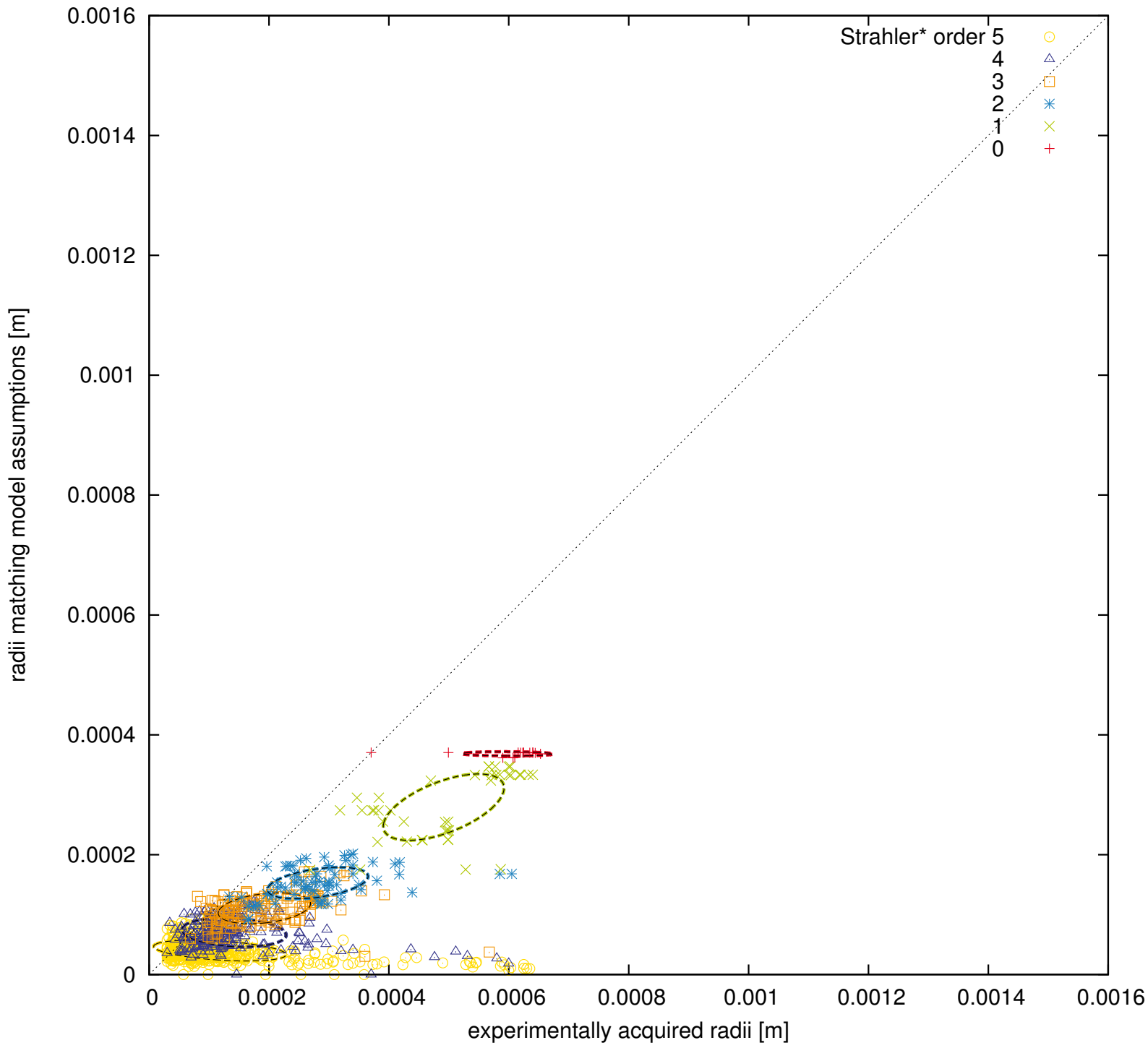
Mouse HV 2/12



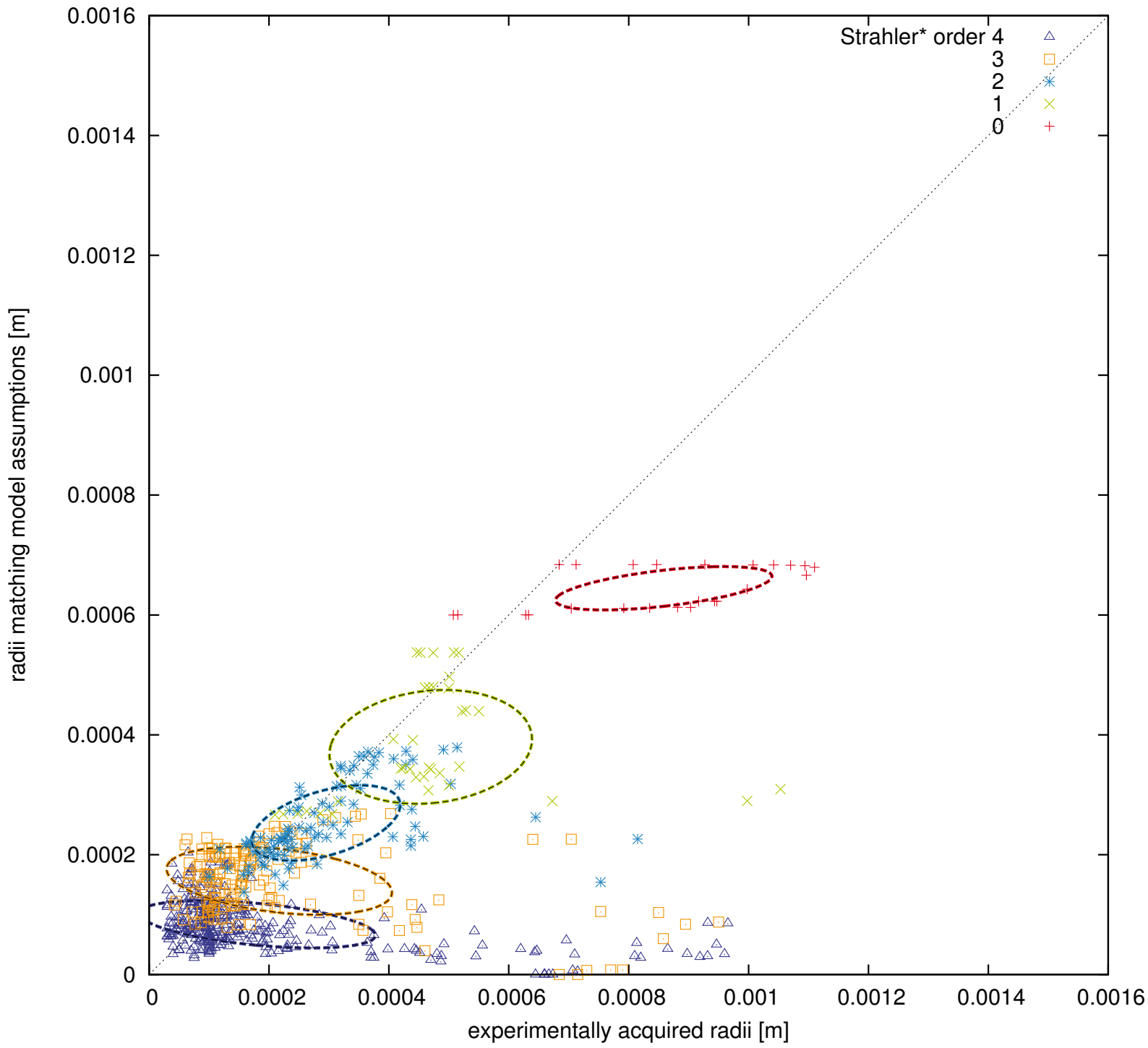
Mouse HV 3/12



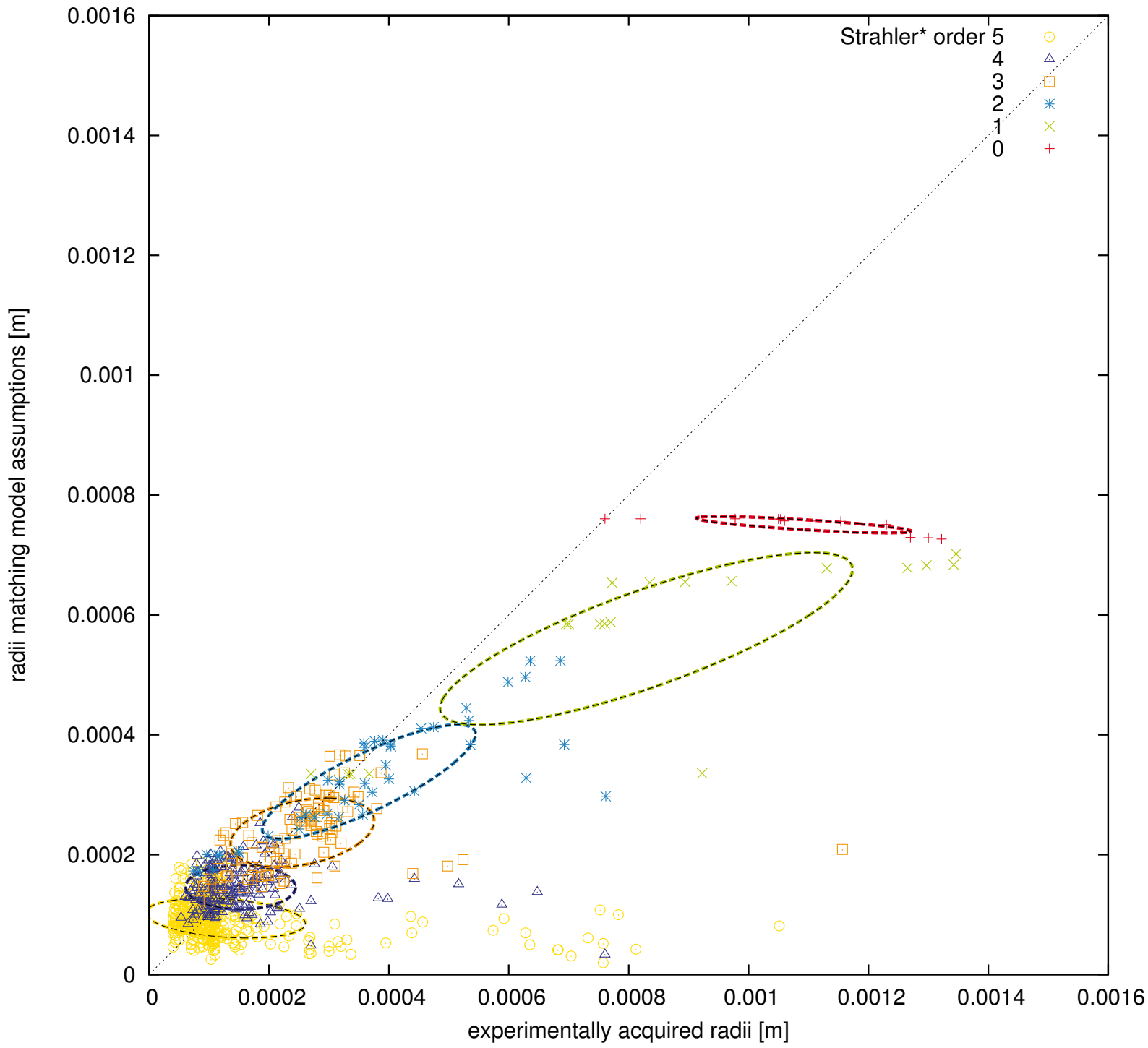
Mouse HV 4/12



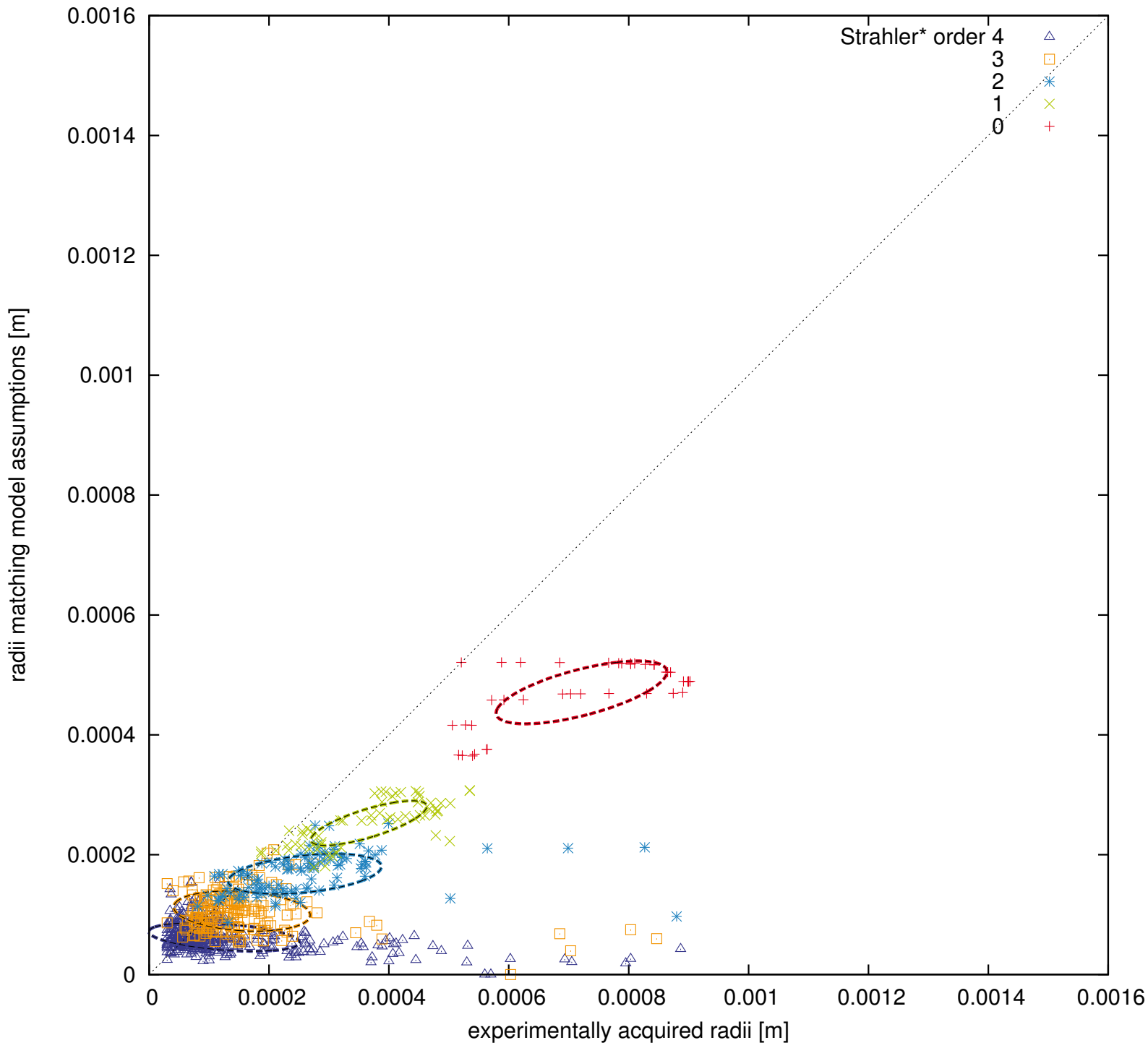
Mouse HV 5/12



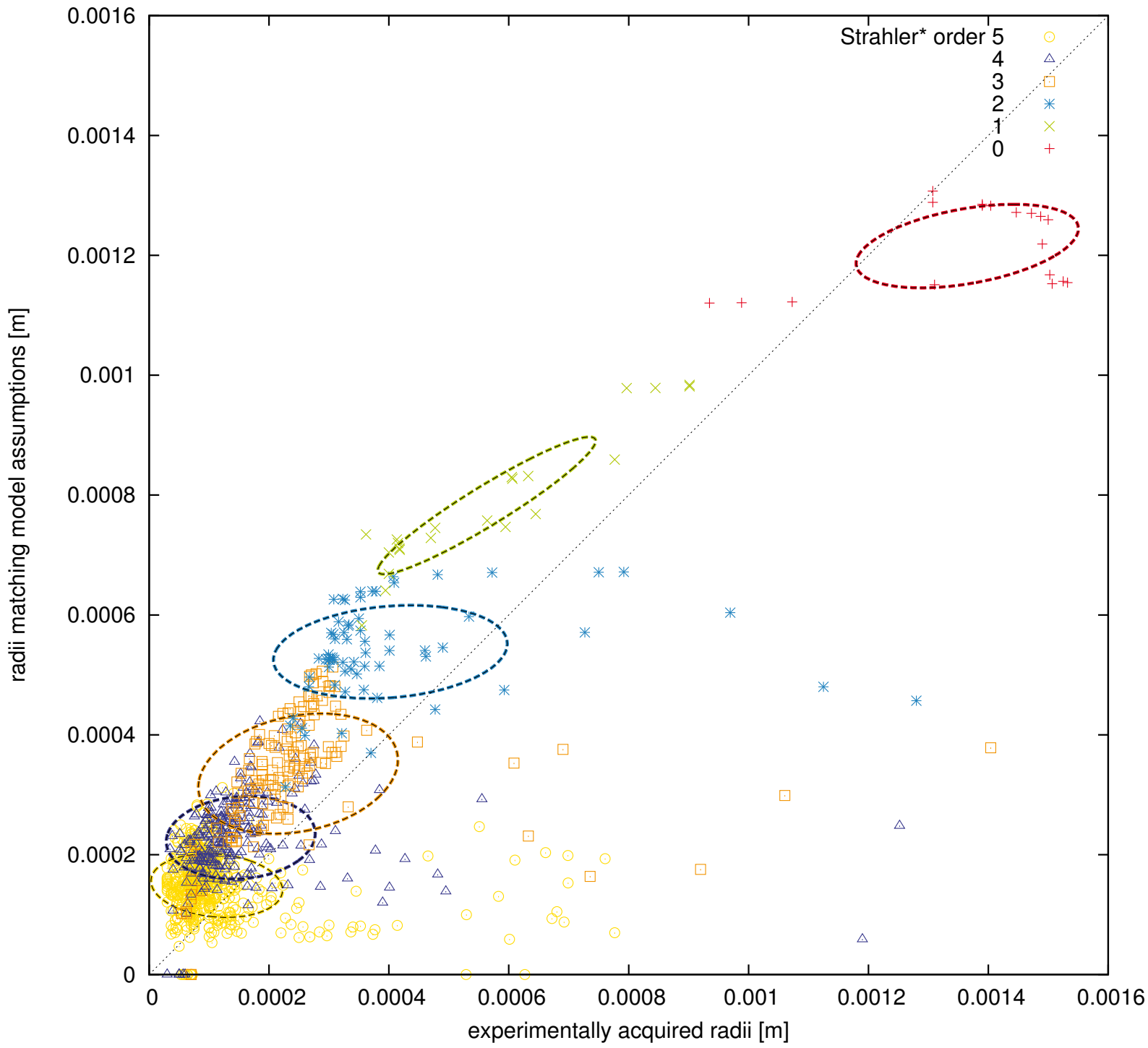
Mouse HV 6/12



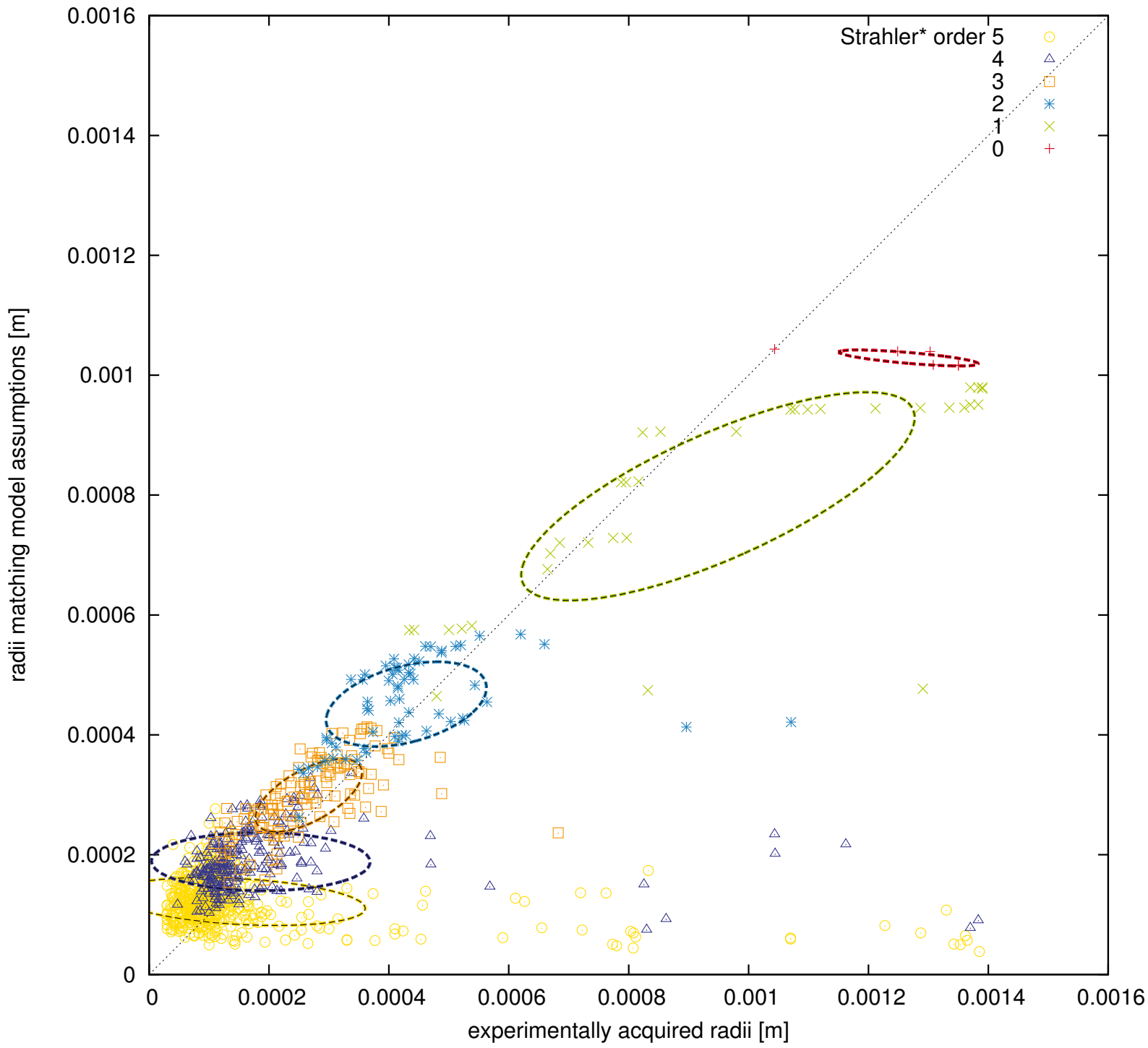
Mouse HV 7/12



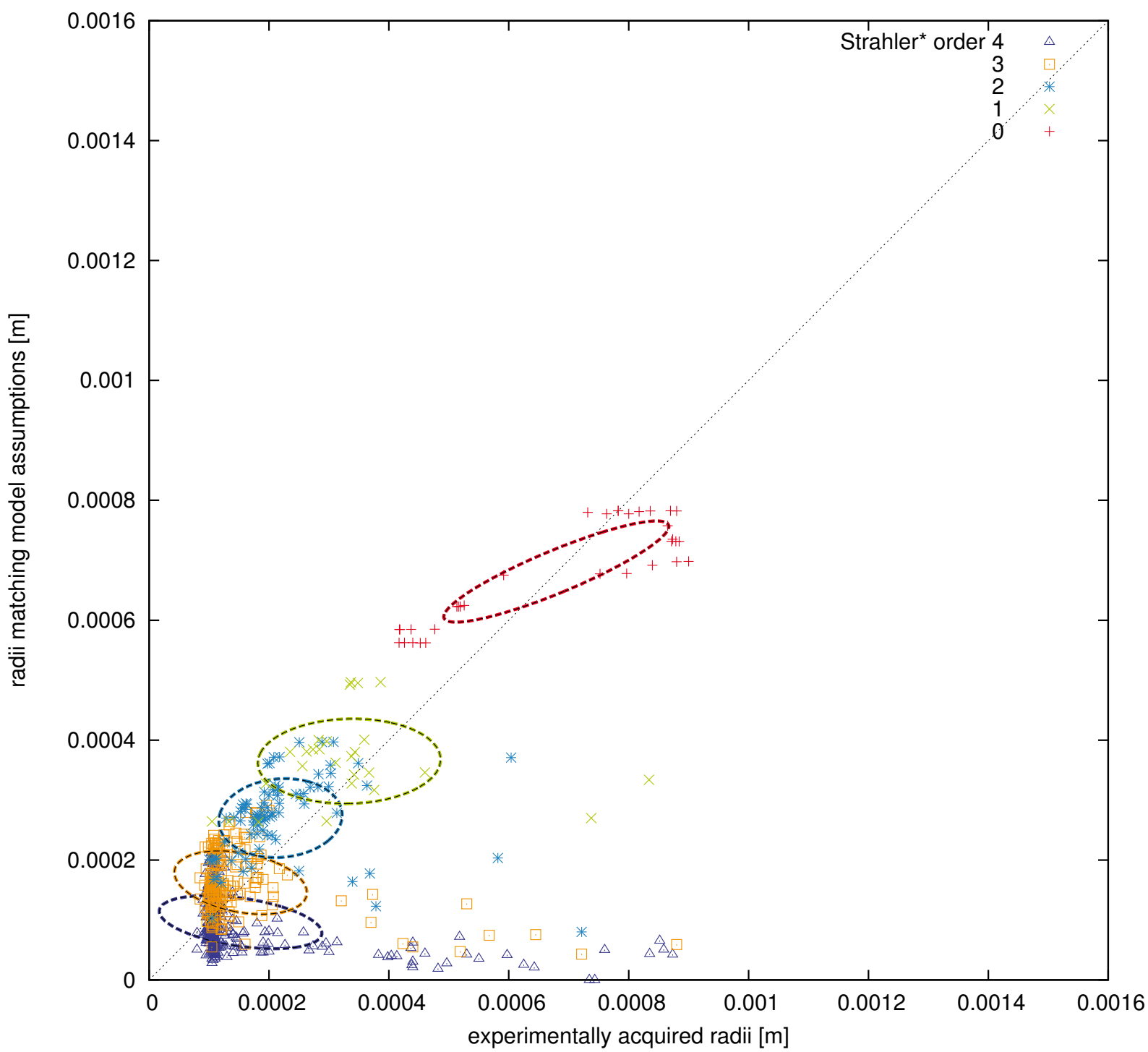
Mouse HV 8/12



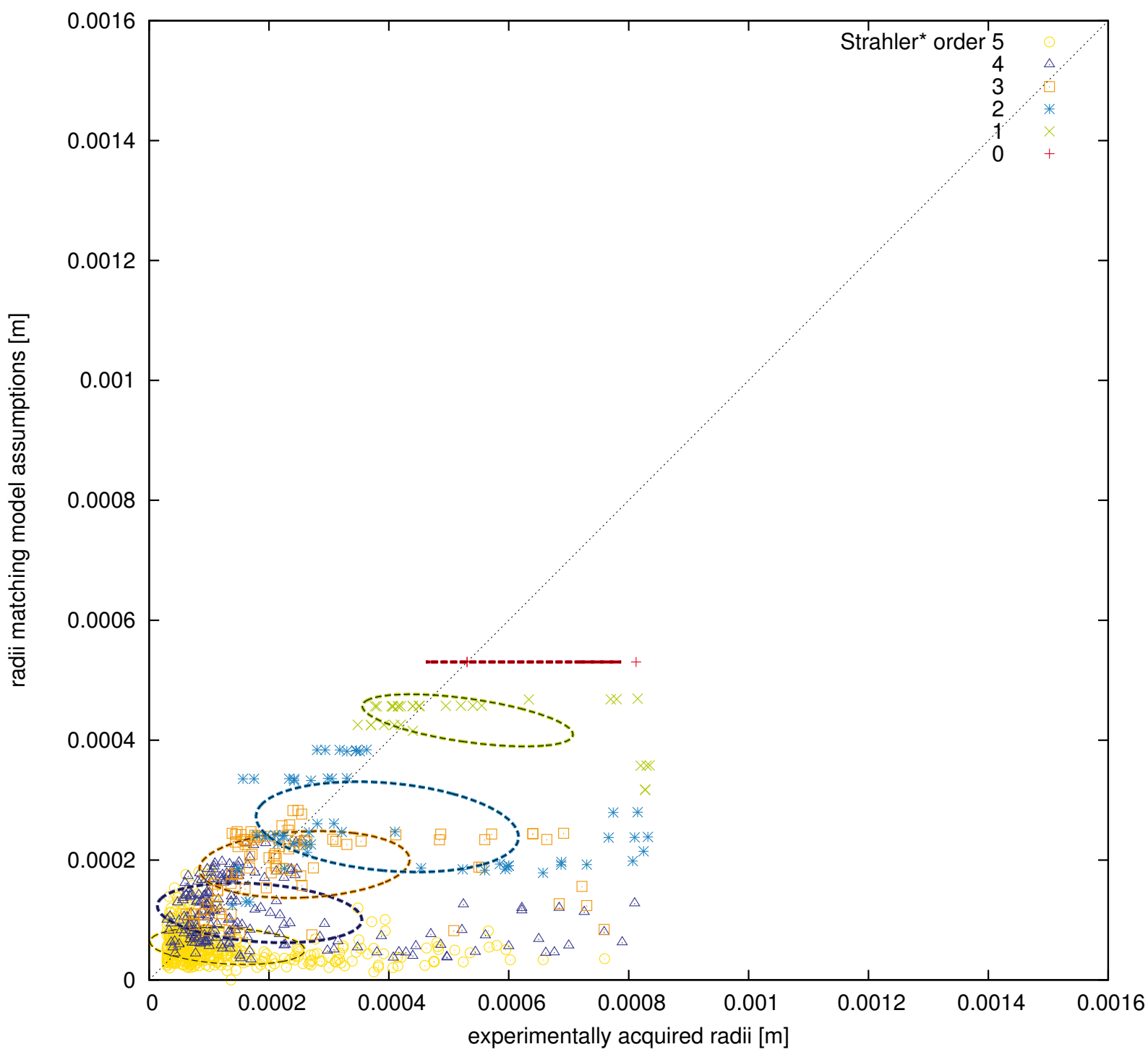
Mouse HV 9/12



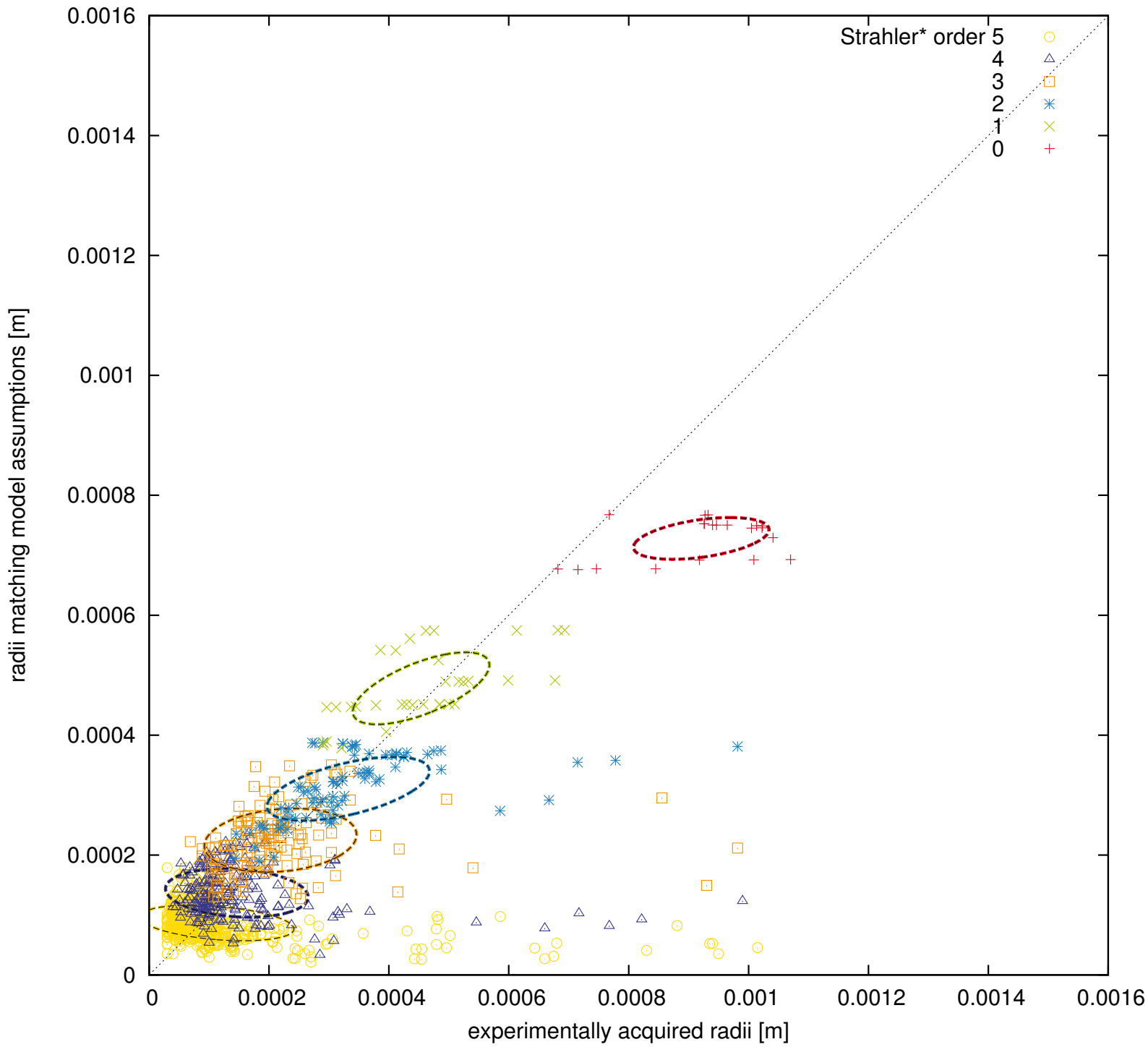
Mouse HV 10/12



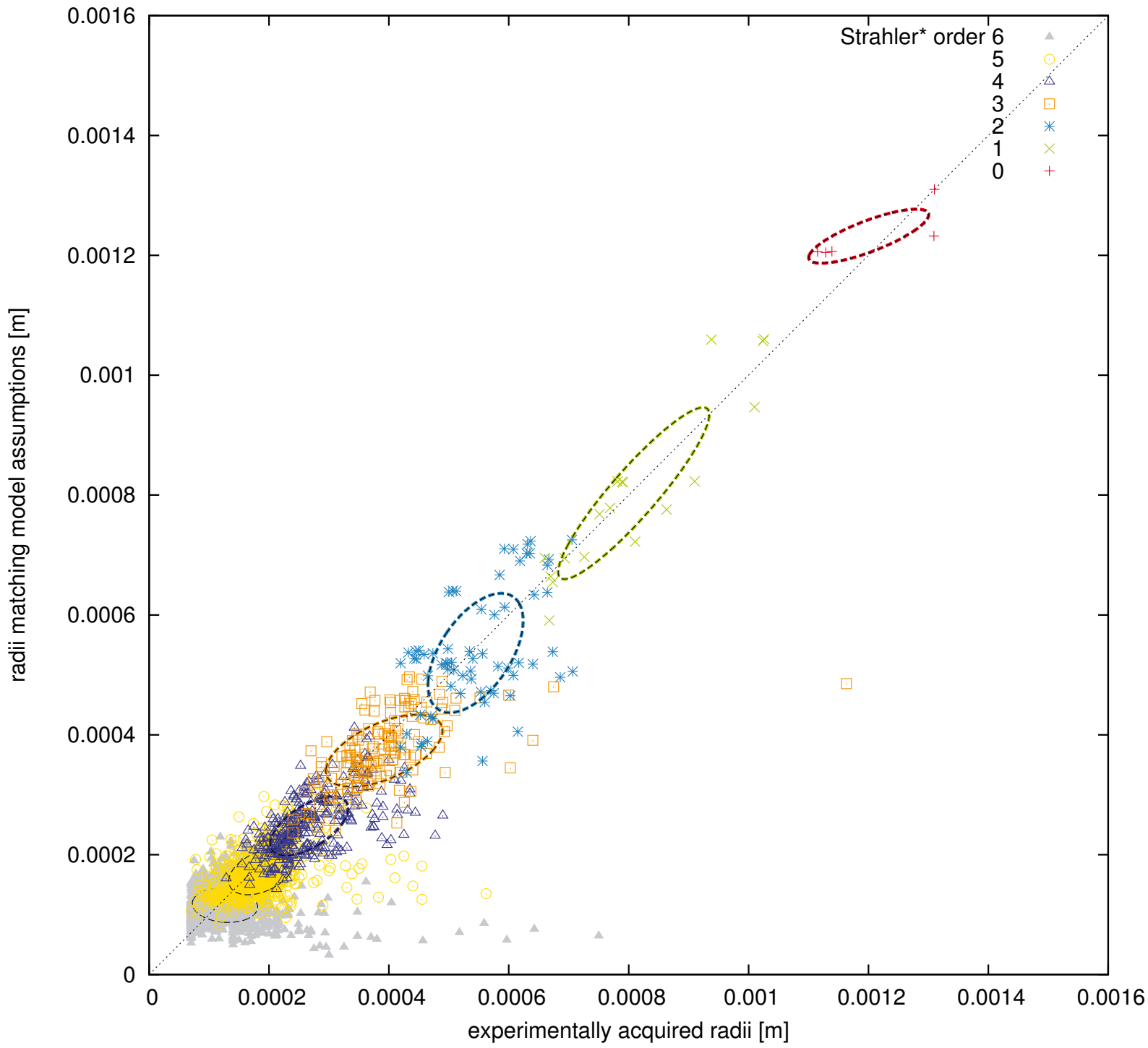
Mouse HV 11/12



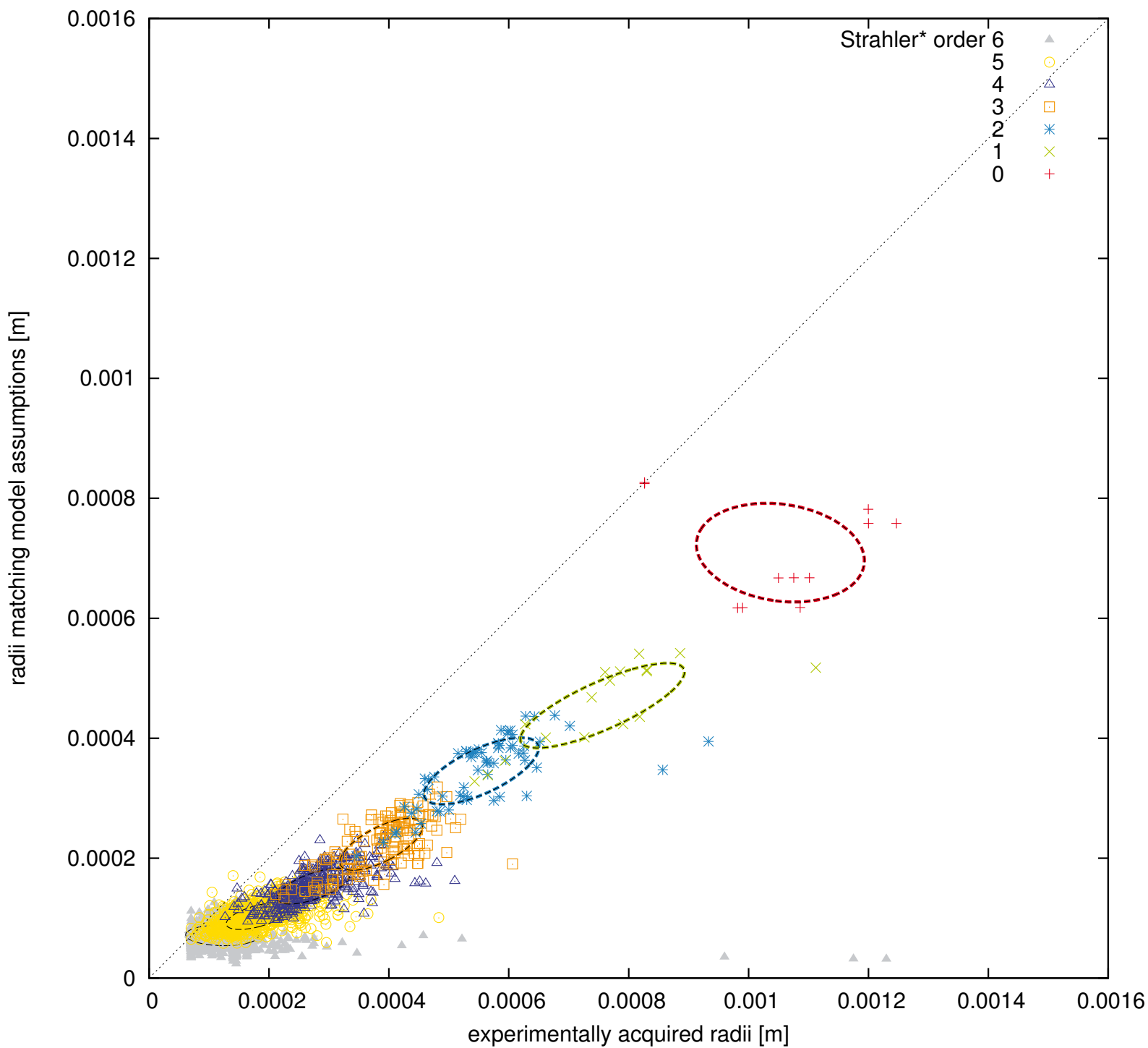
Mouse HV 12/12



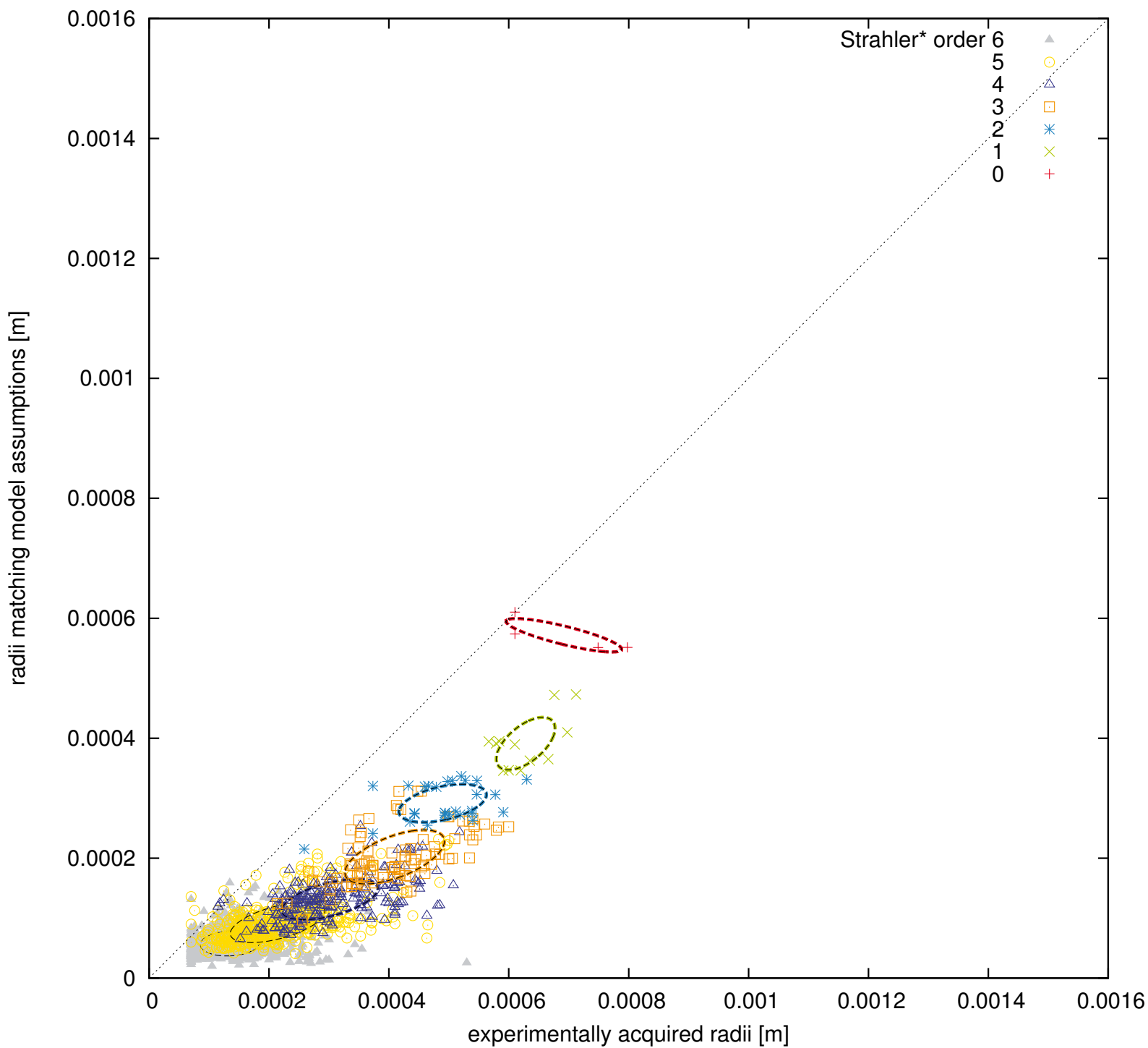
Rat PV 1/6



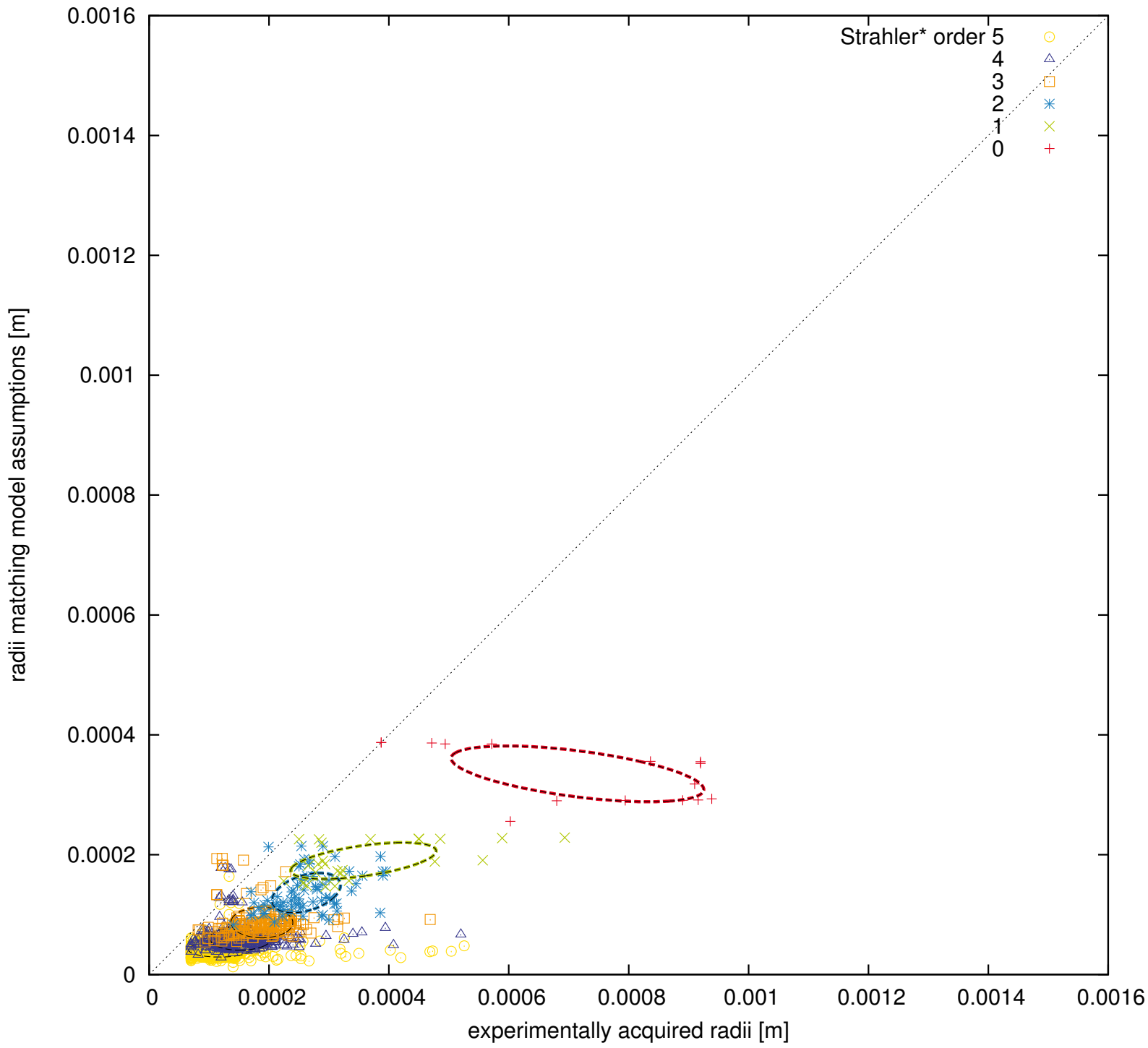
Rat PV 2/6



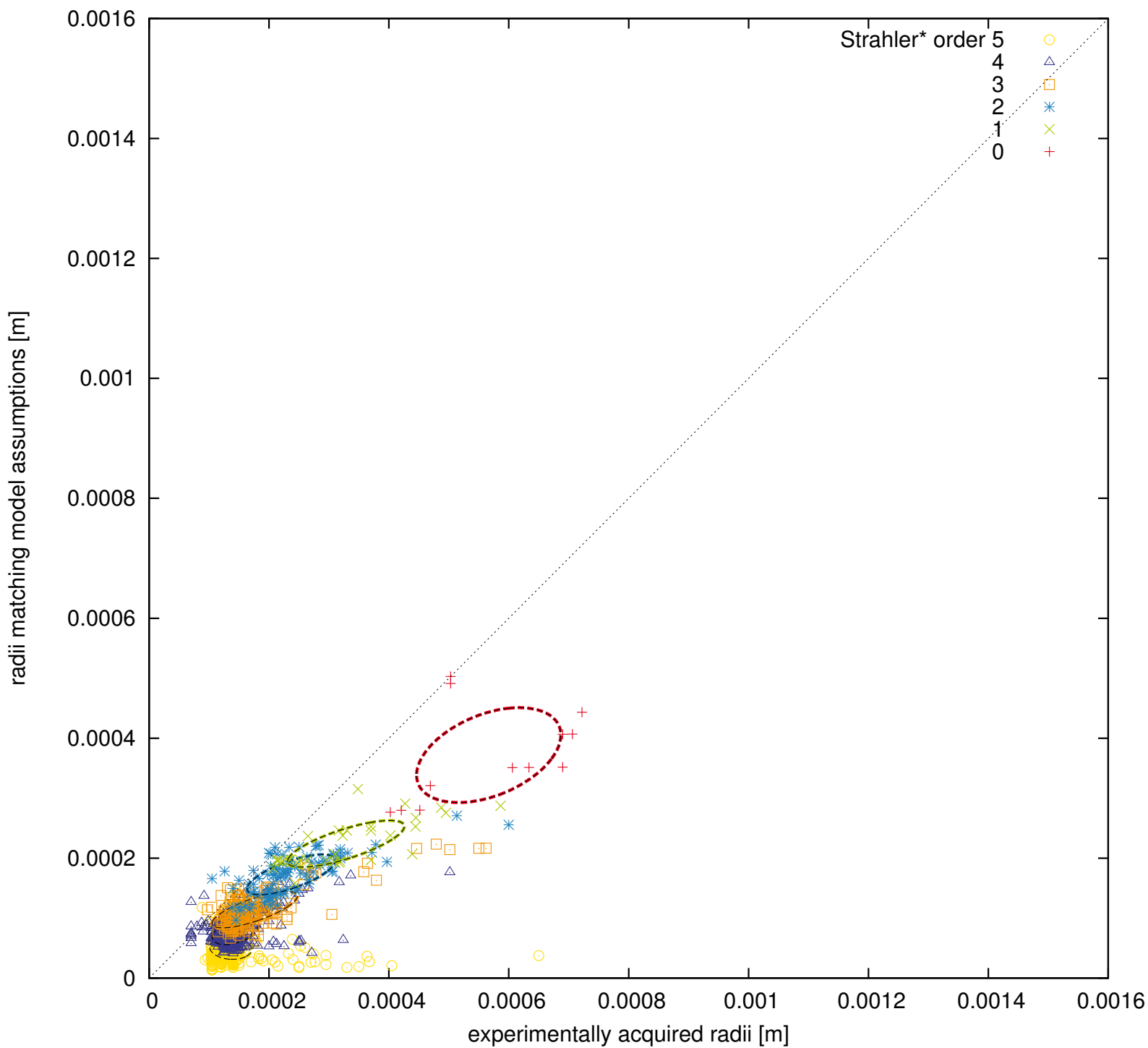
Rat PV 3/6



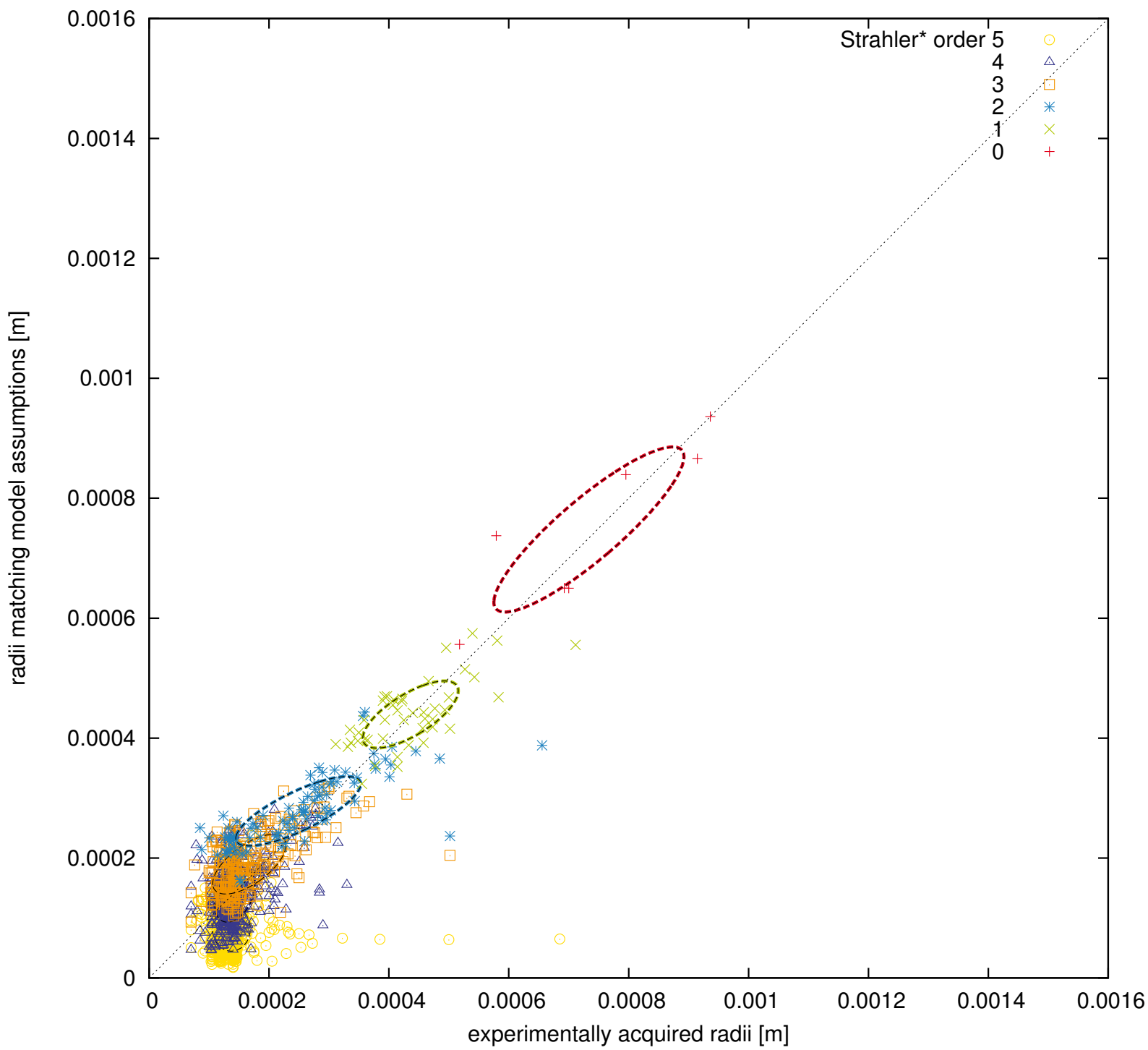
Rat PV 4/6



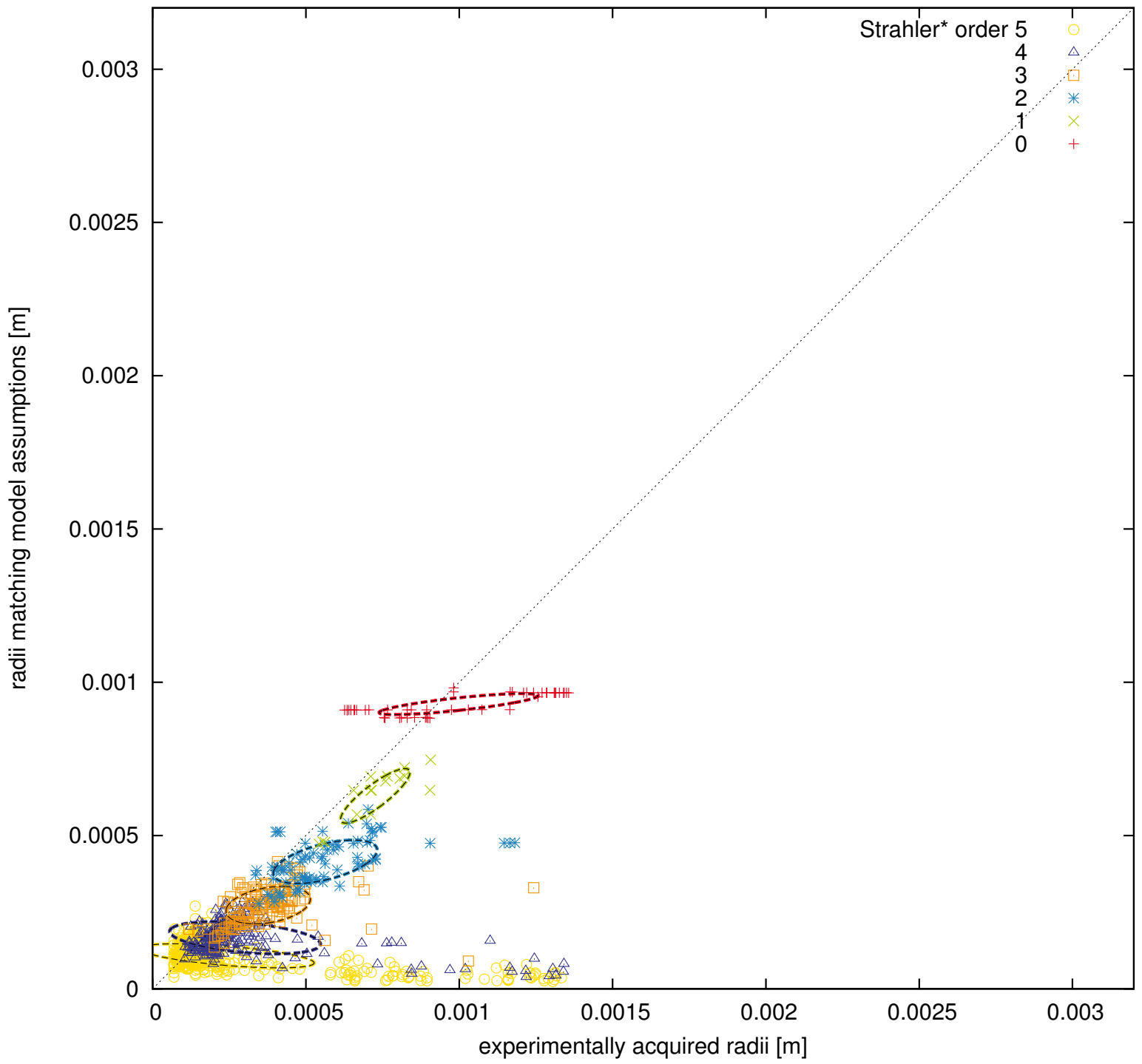
Rat PV 5/6



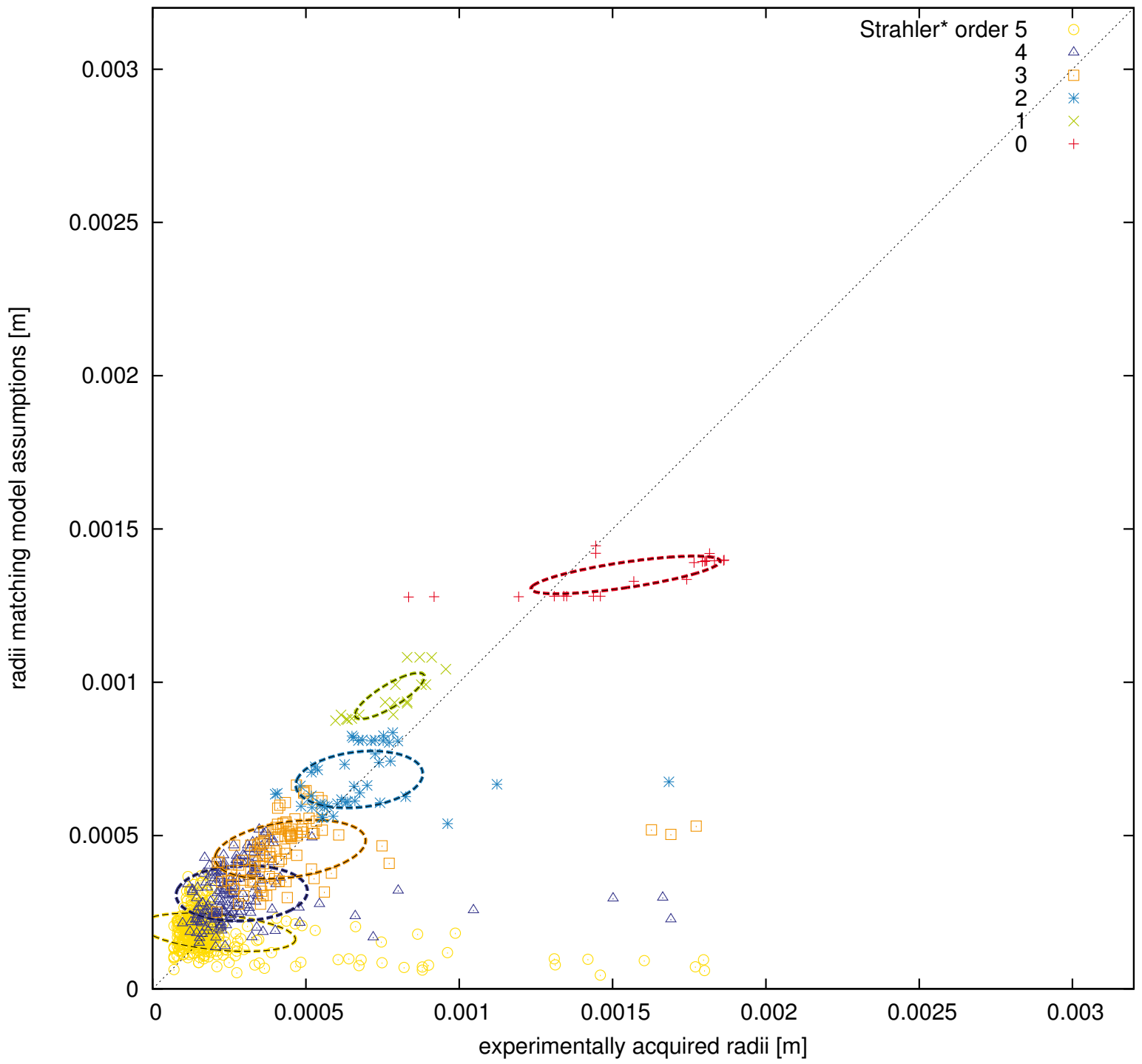
Rat PV 6/6



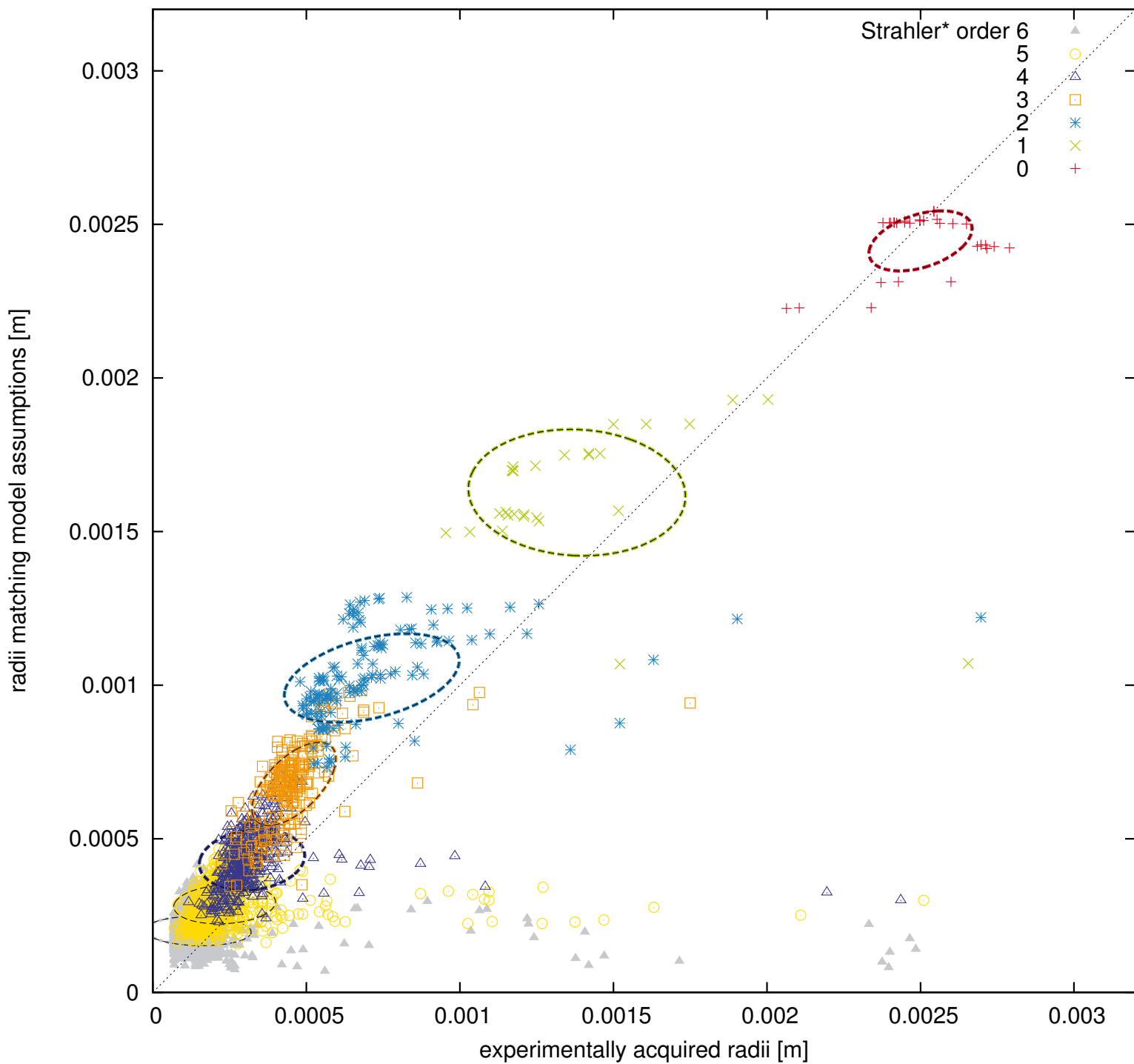
Rat HV 1/6



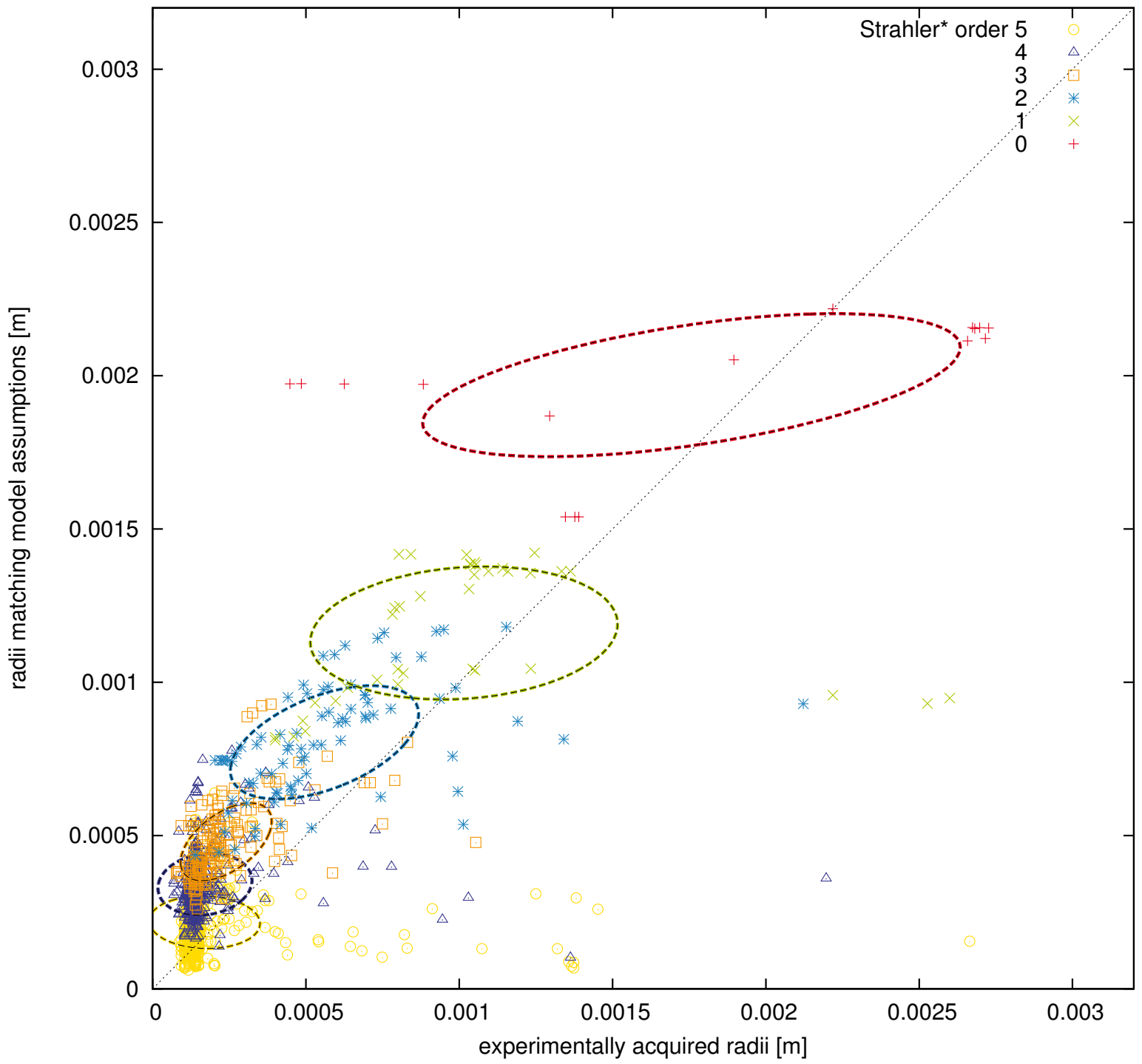
Rat HV 2/6



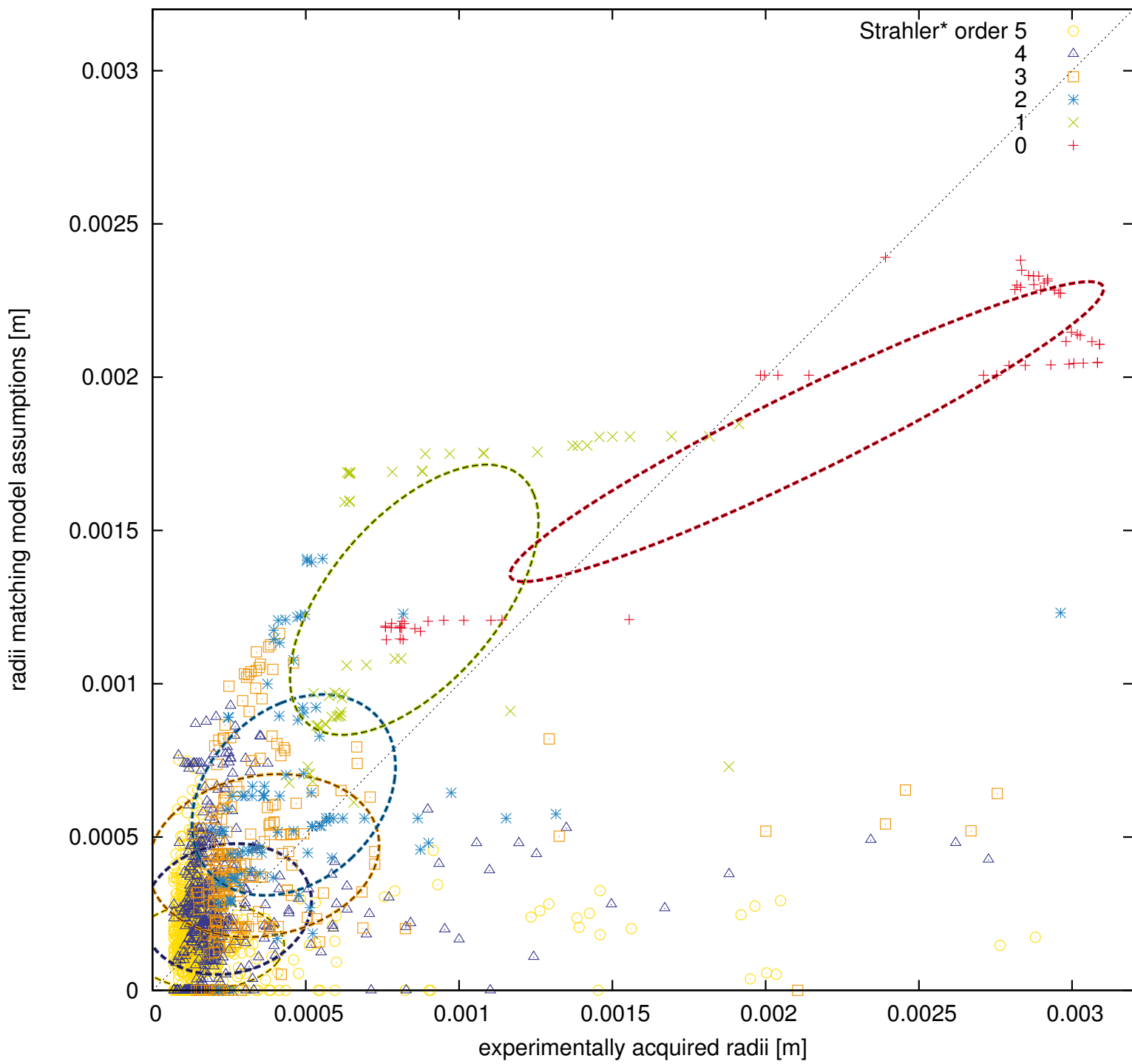
Rat HV 3/6



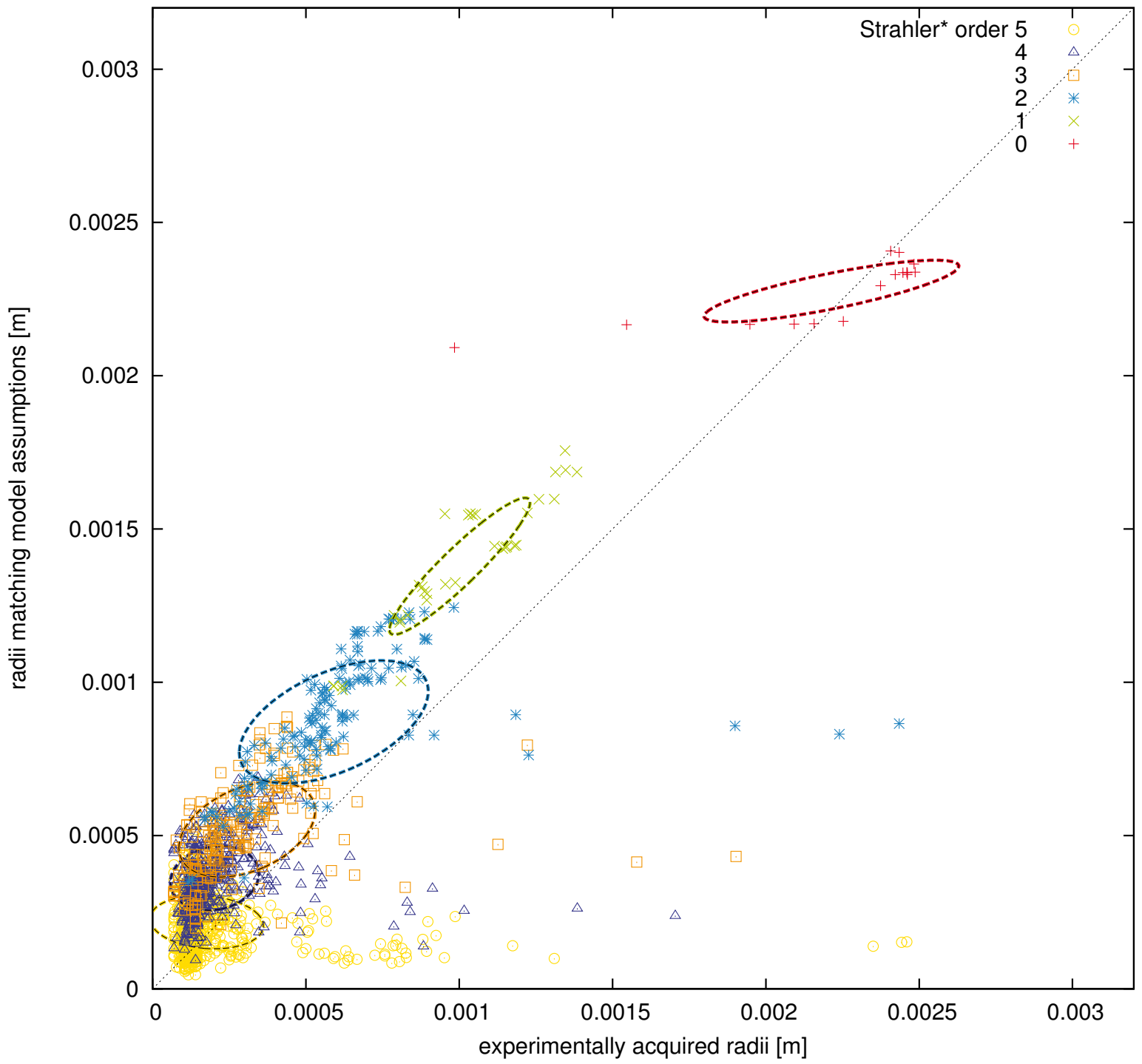
Rat HV 4/6



Rat HV 5/6



Rat HV 6/6



Algorithmically Generated Rodent Hepatic Vascular Trees in Arbitrary Detail
Supporting Information S2

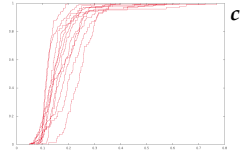
Interindividual Variations

Lars Ole Schwen Weiwei Wei Felix Gremse Josef Ehling
Lei Wang Uta Dahmen Tobias Preusser

Legend

Edge Radii: 0.174^a

Strahler* order ... 3 ...
similarity ... 0.152^b



\emptyset # edges / # trees $116.750^d / 12^e$
averaging weight 0.280^f

a similarity value for this geometric feature averaged over all Strahler* orders

b similarity value for this geometric feature and this Strahler* order

c plot of the cumulative distribution functions for all trees for this geometric feature and this Strahler* order

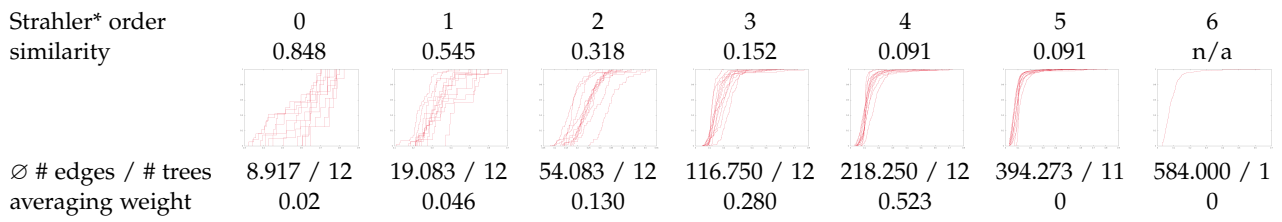
d average number of edges per vascular tree considered for *c*

e number of vascular trees considered for *c*

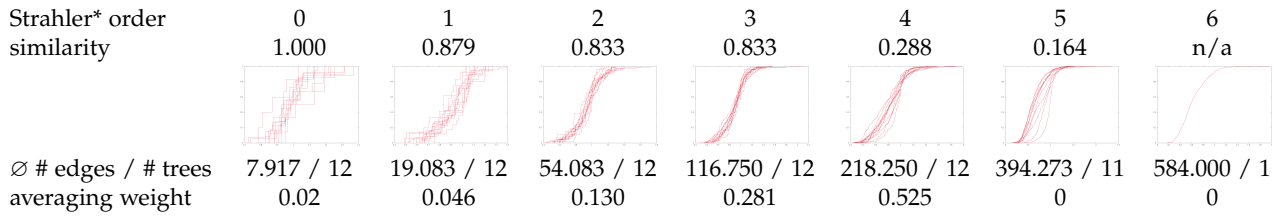
f averaging weight for *b* contributing to *a*

Interindividual Variations Mouse PV

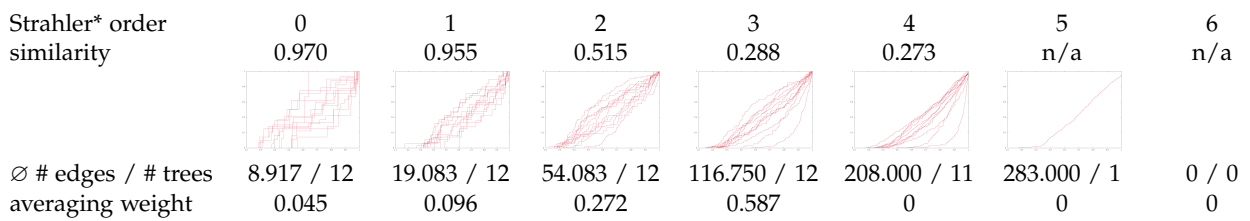
Edge Radii: 0.174



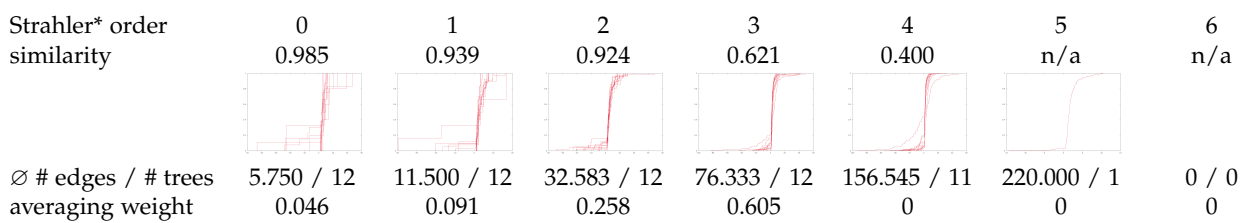
Radius Decrease: 0.552



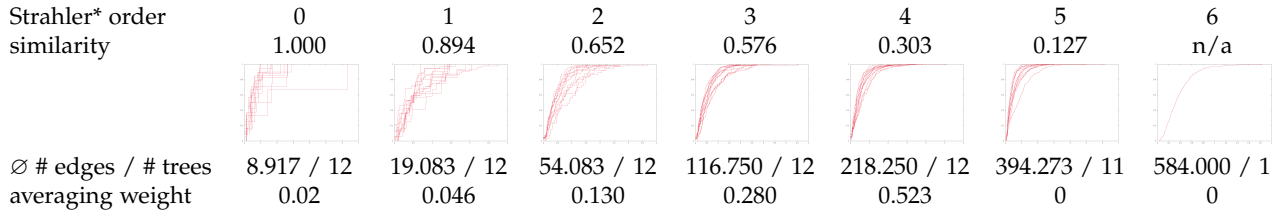
Radius Asymmetry: 0.444



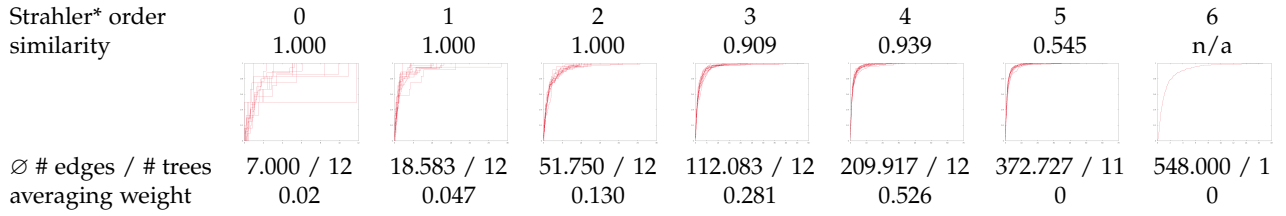
Bifurcation Exponent: 0.745



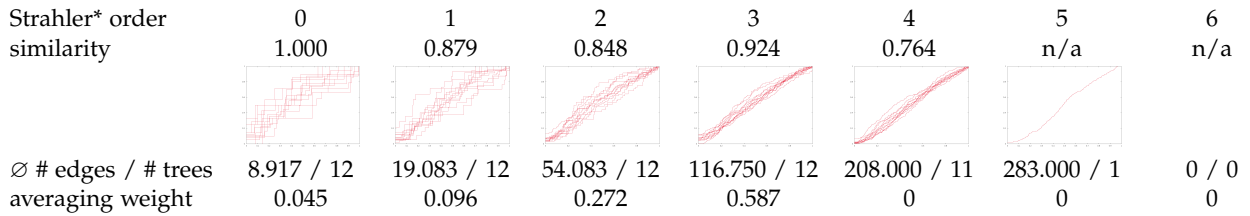
Edge Length: 0.466



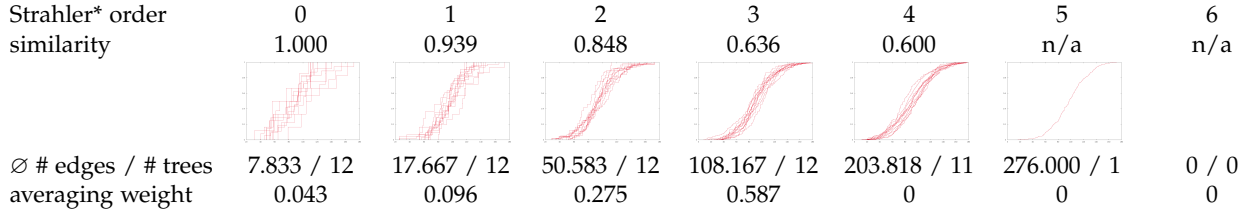
Length Decrease: 0.943



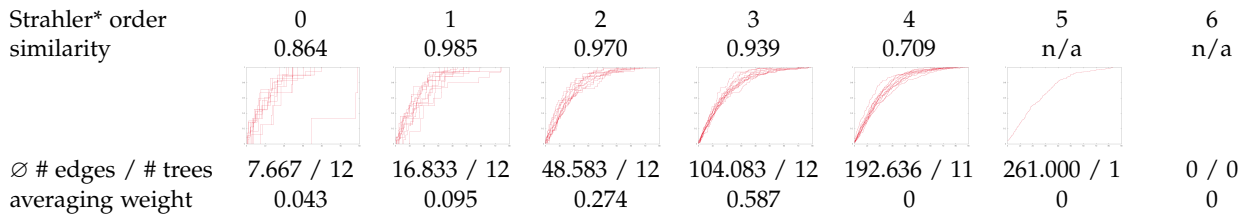
Length Asymmetry: 0.903



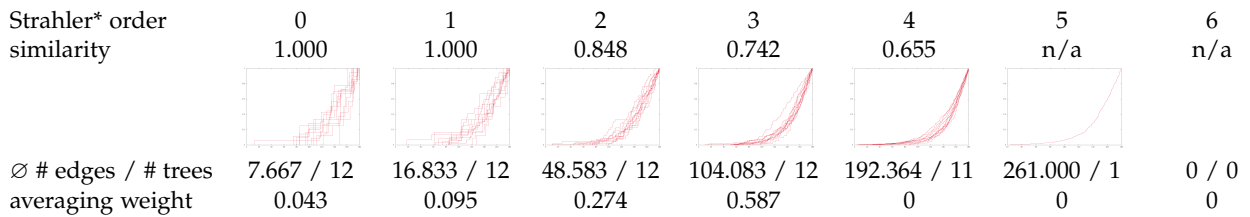
Angle φ_a : 0.739



Angle φ_b : 0.949

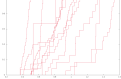
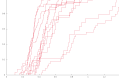
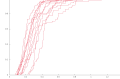
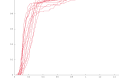
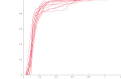
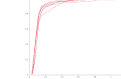


Angle φ_c : 0.807

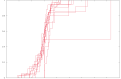
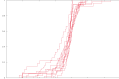
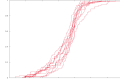
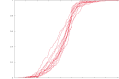
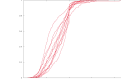
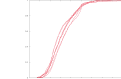


Interindividual Variations Mouse HV

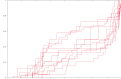
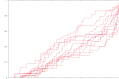
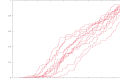
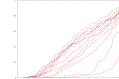
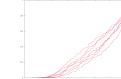
Edge Radii: 0.129

similarity	0.197	0.258	0.152	0.076	0.167	0.190
Strahler* order	0	1	2	3	4	5
						
Ø # edges / # trees	19.833 / 12	35.000 / 12	73.750 / 12	138.833 / 12	258.750 / 12	469.714 / 7
averaging weight	0.074	0.131	0.276	0.519	0	0

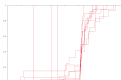
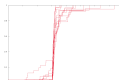
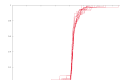
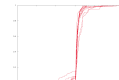
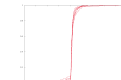
Radius Decrease: 0.647

similarity	0.894	0.727	0.652	0.591	0.197	0.286
Strahler* order	0	1	2	3	4	5
						
Ø # edges / # trees	18.833 / 12	35.000 / 12	73.750 / 12	138.833 / 12	258.750 / 12	469.714 / 7
averaging weight	0.071	0.131	0.277	0.521	0	0

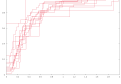
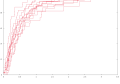
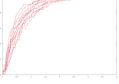
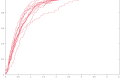
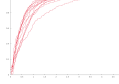
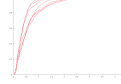
Radius Asymmetry: 0.466

similarity	0.833	0.773	0.500	0.318	0.476	n/a
Strahler* order	0	1	2	3	4	5
						
Ø # edges / # trees	19.833 / 12	35.000 / 12	73.750 / 12	138.833 / 12	226.571 / 7	0 / 0
averaging weight	0.074	0.131	0.276	0.519	0	0


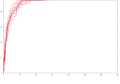

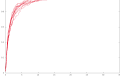
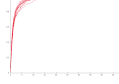
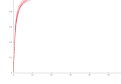
Bifurcation Exponent: 0.613

similarity	1.000	0.758	0.833	0.439	0.810	n/a
Strahler* order	0	1	2	3	4	5
						
Ø # edges / # trees	9.917 / 12	23.917 / 12	50.000 / 12	105.000 / 12	188.714 / 7	0 / 0
averaging weight	0.053	0.127	0.265	0.556	0	0

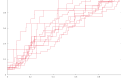
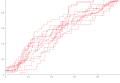
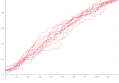
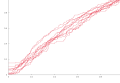
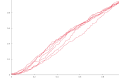
Edge Length: 0.730

similarity	0.924	0.788	0.712	0.697	0.333	0.286
Strahler* order	0	1	2	3	4	5
						
∅ # edges / # trees	19.833 / 12	35.000 / 12	73.750 / 12	138.833 / 12	258.750 / 12	469.714 / 7
averaging weight	0.074	0.131	0.276	0.519	0	0

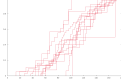
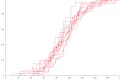
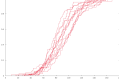
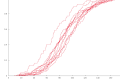
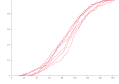
Length Decrease: 0.978

similarity	1.000	0.955	1.000	0.970	0.864	0.762
Strahler* order	0	1	2	3	4	5
						
∅ # edges / # trees	18.455 / 11	34.000 / 12	71.583 / 12	134.917 / 12	246.833 / 12	440.714 / 7
averaging weight	0.066	0.132	0.278	0.524	0	0

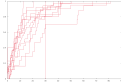
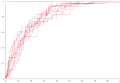
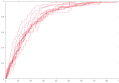
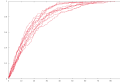
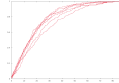
Length Asymmetry: 0.871

similarity 0.879	0.909	0.894	0.848	0.571	n/a	
Strahler* order	0	1	2	3	4	5
						
∅ # edges / # trees	19.833 / 12	35.000 / 12	73.750 / 12	138.833 / 12	226.571 / 7	0 / 0
averaging weight	0.074	0.131	0.276	0.519	0	0

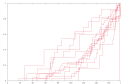

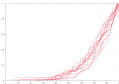


Angle φ_a : 0.575

similarity	0.864	0.985	0.561	0.439	0.476	n/a
Strahler* order	0	1	2	3	4	5
						
∅ # edges / # trees	17.833 / 12	33.167 / 12	68.500 / 12	131.500 / 12	223.714 / 7	0 / 0
averaging weight	0.071	0.132	0.273	0.524	0	0

Angle φ_b : 0.841

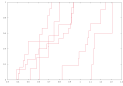
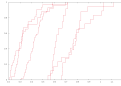
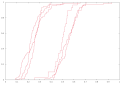
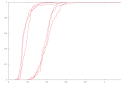
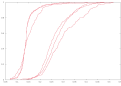
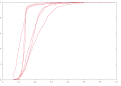
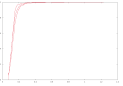
similarity	0.803	0.939	0.818	0.833	0.667	n/a
Strahler* order	0	1	2	3	4	5
						
∅ # edges / # trees	16.833 / 12	32.000 / 12	66.833 / 12	126.083 / 12	208.857 / 7	0 / 0
averaging weight	0.070	0.132	0.276	0.522	0	0

Angle φ_c : 0.661

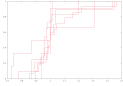
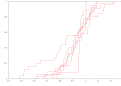
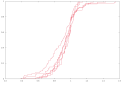
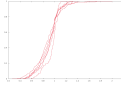
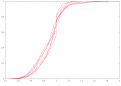
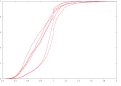
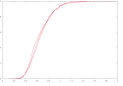
similarity	0.879	0.818	0.833	0.500	0.762	n/a
Strahler* order	0	1	2	3	4	5
						
∅ # edges / # trees	16.833 / 12	32.000 / 12	66.750 / 12	126.083 / 12	208.857 / 7	0 / 0
averaging weight	0.070	0.132	0.276	0.522	0	0

Interindividual Variations Rat PV

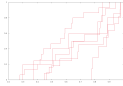
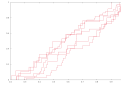
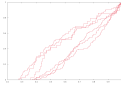
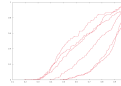
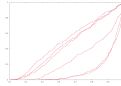
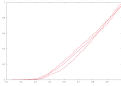
Edge Radii: 0.091

similarity	0.333	0.133	0.067	0.133	0.067	0	0
Strahler* order	0	1	2	3	4	5	6
							
Ø # edges / # trees	9.000 / 6	24.667 / 6	69.167 / 6	162.167 / 6	342.667 / 6	677.500 / 6	1117.000 / 3
averaging weight	0.01	0.041	0.114	0.267	0.564	0	0

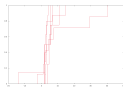
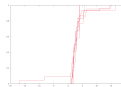
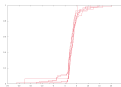
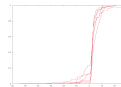
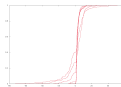
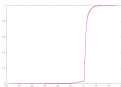
Radius Decrease: 0.392

similarity							
Strahler* order	0	1	2	3	4	5	6
							
Ø # edges / # trees	8.000 / 6	24.667 / 6	69.167 / 6	162.167 / 6	342.667 / 6	677.500 / 6	1117.000 / 3
averaging weight	0.01	0.041	0.114	0.267	0.565	0	0

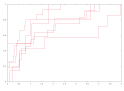
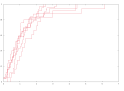
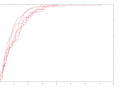
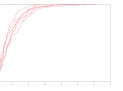
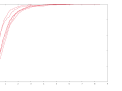
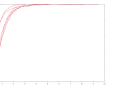
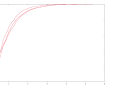
Radius Asymmetry: 0.235

similarity	0.867	0.933	0.333	0.267	0.133	0.667	n/a
Strahler* order	0	1	2	3	4	5	6
							
Ø # edges / # trees	9.000 / 6	24.667 / 6	69.167 / 6	162.167 / 6	342.667 / 6	627.333 / 3	0 / 0
averaging weight	0.01	0.041	0.114	0.267	0.564	0	0

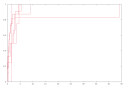
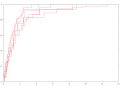
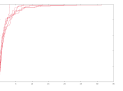
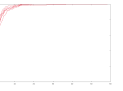
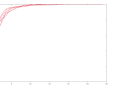
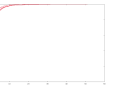
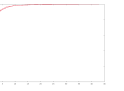
Bifurcation Exponent: 0.381

similarity	1.000	1.000	1.000	0.400	0.200	0.667	n/a
Strahler* order	0	1	2	3	4	5	6
							
Ø # edges / # trees	5.667 / 6	16.333 / 6	44.333 / 6	96.667 / 6	237.000 / 6	523.667 / 3	0 / 0
averaging weight	0.01	0.041	0.111	0.242	0.593	0	0

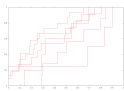
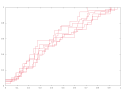
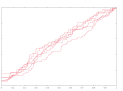
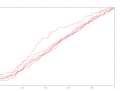
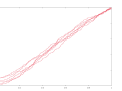
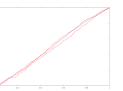
Edge Length: 0.489

similarity	1.000	0.933	0.933	0.533	0.333	0.200	0
Strahler* order	0	1	2	3	4	5	6
							
∅ # edges / # trees	9.000 / 6	24.667 / 6	69.167 / 6	162.167 / 6	342.667 / 6	677.500 / 6	1117.000 / 3
averaging weight	0.01	0.041	0.114	0.267	0.564	0	0

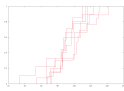
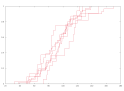
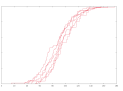
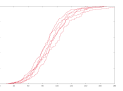
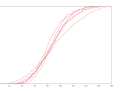
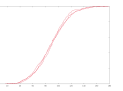
Length Decrease: 0.810

similarity	1.000	1.000	1.000	1.000	0.667	0.400	0.333
Strahler* order	0	1	2	3	4	5	6
							
∅ # edges / # trees	6.333 / 6	23.167 / 6	65.667 / 6	153.333 / 6	327.833 / 6	633.000 / 6	1058.000 / 3
averaging weight	0.01	0.040	0.114	0.266	0.569	0	0

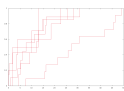
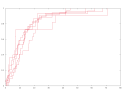
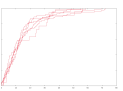
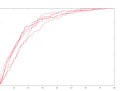
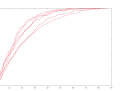
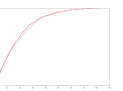
Length Asymmetry: 0.720

similarity	0.800	1.000	1.000	0.667	0.667	0.667	n/a
Strahler* order	0	1	2	3	4	5	6
							
∅ # edges / # trees	9.000 / 6	24.667 / 6	69.167 / 6	162.167 / 6	342.667 / 6	627.333 / 3	0 / 0
averaging weight	0.01	0.041	0.114	0.267	0.564	0	0

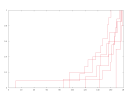


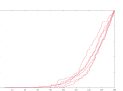
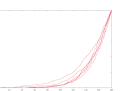
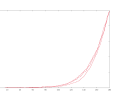
Angle φ_a : 0.562

similarity	1.000	0.867	0.800	0.600	0.467	1.000	n/a
Strahler* order	0	1	2	3	4	5	6
							
∅ # edges / # trees	7.833 / 6	23.167 / 6	62.833 / 6	144.333 / 6	323.667 / 6	616.000 / 3	0 / 0
averaging weight	0.01	0.041	0.112	0.257	0.576	0	0

Angle φ_b : 0.489

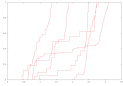
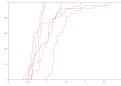
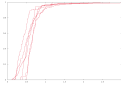
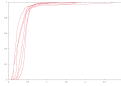
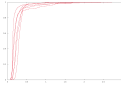
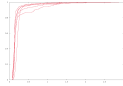
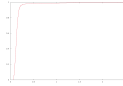
similarity	0.800	0.867	1.000	0.533	0.333	1.000	n/a
Strahler* order	0	1	2	3	4	5	6
							
∅ # edges / # trees	6.833 / 6	22.167 / 6	59.667 / 6	136.833 / 6	301.333 / 6	584.333 / 3	0 / 0
averaging weight	0.01	0.042	0.113	0.260	0.572	0	0

Angle φ_c : 0.641

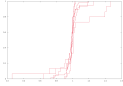
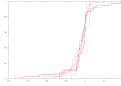
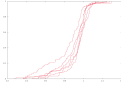
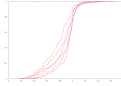
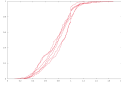
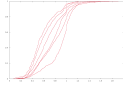
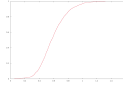
similarity	0.867	0.867	0.867	0.733	0.533	1.000	n/a
Strahler* order	0	1	2	3	4	5	6
							
∅ # edges / # trees	6.833 / 6	22.167 / 6	59.667 / 6	136.833 / 6	301.000 / 6	583.333 / 3	0 / 0
averaging weight	0.01	0.042	0.113	0.260	0.572	0	0

Interindividual Variations Rat HV

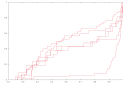
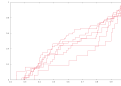
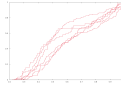
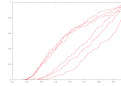
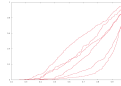
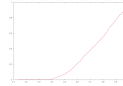

Edge Radii: 0.03

similarity	0.067	0.200	0.133	0	0	0	n/a
Strahler* order	0	1	2	3	4	5	6
							
∅ # edges / # trees	31.833 / 6	31.333 / 6	96.500 / 6	174.833 / 6	371.500 / 6	727.000 / 6	1758.000 / 1
averaging weight	0.045	0.044	0.137	0.248	0.526	0	0

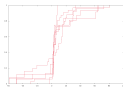
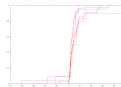
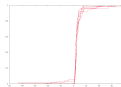
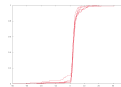
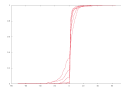
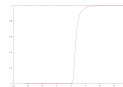

Radius Decrease: 0.392

similarity	0.800	1.000	0.400	0.333	0.333	0	n/a
Strahler* order	0	1	2	3	4	5	6
							
∅ # edges / # trees	30.833 / 6	31.333 / 6	96.500 / 6	174.833 / 6	371.500 / 6	727.000 / 6	1758.000 / 1
averaging weight	0.044	0.044	0.137	0.248	0.527	0	0

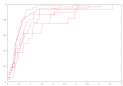
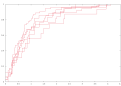
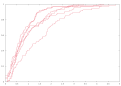
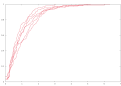
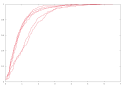
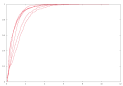
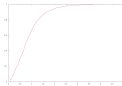
Radius Asymmetry: 0.419

similarity	0.600	0.933	0.467	0.267	0	n/a	n/a
Strahler* order	0	1	2	3	4	5	6
							
∅ # edges / # trees	31.833 / 6	31.333 / 6	96.500 / 6	174.833 / 6	371.500 / 6	939.000 / 1	0 / 0
averaging weight	0.095	0.094	0.288	0.523	0	0	0

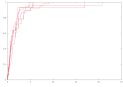
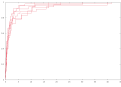
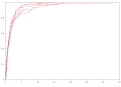
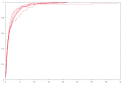
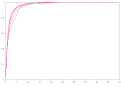
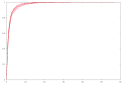
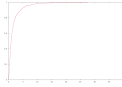
Bifurcation Exponent: 0.696

similarity	0.867	1.000	0.733	0.600	0.067	n/a	n/a
Strahler* order	0	1	2	3	4	5	6
							
∅ # edges / # trees	18.000 / 6	20.833 / 6	70.833 / 6	126.333 / 6	286.500 / 6	828.000 / 1	0 / 0
averaging weight	0.076	0.088	0.300	0.535	0	0	0

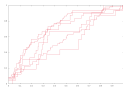
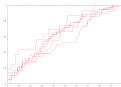
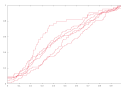
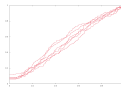
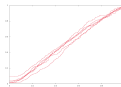
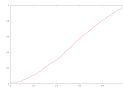

Edge Length: 0.534

similarity	0.867	1.000	0.533	0.533	0.467	0.067	n/a
Strahler* order	0	1	2	3	4	5	6
							
∅ # edges / # trees	31.833 / 6	31.333 / 6	96.500 / 6	174.833 / 6	371.500 / 6	727.000 / 6	1758.000 / 1
averaging weight	0.045	0.044	0.137	0.248	0.526	0	0

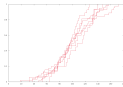
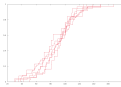
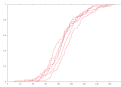
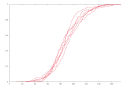
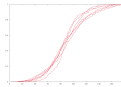
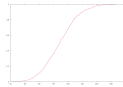

Length Decrease: 0.683

similarity	1.000	1.000	1.000	1.000	0.400	0.533	n/a
Strahler* order	0	1	2	3	4	5	6
							
∅ # edges / # trees	29.167 / 6	29.667 / 6	92.333 / 6	167.000 / 6	357.000 / 6	688.667 / 6	1649.000 / 1
averaging weight	0.043	0.044	0.137	0.247	0.529	0	0

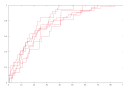
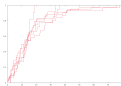
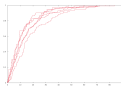
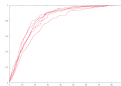
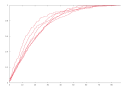
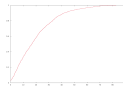

Length Asymmetry: 0.701

similarity	0.733	1.000	0.533	0.733	0.667	n/a	n/a
Strahler* order	0	1	2	3	4	5	6
							
∅ # edges / # trees	31.833 / 6	31.333 / 6	96.500 / 6	174.833 / 6	371.500 / 6	939.000 / 1	0 / 0
averaging weight	0.095	0.094	0.288	0.523	0	0	0

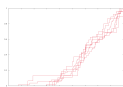
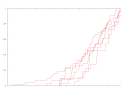
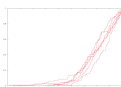
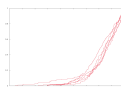
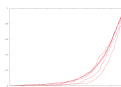
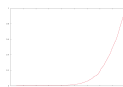

Angle φ_a : 0.779

similarity	1.000	1.000	0.600	0.800	0.400	n/a	n/a
Strahler* order	0	1	2	3	4	5	6
							
∅ # edges / # trees	29.667 / 6	28.333 / 6	90.500 / 6	160.500 / 6	357.167 / 6	923.000 / 1	0 / 0
averaging weight	0.096	0.092	0.293	0.519	0	0	0

Angle φ_b : 0.837

similarity	1.000	1.000	0.800	0.800	0.533	n/a	n/a
Strahler* order	0	1	2	3	4	5	6
							
∅ # edges / # trees	28.667 / 6	26.667 / 6	87.000 / 6	152.833 / 6	338.167 / 6	867.000 / 1	0 / 0
averaging weight	0.097	0.090	0.295	0.518	0	0	0

Angle φ_c : 0.817

similarity	1.000	0.933	0.867	0.733	0.467	n/a	n/a
Strahler* order	0	1	2	3	4	5	6
							
∅ # edges / # trees	28.667 / 6	26.667 / 6	87.000 / 6	152.833 / 6	337.500 / 6	867.000 / 1	0 / 0
averaging weight	0.097	0.090	0.295	0.518	0	0	0

Overview

For mouse and rat, PV and HV vascular trees, the table lists the similarity values among the experimentally acquired trees on a scale from 0 to 1.

feature	mouse		rat	
	PV	HV	PV	HV
radius	0.174	0.129	0.091	0.030
radius decrease	0.552	0.647	0.392	0.392
radius asymmetry	0.444	0.466	0.235	0.419
bifurcation exponent	0.745	0.613	0.381	0.696
length	0.466	0.730	0.489	0.534
length decrease	0.943	0.978	0.810	0.683
length asymmetry	0.903	0.871	0.720	0.701
angle φ_a	0.739	0.575	0.562	0.779
angle φ_b	0.949	0.841	0.489	0.837
angle φ_c	0.807	0.661	0.641	0.817
radius average	0.568	0.554	0.330	0.530
length average	0.831	0.872	0.700	0.648
angle average	0.841	0.710	0.571	0.812
total average	0.774	0.743	0.585	0.696

Variations Between Algorithmically Generated And Experimentally Acquired Vascular Trees

Lars Ole Schwen
Lei Wang

Weiwei Wei
Uta Dahmen

Felix Gremse
Tobias Preusser

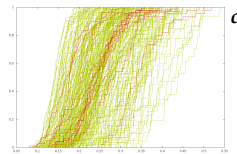
Josef Ehling

Legend

Edge Radii: 0.063^a

Strahler* order
similarity

... 2 ...
0.153^b



∅ # edges / # trees EA
∅ # edges / # trees AG
averaging weight

54.083^d / 12^e
81.771^f / 240^g
0.132^h

a similarity value for this geometric feature averaged over all Strahler* orders

b similarity value for this geometric feature and this Strahler* order

c plot of the cumulative distribution functions for all trees for this geometric feature and this Strahler* order (*green*: algorithmically generated, *red*: experimentally acquired vascular trees)

d average number of edges per experimentally acquired vascular tree considered for *c*

e number of experimentally acquired vascular trees considered for *c*

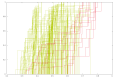
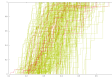
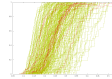
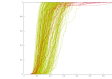
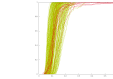
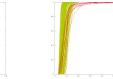
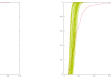
f average number of edges per algorithmically generated vascular tree considered for *c*

g number of algorithmically generated vascular trees considered for *c*

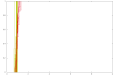
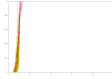
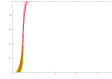
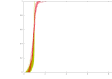
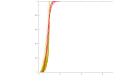
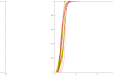
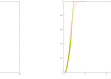
h averaging weight for *b* contributing to *a*

Algorithmically Generated vs. Experimentally Acquired Mouse PV

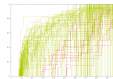
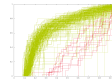
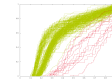
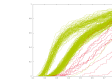
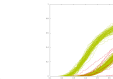
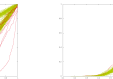
Edge Radii: 0.063

Strahler* order similarity	0	1	2	3	4	5	6
	0.585	0.274	0.153	0.057	0.009	0.003	0.000
							
∅ # edges / # trees EA	8.917 / 12	19.083 / 12	54.083 / 12	116.750 / 12	218.250 / 12	394.273 / 11	584.000 / 1
∅ # edges / # trees AG	6.825 / 240	30.804 / 240	81.771 / 240	168.042 / 240	322.600 / 240	614.427 / 239	759.100 / 80
averaging weight	0.015	0.048	0.132	0.278	0.527	0.000	0.000

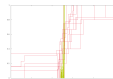
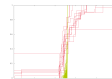
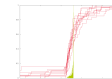
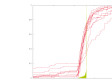
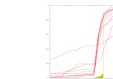

Radius Decrease: 0.028

Strahler* order similarity	0	1	2	3	4	5	6
	0.949	0.295	0.006	0.000	0.000	0.000	0.000
							
∅ # edges / # trees EA	7.917 / 12	19.083 / 12	54.083 / 12	116.750 / 12	218.250 / 12	394.273 / 11	584.000 / 1
∅ # edges / # trees AG	7.206 / 194	30.804 / 240	81.771 / 240	168.042 / 240	322.600 / 240	614.427 / 239	759.100 / 80
averaging weight	0.014	0.048	0.132	0.278	0.528	0.000	0.000

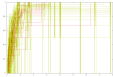
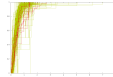
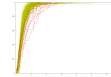
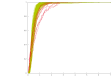
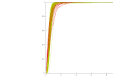
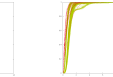
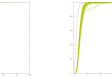
Radius Asymmetry: 0.062

Strahler* order similarity	0	1	2	3	4	5	6
	0.743	0.126	0.003	0.041	0.247	0.487	n/a
							
∅ # edges / # trees EA	8.917 / 12	19.083 / 12	54.083 / 12	116.750 / 12	208.000 / 11	283.000 / 1	0 / 0
∅ # edges / # trees AG	6.825 / 240	30.804 / 240	81.771 / 240	168.042 / 240	321.230 / 239	388.913 / 80	0 / 0
averaging weight	0.033	0.102	0.279	0.587	0.000	0.000	0.000

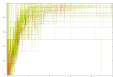
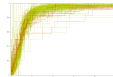
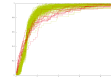
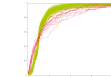
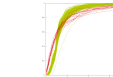
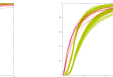
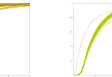
Bifurcation Exponent: 0.048

Strahler* order similarity	0	1	2	3	4	5	6
	0.811	0.218	0.000	0.000	0.000	0.000	n/a
							
∅ # edges / # trees EA	5.750 / 12	11.500 / 12	32.583 / 12	76.333 / 12	156.545 / 11	220.000 / 1	0 / 0
∅ # edges / # trees AG	6.825 / 240	30.804 / 240	81.771 / 240	168.042 / 240	321.230 / 239	388.913 / 80	0 / 0
averaging weight	0.033	0.099	0.272	0.596	0.000	0.000	0.000

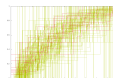
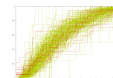
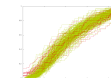
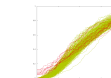
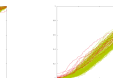
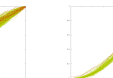
Edge Length: 0.130

Strahler* order similarity	0 0.957	1 0.787	2 0.384	3 0.086	4 0.005	5 0.000	6 0.000
							
∅ # edges / # trees EA	8.917 / 12	19.083 / 12	54.083 / 12	116.750 / 12	218.250 / 12	394.273 / 11	584.000 / 1
∅ # edges / # trees AG	6.825 / 240	30.804 / 240	81.771 / 240	168.042 / 240	322.600 / 240	614.427 / 239	759.100 / 80
averaging weight	0.015	0.048	0.132	0.278	0.527	0.000	0.000

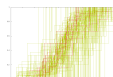
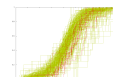
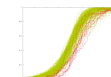
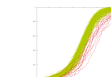
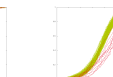
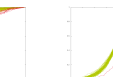
Length Decrease: 0.155

Strahler* order similarity	0 0.996	1 0.979	2 0.550	3 0.078	4 0.000	5 0.000	6 0.000
							
∅ # edges / # trees EA	7.000 / 12	18.583 / 12	51.750 / 12	112.083 / 12	209.917 / 12	372.727 / 11	548.000 / 1
∅ # edges / # trees AG	7.206 / 194	30.804 / 240	81.771 / 240	168.042 / 240	322.600 / 240	614.427 / 239	759.100 / 80
averaging weight	0.013	0.049	0.132	0.278	0.528	0.000	0.000

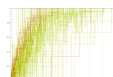
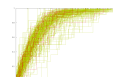
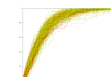
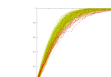
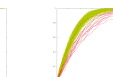
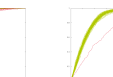
Length Asymmetry: 0.761

Strahler* order similarity	0 0.994	1 0.904	2 0.790	3 0.709	4 0.413	5 0.163	6 n/a
							
∅ # edges / # trees EA	8.917 / 12	19.083 / 12	54.083 / 12	116.750 / 12	208.000 / 11	283.000 / 1	0 / 0
∅ # edges / # trees AG	6.825 / 240	30.804 / 240	81.771 / 240	168.042 / 240	321.230 / 239	388.913 / 80	0 / 0
averaging weight	0.033	0.102	0.279	0.587	0.000	0.000	0.000

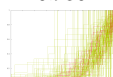




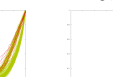
Angle φ_a : 0.255

Strahler* order similarity	0 0.964	1 0.806	2 0.267	3 0.116	4 0.091	5 0.000	6 n/a
							
∅ # edges / # trees EA	7.833 / 12	17.667 / 12	50.583 / 12	108.167 / 12	203.818 / 11	276.000 / 1	0 / 0
∅ # edges / # trees AG	6.825 / 240	30.804 / 240	81.771 / 240	168.042 / 240	321.230 / 239	388.913 / 80	0 / 0
averaging weight	0.032	0.102	0.280	0.587	0.000	0.000	0.000

Angle φ_b : 0.810

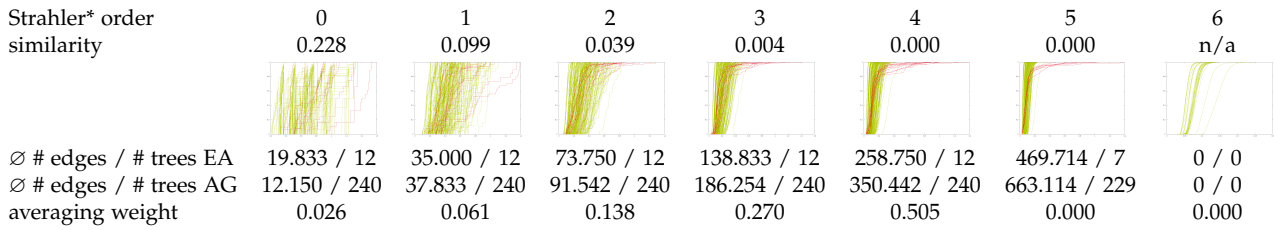
Strahler* order similarity	0 0.918	1 0.952	2 0.954	3 0.711	4 0.121	5 0.000	6 n/a
							
∅ # edges / # trees EA	7.667 / 12	16.833 / 12	48.583 / 12	104.083 / 12	192.636 / 11	261.000 / 1	0 / 0
∅ # edges / # trees AG	6.825 / 240	30.804 / 240	81.771 / 240	168.042 / 240	321.230 / 239	388.913 / 80	0 / 0
averaging weight	0.032	0.101	0.280	0.587	0.000	0.000	0.000

Angle φ_c : 0.793

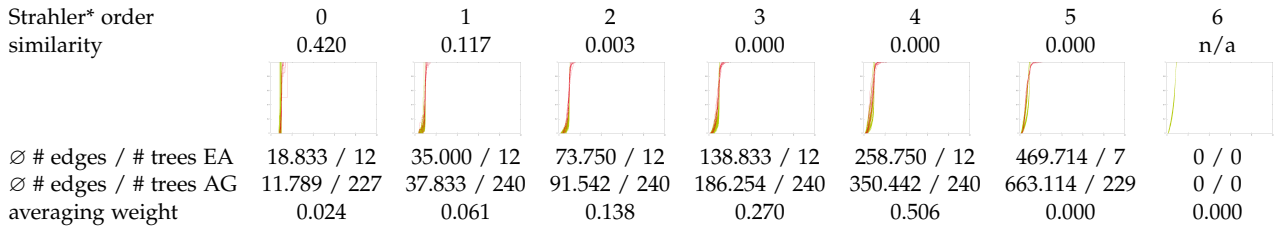
Strahler* order similarity	0 0.980	1 0.968	2 0.802	3 0.749	4 0.223	5 0.000	6 n/a
							
∅ # edges / # trees EA	7.667 / 12	16.833 / 12	48.583 / 12	104.083 / 12	192.364 / 11	261.000 / 1	0 / 0
∅ # edges / # trees AG	6.825 / 240	30.804 / 240	81.771 / 240	168.042 / 240	321.230 / 239	388.913 / 80	0 / 0
averaging weight	0.032	0.101	0.280	0.587	0.000	0.000	0.000

Algorithmically Generated vs. Experimentally Acquired Mouse HV

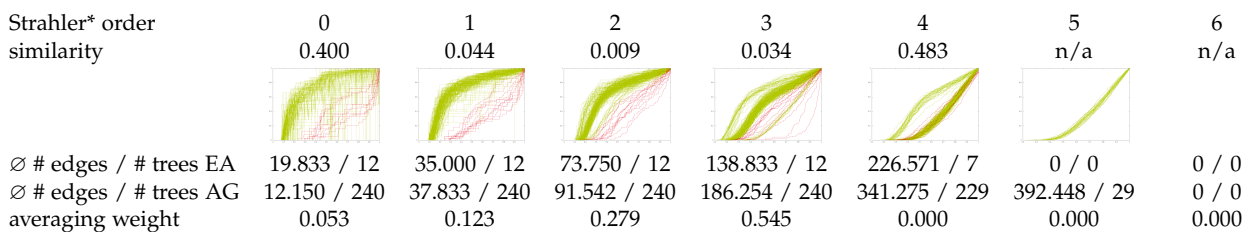
Edge Radii: 0.018



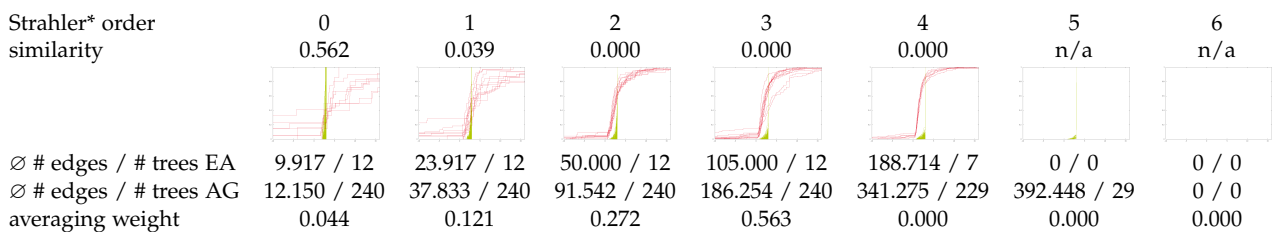
Radius Decrease: 0.018



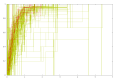
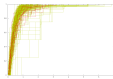
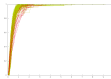
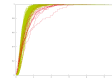
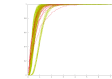
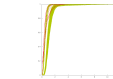
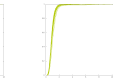
Radius Asymmetry: 0.047



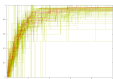
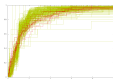
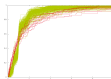
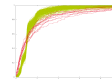
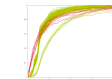
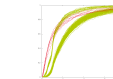
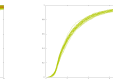
Bifurcation Exponent: 0.029



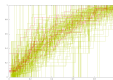
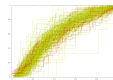
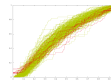
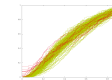
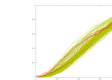
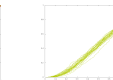

Edge Length: 0.139

Strahler* order similarity	0 0.826	1 0.785	2 0.318	3 0.091	4 0.003	5 0.000	6 n/a
							
∅ # edges / # trees EA	19.833 / 12	35.000 / 12	73.750 / 12	138.833 / 12	258.750 / 12	469.714 / 7	0 / 0
∅ # edges / # trees AG	12.150 / 240	37.833 / 240	91.542 / 240	186.254 / 240	350.442 / 240	663.114 / 229	0 / 0
averaging weight	0.026	0.061	0.138	0.270	0.505	0.000	0.000

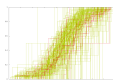
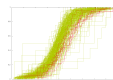
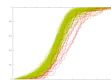
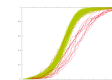
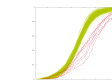
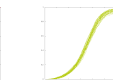

Length Decrease: 0.156

Strahler* order similarity	0 0.993	1 0.884	2 0.459	3 0.054	4 0.000	5 0.000	6 n/a
							
∅ # edges / # trees EA	18.455 / 11	34.000 / 12	71.583 / 12	134.917 / 12	246.833 / 12	440.714 / 7	0 / 0
∅ # edges / # trees AG	11.789 / 227	37.833 / 240	91.542 / 240	186.254 / 240	350.442 / 240	663.114 / 229	0 / 0
averaging weight	0.024	0.061	0.139	0.272	0.504	0.000	0.000

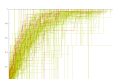
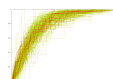
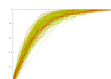
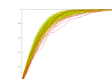
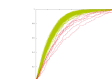
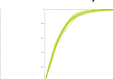

Length Asymmetry: 0.777

Strahler* order similarity	0 0.900	1 0.877	2 0.829	3 0.716	4 0.445	5 n/a	6 n/a
							
∅ # edges / # trees EA	19.833 / 12	35.000 / 12	73.750 / 12	138.833 / 12	226.571 / 7	0 / 0	0 / 0
∅ # edges / # trees AG	12.150 / 240	37.833 / 240	91.542 / 240	186.254 / 240	341.275 / 229	392.448 / 29	0 / 0
averaging weight	0.053	0.123	0.279	0.545	0.000	0.000	0.000

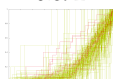
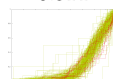
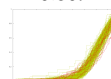
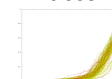
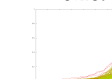
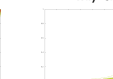

Angle φ_a : 0.228

Strahler* order similarity	0 0.874	1 0.580	2 0.243	3 0.081	4 0.000	5 n/a	6 n/a
							
∅ # edges / # trees EA	17.833 / 12	33.167 / 12	68.500 / 12	131.500 / 12	223.714 / 7	0 / 0	0 / 0
∅ # edges / # trees AG	12.150 / 240	37.833 / 240	91.542 / 240	186.254 / 240	341.275 / 229	392.448 / 29	0 / 0
averaging weight	0.051	0.124	0.277	0.548	0.000	0.000	0.000

Angle φ_b : 0.759

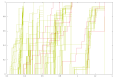
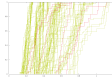
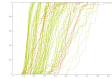
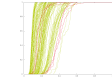
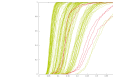
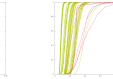
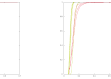
Strahler* order similarity	0 0.844	1 0.947	2 0.865	3 0.655	4 0.009	5 n/a	6 n/a
							
∅ # edges / # trees EA	16.833 / 12	32.000 / 12	66.833 / 12	126.083 / 12	208.857 / 7	0 / 0	0 / 0
∅ # edges / # trees AG	12.150 / 240	37.833 / 240	91.542 / 240	186.254 / 240	341.275 / 229	392.448 / 29	0 / 0
averaging weight	0.051	0.124	0.279	0.546	0.000	0.000	0.000

Angle φ_c : 0.674

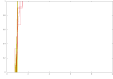
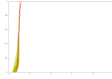
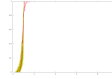
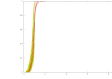
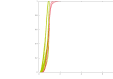
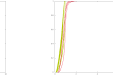
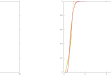
Strahler* order similarity	0 0.892	1 0.814	2 0.809	3 0.553	4 0.109	5 n/a	6 n/a
							
∅ # edges / # trees EA	16.833 / 12	32.000 / 12	66.750 / 12	126.083 / 12	208.857 / 7	0 / 0	0 / 0
∅ # edges / # trees AG	12.150 / 240	37.833 / 240	91.542 / 240	186.254 / 240	341.275 / 229	392.448 / 29	0 / 0
averaging weight	0.051	0.124	0.279	0.546	0.000	0.000	0.000

Algorithmically Generated vs. Experimentally Acquired Rat PV

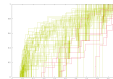
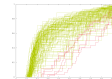
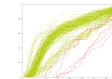
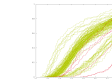
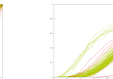
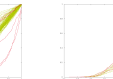
Edge Radii: 0.021

Strahler* order similarity	0 0.394	1 0.115	2 0.040	3 0.018	4 0.000	5 0.000	6 0.000
							
∅ # edges / # trees EA	9.000 / 6	24.667 / 6	69.167 / 6	162.167 / 6	342.667 / 6	677.500 / 6	1117.000 / 3
∅ # edges / # trees AG	7.875 / 120	28.708 / 120	79.100 / 120	159.383 / 120	295.950 / 120	610.089 / 101	826.714 / 7
averaging weight	0.014	0.045	0.126	0.273	0.541	0.000	0.000

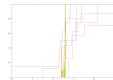
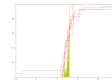
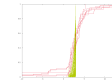
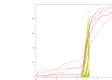
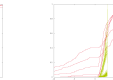
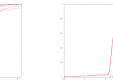
Radius Decrease: 0.034

Strahler* order similarity	0 0.909	1 0.464	2 0.010	3 0.000	4 0.000	5 0.000	6 0.000
							
∅ # edges / # trees EA	8.000 / 6	24.667 / 6	69.167 / 6	162.167 / 6	342.667 / 6	677.500 / 6	1117.000 / 3
∅ # edges / # trees AG	7.301 / 113	28.708 / 120	79.100 / 120	159.383 / 120	295.950 / 120	610.089 / 101	826.714 / 7
averaging weight	0.013	0.045	0.126	0.274	0.542	0.000	0.000

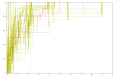
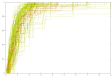
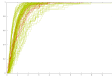
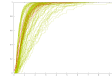
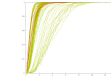
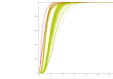
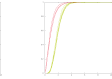
Radius Asymmetry: 0.128

Strahler* order similarity	0 0.682	1 0.211	2 0.065	3 0.114	4 0.026	5 0.714	6 n/a
							
∅ # edges / # trees EA	9.000 / 6	24.667 / 6	69.167 / 6	162.167 / 6	342.667 / 6	627.333 / 3	0 / 0
∅ # edges / # trees AG	7.875 / 120	28.708 / 120	79.100 / 120	159.383 / 120	316.465 / 101	419.000 / 7	0 / 0
averaging weight	0.031	0.099	0.274	0.596	0.000	0.000	0.000

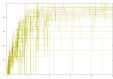
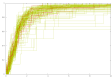
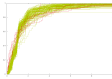
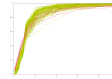
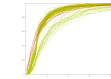
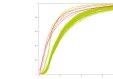
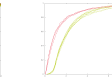
Bifurcation Exponent: 0.039

Strahler* order similarity	0 0.686	1 0.158	2 0.003	3 0.000	4 0.000	5 0.000	6 n/a
							
∅ # edges / # trees EA	5.667 / 6	16.333 / 6	44.333 / 6	96.667 / 6	237.000 / 6	523.667 / 3	0 / 0
∅ # edges / # trees AG	7.875 / 120	28.708 / 120	79.100 / 120	159.383 / 120	316.465 / 101	419.000 / 7	0 / 0
averaging weight	0.032	0.102	0.280	0.586	0.000	0.000	0.000

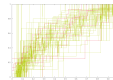
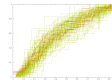
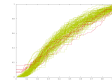
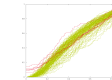
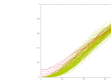
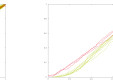
Edge Length: 0.130

Strahler* order similarity	0	1	2	3	4	5	6
	0.969	0.744	0.399	0.111	0.004	0.000	0.000
							
∅ # edges / # trees EA	9.000 / 6	24.667 / 6	69.167 / 6	162.167 / 6	342.667 / 6	677.500 / 6	1117.000 / 3
∅ # edges / # trees AG	7.875 / 120	28.708 / 120	79.100 / 120	159.383 / 120	295.950 / 120	610.089 / 101	826.714 / 7
averaging weight	0.014	0.045	0.126	0.273	0.541	0.000	0.000

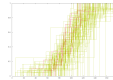
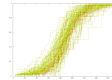
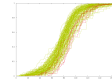
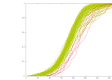
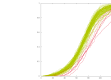
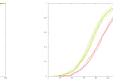
Length Decrease: 0.210

Strahler* order similarity	0	1	2	3	4	5	6
	0.987	0.975	0.533	0.278	0.021	0.000	0.000
							
∅ # edges / # trees EA	6.333 / 6	23.167 / 6	65.667 / 6	153.333 / 6	327.833 / 6	633.000 / 6	1058.000 / 3
∅ # edges / # trees AG	7.301 / 113	28.708 / 120	79.100 / 120	159.383 / 120	295.950 / 120	610.089 / 101	826.714 / 7
averaging weight	0.012	0.045	0.126	0.273	0.544	0.000	0.000

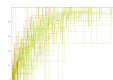
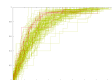
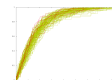
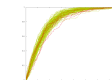
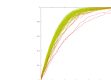
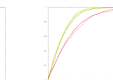
Length Asymmetry: 0.670

Strahler* order similarity	0	1	2	3	4	5	6
	0.967	0.988	0.871	0.510	0.371	0.000	n/a
							
∅ # edges / # trees EA	9.000 / 6	24.667 / 6	69.167 / 6	162.167 / 6	342.667 / 6	627.333 / 3	0 / 0
∅ # edges / # trees AG	7.875 / 120	28.708 / 120	79.100 / 120	159.383 / 120	316.465 / 101	419.000 / 7	0 / 0
averaging weight	0.031	0.099	0.274	0.596	0.000	0.000	0.000

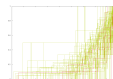
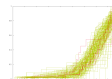
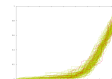
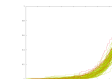
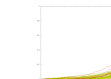
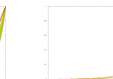
Angle φ_a : 0.266

Strahler* order similarity	0	1	2	3	4	5	6
	0.949	0.836	0.400	0.071	0.023	0.000	n/a
							
∅ # edges / # trees EA	7.833 / 6	23.167 / 6	62.833 / 6	144.333 / 6	323.667 / 6	616.000 / 3	0 / 0
∅ # edges / # trees AG	7.875 / 120	28.708 / 120	79.100 / 120	159.383 / 120	316.465 / 101	419.000 / 7	0 / 0
averaging weight	0.031	0.101	0.276	0.593	0.000	0.000	0.000

Angle φ_b : 0.806

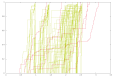
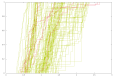
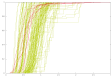
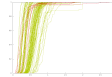
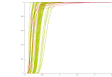
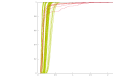
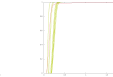
Strahler* order similarity	0	1	2	3	4	5	6
	0.942	0.854	0.896	0.750	0.219	0.000	n/a
							
∅ # edges / # trees EA	6.833 / 6	22.167 / 6	59.667 / 6	136.833 / 6	301.333 / 6	584.333 / 3	0 / 0
∅ # edges / # trees AG	7.875 / 120	28.708 / 120	79.100 / 120	159.383 / 120	316.465 / 101	419.000 / 7	0 / 0
averaging weight	0.029	0.101	0.276	0.593	0.000	0.000	0.000

Angle φ_c : 0.762




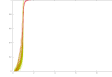
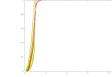
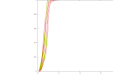
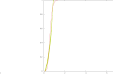
Strahler* order similarity	0	1	2	3	4	5	6
	0.931	0.900	0.890	0.671	0.111	0.000	n/a
							
∅ # edges / # trees EA	6.833 / 6	22.167 / 6	59.667 / 6	136.833 / 6	301.000 / 6	583.333 / 3	0 / 0
∅ # edges / # trees AG	7.875 / 120	28.708 / 120	79.100 / 120	159.383 / 120	316.465 / 101	419.000 / 7	0 / 0
averaging weight	0.029	0.101	0.276	0.593	0.000	0.000	0.000

Algorithmically Generated vs. Experimentally Acquired Rat HV

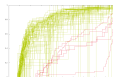
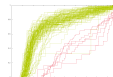
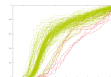
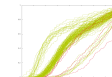
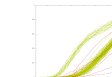
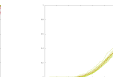

Edge Radii: 0.016

Strahler* order similarity	0	1	2	3	4	5	6
	0.231	0.101	0.019	0.003	0.000	0.000	0.000
							
∅ # edges / # trees EA	31.833 / 6	31.333 / 6	96.500 / 6	174.833 / 6	371.500 / 6	727.000 / 6	1758.000 / 1
∅ # edges / # trees AG	14.358 / 120	39.400 / 120	84.317 / 120	175.767 / 120	337.900 / 120	642.363 / 113	810.000 / 16
averaging weight	0.032	0.052	0.133	0.259	0.524	0.000	0.000

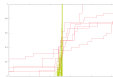
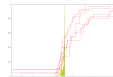
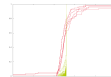
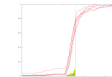
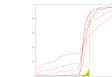
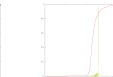

Radius Decrease: 0.024

Strahler* order similarity	0	1	2	3	4	5	6
	0.534	0.143	0.007	0.000	0.000	0.000	0.000
							
∅ # edges / # trees EA	30.833 / 6	31.333 / 6	96.500 / 6	174.833 / 6	371.500 / 6	727.000 / 6	1758.000 / 1
∅ # edges / # trees AG	14.843 / 108	39.400 / 120	84.317 / 120	175.767 / 120	337.900 / 120	642.363 / 113	810.000 / 16
averaging weight	0.030	0.052	0.134	0.260	0.525	0.000	0.000

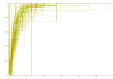
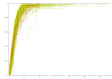
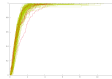
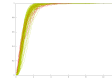
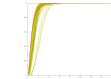
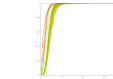
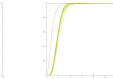
Radius Asymmetry: 0.159

Strahler* order similarity	0	1	2	3	4	5	6
	0.324	0.011	0.035	0.233	0.174	0.938	n/a
							
∅ # edges / # trees EA	31.833 / 6	31.333 / 6	96.500 / 6	174.833 / 6	371.500 / 6	939.000 / 1	0 / 0
∅ # edges / # trees AG	14.358 / 120	39.400 / 120	84.317 / 120	175.767 / 120	331.743 / 113	416.875 / 16	0 / 0
averaging weight	0.066	0.109	0.280	0.544	0.000	0.000	0.000

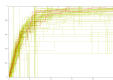
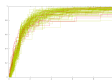
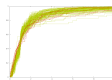
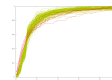
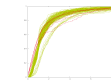
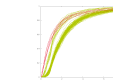
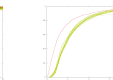
Bifurcation Exponent: 0.027

Strahler* order similarity	0	1	2	3	4	5	6
	0.433	0.017	0.000	0.000	0.000	0.000	n/a
							
∅ # edges / # trees EA	18.000 / 6	20.833 / 6	70.833 / 6	126.333 / 6	286.500 / 6	828.000 / 1	0 / 0
∅ # edges / # trees AG	14.358 / 120	39.400 / 120	84.317 / 120	175.767 / 120	331.743 / 113	416.875 / 16	0 / 0
averaging weight	0.059	0.106	0.285	0.550	0.000	0.000	0.000

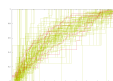
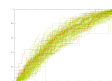
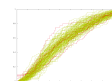
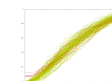
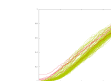
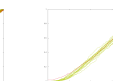
Edge Length: 0.210

Strahler* order similarity	0 0.857	1 0.922	2 0.585	3 0.201	4 0.008	5 0.000	6 0.000
							
∅ # edges / # trees EA	31.833 / 6	31.333 / 6	96.500 / 6	174.833 / 6	371.500 / 6	727.000 / 6	1758.000 / 1
∅ # edges / # trees AG	14.358 / 120	39.400 / 120	84.317 / 120	175.767 / 120	337.900 / 120	642.363 / 113	810.000 / 16
averaging weight	0.032	0.052	0.133	0.259	0.524	0.000	0.000

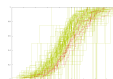
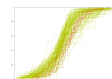
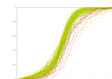
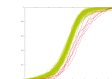
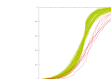
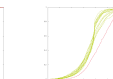
Length Decrease: 0.291

Strahler* order similarity	0 0.975	1 0.929	2 0.861	3 0.315	4 0.033	5 0.000	6 0.000
							
∅ # edges / # trees EA	29.167 / 6	29.667 / 6	92.333 / 6	167.000 / 6	357.000 / 6	688.667 / 6	1649.000 / 1
∅ # edges / # trees AG	14.843 / 108	39.400 / 120	84.317 / 120	175.767 / 120	337.900 / 120	642.363 / 113	810.000 / 16
averaging weight	0.030	0.052	0.134	0.259	0.526	0.000	0.000

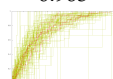
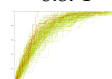
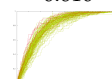
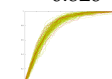
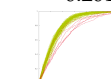
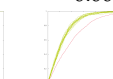
Length Asymmetry: 0.778

Strahler* order similarity	0 0.910	1 0.939	2 0.721	3 0.760	4 0.261	5 0.875	6 n/a
							
∅ # edges / # trees EA	31.833 / 6	31.333 / 6	96.500 / 6	174.833 / 6	371.500 / 6	939.000 / 1	0 / 0
∅ # edges / # trees AG	14.358 / 120	39.400 / 120	84.317 / 120	175.767 / 120	331.743 / 113	416.875 / 16	0 / 0
averaging weight	0.066	0.109	0.280	0.544	0.000	0.000	0.000

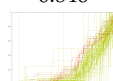

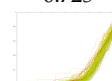
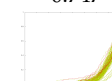


Angle φ_a : 0.234

Strahler* order similarity	0 0.849	1 0.699	2 0.340	3 0.011	4 0.000	5 0.000	6 n/a
							
∅ # edges / # trees EA	29.667 / 6	28.333 / 6	90.500 / 6	160.500 / 6	357.167 / 6	923.000 / 1	0 / 0
∅ # edges / # trees AG	14.358 / 120	39.400 / 120	84.317 / 120	175.767 / 120	331.743 / 113	416.875 / 16	0 / 0
averaging weight	0.067	0.108	0.282	0.543	0.000	0.000	0.000

Angle φ_b : 0.779

Strahler* order similarity	0 0.963	1 0.874	2 0.610	3 0.826	4 0.201	5 0.000	6 n/a
							
∅ # edges / # trees EA	28.667 / 6	26.667 / 6	87.000 / 6	152.833 / 6	338.167 / 6	867.000 / 1	0 / 0
∅ # edges / # trees AG	14.358 / 120	39.400 / 120	84.317 / 120	175.767 / 120	331.743 / 113	416.875 / 16	0 / 0
averaging weight	0.067	0.107	0.283	0.542	0.000	0.000	0.000

Angle φ_c : 0.769

Strahler* order similarity	0 0.846	1 0.943	2 0.725	3 0.747	4 0.168	5 0.000	6 n/a
							
∅ # edges / # trees EA	28.667 / 6	26.667 / 6	87.000 / 6	152.833 / 6	337.500 / 6	867.000 / 1	0 / 0
∅ # edges / # trees AG	14.358 / 120	39.400 / 120	84.317 / 120	175.767 / 120	331.743 / 113	416.875 / 16	0 / 0
averaging weight	0.067	0.107	0.283	0.542	0.000	0.000	0.000

Overview

For mouse and rat, PV and HV vascular trees, the following table lists the similarity values between experimentally acquired and calibrated algorithmically generated vascular trees on a scale from 0 to 1.

feature	mouse		rat	
	PV	HV	PV	HV
radius	0.063	0.018	0.021	0.016
radius decrease	0.028	0.018	0.034	0.024
radius asymmetry	0.062	0.047	0.128	0.159
bifurcation exponent	0.048	0.029	0.039	0.027
length	0.130	0.139	0.130	0.210
length decrease	0.155	0.156	0.210	0.291
length asymmetry	0.761	0.777	0.670	0.778
angle φ_a	0.255	0.228	0.266	0.234
angle φ_b	0.810	0.759	0.806	0.779
angle φ_c	0.793	0.674	0.762	0.769
radius average	0.047	0.029	0.054	0.062
length average	0.386	0.361	0.355	0.447
angle average	0.640	0.585	0.610	0.601
total average	0.410	0.362	0.395	0.434